Australia's National Science Agency

MD-WERP Report T2.H.3

Impact of hydrologic non-stationarity and changing climate on runoff in the northern Murray–Darling Basin

Jorge L. Peña-Arancibia, Guobin Fu, Hongxing Zheng, Yingying Yu and Francis H. S. Chiew

MD-WERP Project T2.H

January 2025

Citation

Peña-Arancibia JL, Fu G, Zheng X, Yu Y, and Chiew FHS (2025) Impact of hydrologic non-stationarity and changing climate on runoff in the northern Murray−Darling Basin. CSIRO Technical report for the Murray-Darling Basin Authority. CSIRO, Australia.

Copyright

© Murray–Darling Basin Authority 2024. With the exception of the Commonwealth Coat of Arms, the MDBA logo, the MD–WERP logo, the CSIRO logo, and any trademarks, and any exempt content (if identified), this publication is provided under a Creative Commons Attribution 4.0 licence (CC-BY). CSIRO have all necessary rights and permissions to make this publication available publicly under a CC-BY licence for the purposes of supporting MD-WERP objectives or other research purposes.

Important disclaimer

CSIRO advises that the information contained in this publication comprises general statements based on scientific research. The reader is advised and needs to be aware that such information may be incomplete or unable to be used in any specific situation. No reliance or actions must therefore be made on that information without seeking prior expert professional, scientific and technical advice. To the extent permitted by law, CSIRO (including its employees and consultants) excludes all liability to any person for any consequences, including but not limited to all losses, damages, costs, expenses and any other compensation, arising directly or indirectly from using this publication (in part or in whole) and any information or material contained in it.

CSIRO is committed to providing web accessible content wherever possible. If you are having difficulties with accessing this document please contact csiro.au/contact.

Acknowledgement

Supported through funding from the Australian Government Murray–Darling Water and Environment Research Program.

Contents

Figures

Tables

Acknowledgements

This work is carried out in CSIRO Land and Water as part of the Murray–Darling Water and Environment Research Program (MD-WERP). The Murray–Darling Water and Environment Research Program is an Australian Government initiative to strengthen scientific knowledge of the Murray–Darling Basin. It is designed to help inform water and environment management decisions which will improve outcomes for the Basin and its communities. Four priority themes have been identified as the focus of the strategic research: Climate Adaptation, Hydrology, Environmental Outcomes, and Social, Economic and Cultural Outcomes. This research falls in the Hydrology theme.

The authors thank David Post from CSIRO; Charlotte Dennis, Alistair Korn, Jong Lee, Sohail Rai, Aftab Ahmad and Georgia Kerber from the Murray–Darling Basin Authority for project management and for reviewing the report.

The authors pay respect to the Traditional Owners and their Nations of the Murray−Darling Basin. We acknowledge their deep cultural, social, environmental, spiritual, and economic connection to their lands and waters.

Executive summary

This study investigates hydrological non-stationarity in the Murray-Darling Basin (MDB) and its drivers and impacts, with a focus on the northern MDB (NMDB). The research explores changes in rainfall characteristics, rainfall-runoff relationships, vegetation dynamics, and water use patterns, aiming to address data and knowledge gaps identified in previous studies. Key research questions include understanding how changes in weather systems influence rainfall and water availability, the role of vegetation dynamics and land use in modifying hydrological processes, and the impacts of farm dams on runoff.

The findings reveal that rainfall characteristics and their relationship with weather systems vary significantly across the MDB. Thunderstorms dominate rainfall generation in the NMDB, while a mix of weather types contributes to rainfall in the southern MDB (SMDB). Rainfall anomalies align with wet and dry periods, including the Millennium Drought, highlighting the spatial and temporal variability in hydrological responses. Analysis of 110 largely unregulated catchments shows significant differences in the impacts of hydrological non-stationarity between the NMDB and SMDB. In the NMDB, most catchments experienced minimal changes in rainfall-runoff relationships during the drought and have recovered post-drought. Conversely, in the SMDB, a majority of catchments investigated exhibit significant runoff declines and persistent changes in rainfall-runoff relationships, particularly in drier western regions, with many failing to recover fully post-drought.

Vegetation dynamics were assessed using a long-term Leaf Area Index (LAI) dataset, revealing significant greening trends in forested areas of the SMDB during both cool and warm months. Actual evapotranspiration (ET_a) followed rainfall declines in the NMDB but remained stable in the SMDB despite reductions in rainfall, contributing to the observed runoff declines. The study also highlights the role of farm dams, which reduce runoff in headwater catchments, particularly during dry years.

Shifts in rainfall-runoff relationship (i.e., hydrological non-stationarity) significantly affect the robustness and reliability in hydrological modelling. Adapted hydrological model by considering the dynamics of farm dam and vegetation dynamics contribute to improve model performance, particularly for catchments in the SMDB. Modelling results suggest that reduction in rainfall and growth in farm dams' volumes during the drought period are the most important drivers leading to lower runoff in the Millennium Drought.

This research also examined long-term (~20 years) irrigation dynamics to understand their impact on water availability. Advanced remote sensing techniques were employed to map irrigated areas and quantify their water use. These maps provided high spatial (30 m) and temporal (monthly) resolution, enabling detailed analysis of irrigation extent and water use. Accuracy assessments showed strong agreement with ground-based observations, with overall accuracies exceeding 85%, confirming the reliability of the remote sensing approach for large-scale irrigation mapping.

Overall, the research provides critical insights into regional hydroclimate and landscape processes in the MDB and how these impact hydrological non-stationarity, particularly in the SMDB.

1 Introduction

1.1 Background

The Murray–Darling Basin (MDB, 1.061 million km^2, Figure 1), located in southeastern Australia, is the largest river system in Australia and home to 2.4 million people. With a mean annual rainfall of 465 mm/year (estimated for 1990–2020 from Jones et al., 2009), large parts of the MDB experience a semi-arid climate (Beck et al., 2018). Rainfall and streamflow in the MDB experience high spatiotemporal variability (Chiew et al., 2022b). The natural drainage divides the river system into the northern MDB (NMDB) and southern MDB (SMDB). The NMDB is defined as the catchment area drained by all the rivers flowing into and including the Barwon-Darling (or Baaka) River, which receives inflows from the Paroo, Warrego, Nebine, Condamine-Balonne, Moonie, Border Rivers, Gwydir, Namoi and Macquarie-Castlereagh river valleys (maroon regions in Figure 1). The SMDB includes all rivers that drain into and including the Murray River, which receives inflows from the Lachlan, Murrumbidgee, Ovens, Goulburn-Broken, Campaspe, Loddon-Avoca, Wimmera, Lower Darling and the Eastern Mount Lofty Ranges river valleys (orange regions in Figure 1).

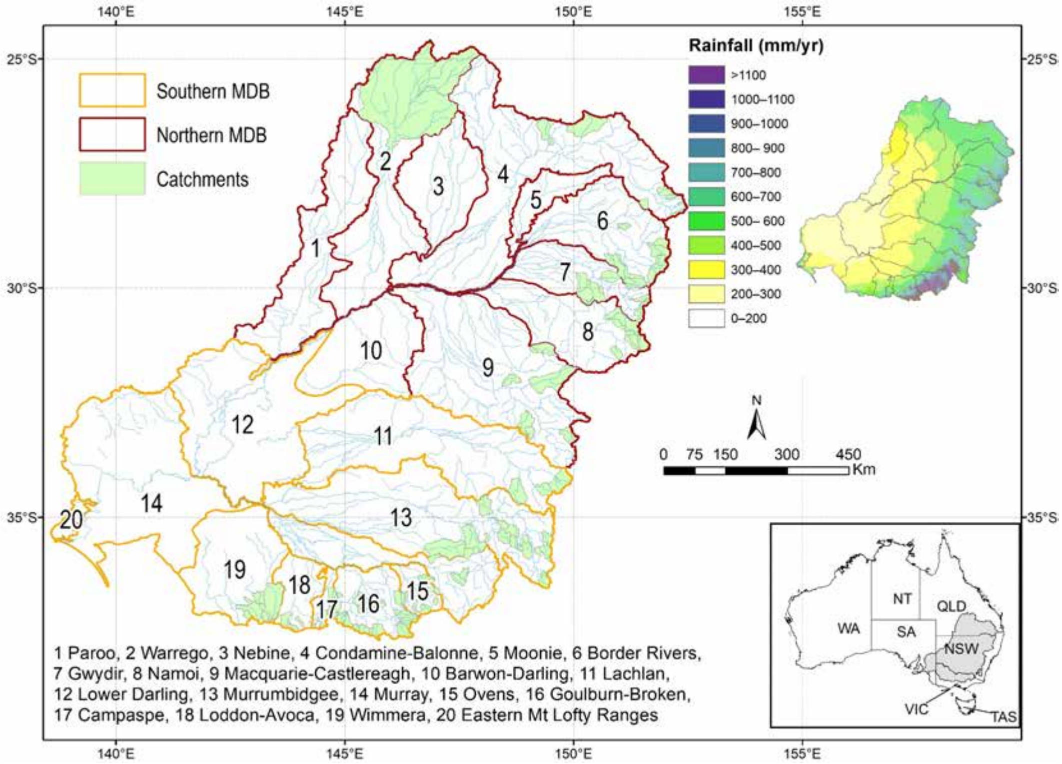

Figure 1. River valley divisions of the Murray-Darling Basin (NMDB valleys in maroon outline, SMDB valleys in orange outline) including catchments used for more detailed analyses (light green). Upper-right inset shows mean annual rainfall for 1990–2020.

Rainfall and streamflow patterns differ in the MDB, with the NMDB experiencing highly variable tropical and extratropical summer (December to February) rainfall and relatively uniform runoff through the year. Conversely, rainfall in the SMDB is winter dominated and most of the runoff occurs in winter and spring (Chiew et al., 2022b; Gallant et al., 2012).

In recent decades, the MDB experienced periods of severe droughts – like the 1997–2009 'Millennium Drought' (van Dijk et al., 2013; Yang et al., 2017) – and years with large flooding following the 2010 La Niña (Callaghan, 2019). In the NMDB, the extremely dry period from January 2017 to December 2019, the 'Tinderbox Drought' (Devanand et al., 2024), resulted in very low inflows into major reservoirs, and by January 2020 a record low 254 GL out of 4,708 GL (5.4%) was stored in NMDB reservoirs (BoM, 2020). Peña-Arancibia et al. (2023a) reported annual long-term (1970/71 to 2021/22) basin-wide climate and biophysical processes' trends, highlighting rainfall and runoff declines across the MDB (particularly in runoff-generating areas), concurrent actual evapotranspiration (ET_a) declines, but 'greening' trends (increased Leaf Area Index, LAI) in the SMDB. In areas of the southern MDB within the state of Victoria (lower right inset in Figure 1), Fu et al. (2024) attributed changes in rainfall that are important for runoff generation to changes in weather systems, particularly a shift from winter front rainfall to summer thunderstorms.

To mitigate low water availability during dry spells, farm dams (which intercept landscape runoff and provide water when surface water is scarce) construction increased across the MDB in runoff-generating areas, especially in the 1990s and during the Millennium Drought (Peña-Arancibia et al., 2023b). Currently, farm dams in the MDB have an estimated storage capacity of 2,629 GL (~8% of the combined storage capacity), with 49% in the NMDB and 51% in the SMDB (Peña-Arancibia et al., 2023b). Evaluating 112 headwater catchments across different climate and land covers in the MDB, Robertson et al. (2023) estimated that farm dams contribute to a mean annual runoff reduction of 13% in these catchments. Chiew et al. (2022a) ascribed a roughly equal importance to climate and historical water resource development (water infrastructure and water extraction for irrigation and other productive activities) as the causes of long-term reduction of streamflow experienced in the Barwon-Darling River in the last 30 years.

These evaluations highlighted the potential role of 'hydrologic non-stationarity' reported in MDB catchments (Chiew et al., 2014; Fowler et al., 2022), induced by changes in climate and catchment development, which can modify hydroclimate characteristics and dominant hydrological processes. Under dry climates, hydrologic non-stationarity results in reduced annual runoff generated from a similar amount of annual rainfall (Chiew et al., 2014). Causes of hydrologic non-stationarity have been evaluated in the MDB, with most studies focusing on catchments in the SMDB or similar climatic and biophysical settings (e.g. in Victoria, Fowler et al., 2022, and references therein), although changes in the rainfall-runoff relationship and declines in runoff have also been observed in catchments in the NMDB, particularly during the Millennium Drought (Amirthanathan et al., 2023; Rassam et al., 2017).

1.2 Aim and objectives

The MDBA initiated this project in MD-WERP (Murray–Darling Water and Environment Research Program) Hydrology Theme with the aim to examine drivers leading to hydrologic non-stationarity in the MDB and its impacts, with particular focus on the NMDB. Recent studies (Deb et al., 2019; Fowler et al., 2022; Peterson et al., 2021; Saft et al., 2016) have assessed drivers leading to hydrologic non-stationarity, and identified data and knowledge gaps that can be used to elucidate causality. Following these previous findings and aiming to bridge some of these gaps, this report focused on key potential drivers of non-stationarity:

1. Changes in rainfall characteristics can result in nonstationary rainfall-runoff relationship and these can be related to changes in weather systems. The contributions of changing synoptic weather types to rainfall are essential for understanding regional water availability and water resource management. Chapter 2 explores the spatial and temporal variability of rainfall responses to changes in weather types.
2. Chapter 3 describes analysis of rainfall and streamflow data from 110 largely unregulated MDB catchments with minimal land use change. Various types of statistical analysis are used to assess non-stationarity in the rainfall-runoff relationship.
3. Chapter 4 describes an assessment of changes in vegetation dynamics to elucidate their potential role in modifying the rainfall-runoff relationship, including changes in LAI and actual evapotranspiration (ET_a). The research focused on sourcing and developing diagnostic datasets that incorporate remotely sensed landscape vegetation processes.
4. Chapter 5 applies rainfall-runoff models that include process representation of vegetation dynamics (described in Chapter 4) and farm dams. Farm dams' storage growth and monthly LAI from multitemporal satellite observations are used as model inputs, in addition to conventional climate inputs. Sensitivity analysis and scenario modelling are performed to quantify the contributions of climate, vegetation, and land use change on key hydrological variables.
5. The potential role of irrigation is assessed by mapping main irrigated areas across the MDB using Artificial Intelligence/Machine Learning (AI/ML) techniques and water use trends from 2000 to 2020 (Chapter 6).

2 Weather systems and annual rainfall variability

Spatiotemporal rainfall variability in the MDB is high compared to other basins worldwide due to the influence of many climate drivers (Gallant et al., 2012; Nicholls et al., 1997). El Niño-Southern Oscillation (ENSO), the Indian Ocean Dipole (IOD), the Southern Annular Mode (SAM) and the Subtropical Ridge (STR) can have significant impacts on the MDB's climate. Moreover, these climate drivers interact in complex ways, contributing to the variability of the MDB's hydroclimate. In the MDB the first half of the 20th century experienced mostly drier than average conditions, followed by generally wet years in the 1950s and the 1970s (Figure 2). Annual rainfall in the last two decades in the MDB has been dominated by dry years, except for La Niña years in 2010/11 and 2011/12 and from 2020/21 to 2022/23 (Figure 2).

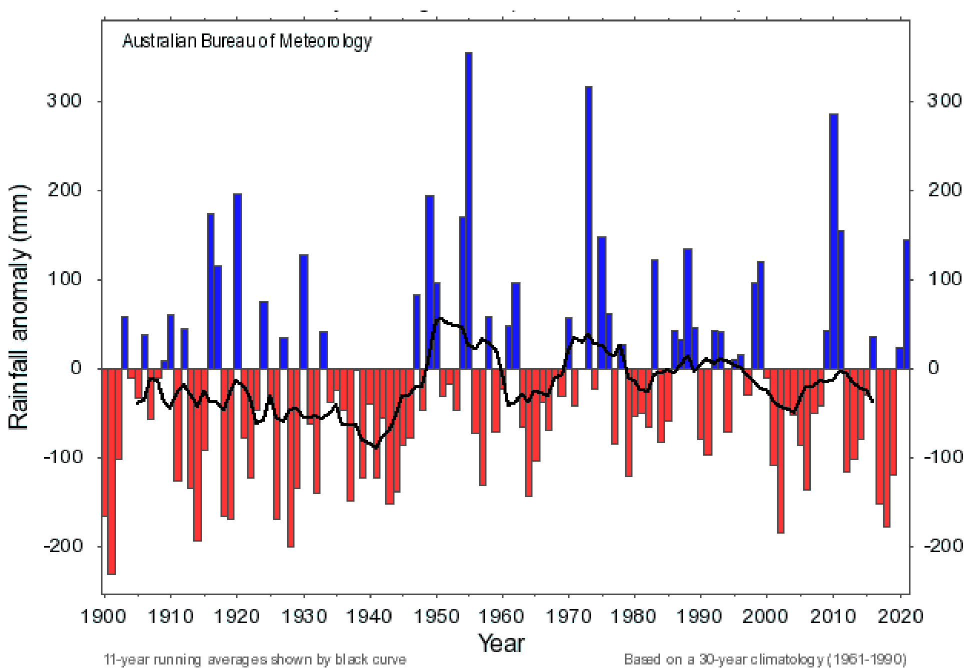

Figure 2. Murray−Darling Basin (MDBA) hydrological year (July to next June) rainfall anomaly for 1900/01−2021/22 (with 11-year running mean in black, which divides the 121 years into 11 periods of 11 years). Anomaly based on 30-year climatology (1961–90). Source: Bureau of Meteorology website http://www.bom.gov.au/climate/.

It is well known that the changes in rainfall characteristics can result in nonstationary rainfall-runoff relationship (Ajami et al., 2017; Chiew et al., 2014; Chiew et al., 2022a; Deb et al., 2019; Fowler et al., 2022; Fu et al., 2021a; Hughes and Vaze, 2015; Rassam et al., 2017; Vaze et al., 2010), i.e., the same annual rainfall could produce different streamflow due to different rainfall characteristics or changed catchment conditions. Furthermore, the rainfall characteristics are related to weather systems.

The weather systems' contributions to rainfall and their spatiotemporal variability in the MDB were investigated with a multi-method weather type dataset (Pepler et al., 2020) and SILO gridded daily rainfall (Jeffrey et al., 2001) for the period of 1979–2015. The weather type database incorporates two multi-method datasets of cold fronts and low-pressure systems to enhance the robustness of the cyclone and front datasets and has advantages over the weaker and less impactful events derived from a single method. The datasets of front and low-pressure systems are then combined with a thunderstorm dataset to produce the full weather system dataset. Table 1 describes the weather types which includes cyclone, front and thunderstorm, as well as their combinations.

Table 1. Description of weather types used in this study.

Name	Long name	Description
CO	Cyclone-Only	A cyclone/low is present in both datasets
FO	Front-Only	A cold front is present in both datasets
TO	Thunderstorm-Only	A thunderstorm environment is present
CF	Cyclone-Front	Both a cyclone and a cold front are present
CT	Cyclone-Thunderstorm	Both a cyclone and a thunderstorm environment are present
FT	Front-Thunderstorm	Both a cold front and a thunderstorm environment are present
CFT	Triple storm	A cyclone, cold front, and thunderstorm are all present
Other	Other	Days with Highs (H), Warm Fronts (WF), Fronts or Lows identified by only one method (Unconf) and when no weather system is defined (Undef)

A comparison of weather systems and total rainfall for 1979–2015 shows that three weather systems, Front-Only (FO), Cyclone-Only (CO) and Thunderstorm-Only (TO) and their combinations (7 weather types, Table 1) account for 89.3% of total rainfall and 49.3% number of days for the entire MDB (Figure 3).

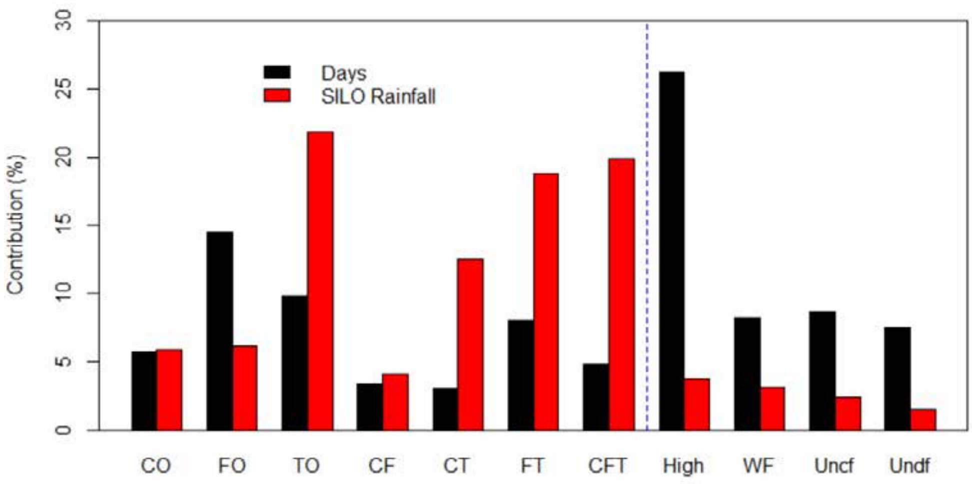

Figure 3. Contributions of seven weather systems to total rainfall for 1979–2015 in the MDB and their combinations. CO= Cyclone-Only, FO= Front-Only, TO= Thunderstorm-Only, CF= Cyclone-Front, CT= Cyclone-Thunderstorm, FT= Front-Thunderstorm, CFT= Triple storm.

The contributions of the 7 weather types to MDB rainfall show spatially heterogeneous patterns (Figure 4). The total number of days of FO, CO and TO and their combinations increase from the northwest (40%) to the southeast (55%), while their total contributions to annual rainfall show a north-south pattern (Figure 4). That is, the 7 weather types explain a large proportion (almost all) of the rainfall and slightly more in the SMDB.

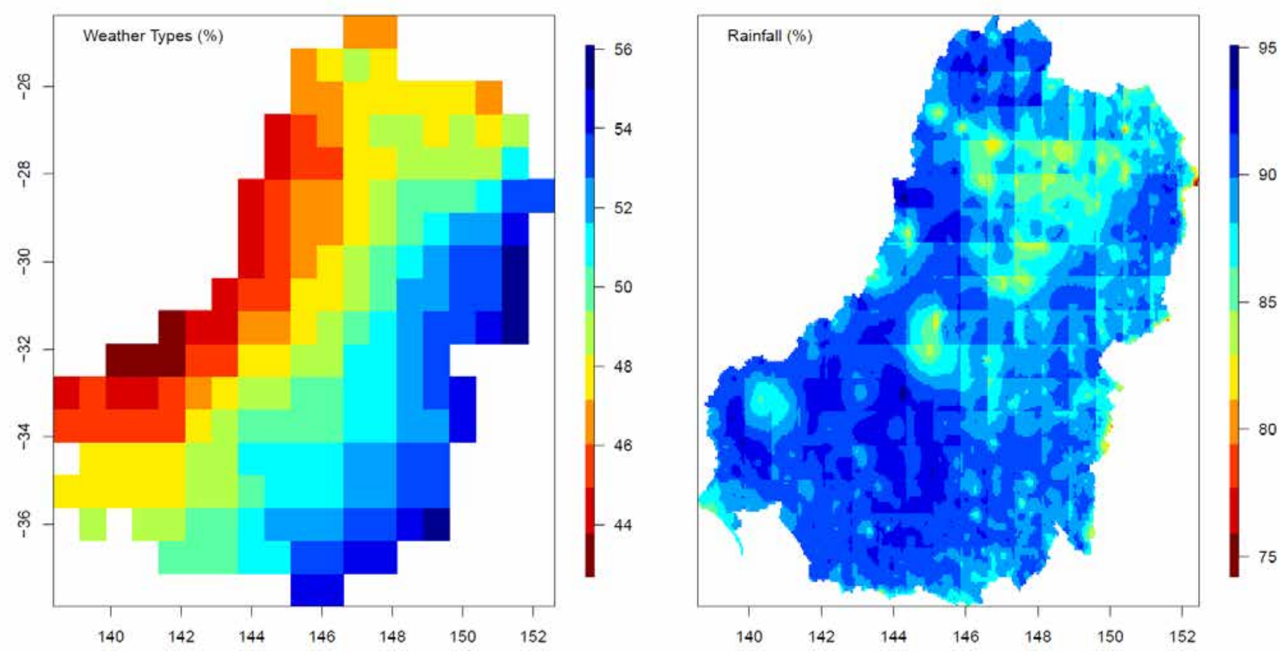

Figure 4. Spatial distributions of days from 7 weather types (%, left) and their contribution to total annual rainfall (%, right).

The combined contribution of CO, FO and CFT to total rainfall has a clear south-north pattern: up to 30% in the SMDB and around 10% in the NMDB (Figure 5), while TO has the opposite north-south pattern with thunderstorm contributing more than 40% of the total rainfall in the NMDB. This conclusion is reinforced in Figure 6, which shows that rainfall in the SMDB comes from different weather types (small coefficient of variation, with the seven weather types contributing to rainfall) while TO is by far the main component of rainfall in the NMDB.

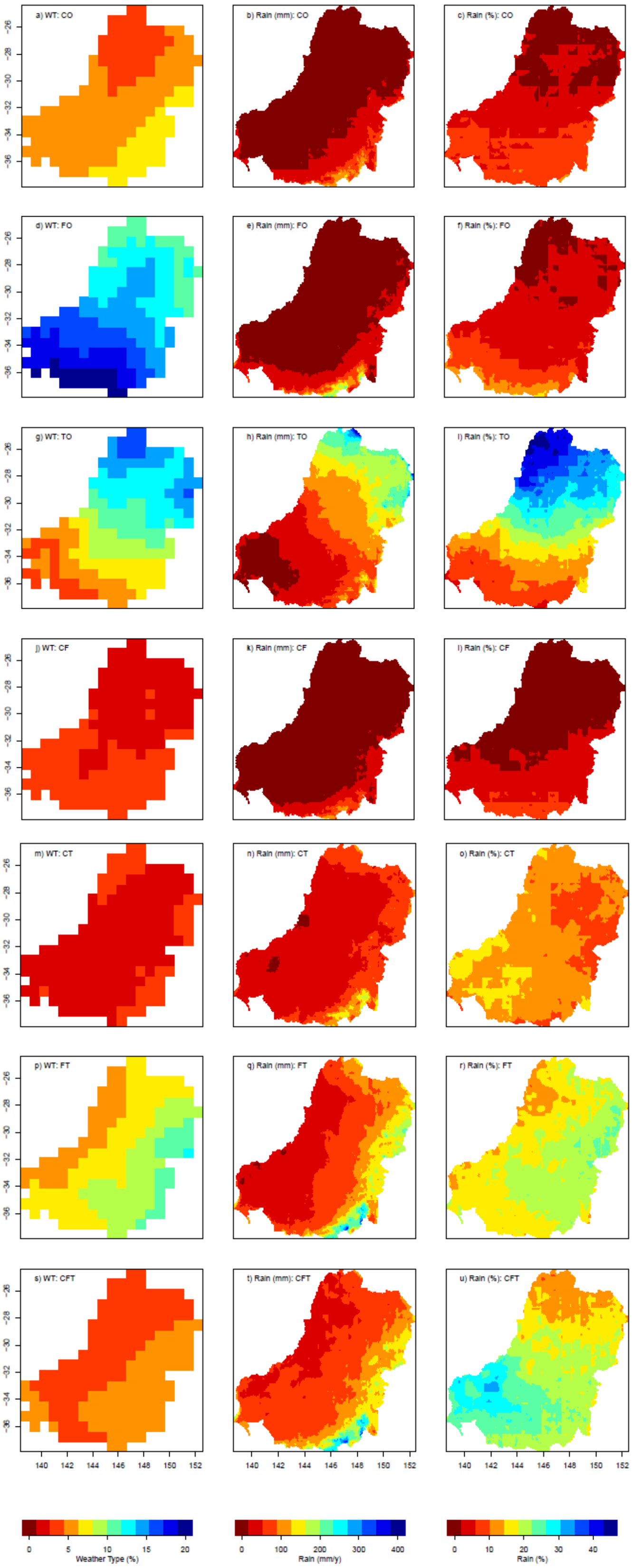

Figure 5. Spatial distributions of percentages (%) of days (left column), annual rainfall (mm/year) (middle column) and percentage (%) of annual rainfall (right column) for each weather types (each row) in 1979–2015. CO= Cyclone-Only, FO= Front-Only, TO= Thunderstorm-Only, CF= Cyclone-Front, CT= Cyclone-Thunderstorm, FT= Front-Thunderstorm, CFT= Triple storm.

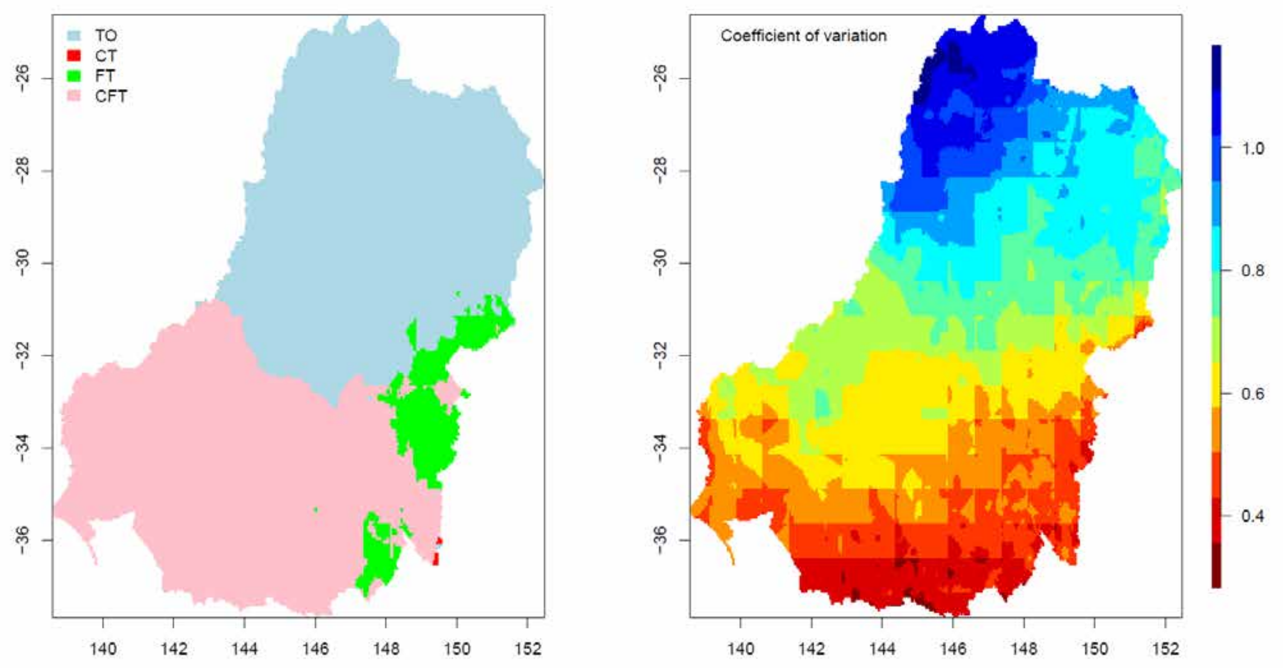

Figure 6. The largest weather type to total annual rainfall (left column) and its coefficient of variation among 7 weather types (right column). TO= Thunderstorm-Only, CT= Cyclone-Thunderstorm, FT= Front-Thunderstorm, CFT= Triple storm

Figure 7 shows an example of rainfall contribution from different weather types in one 5 km grid cell in NMDB and another in the SMDB. The cells used in the example are selected because they show how different the contributions of weather patterns can be in the NMDB and the SMDB, with the cell in the NMDB having 40% of rainfall coming from TO weather, whereas the cell in the SMDB shows more heterogeneity in weather types to rainfall contribution.

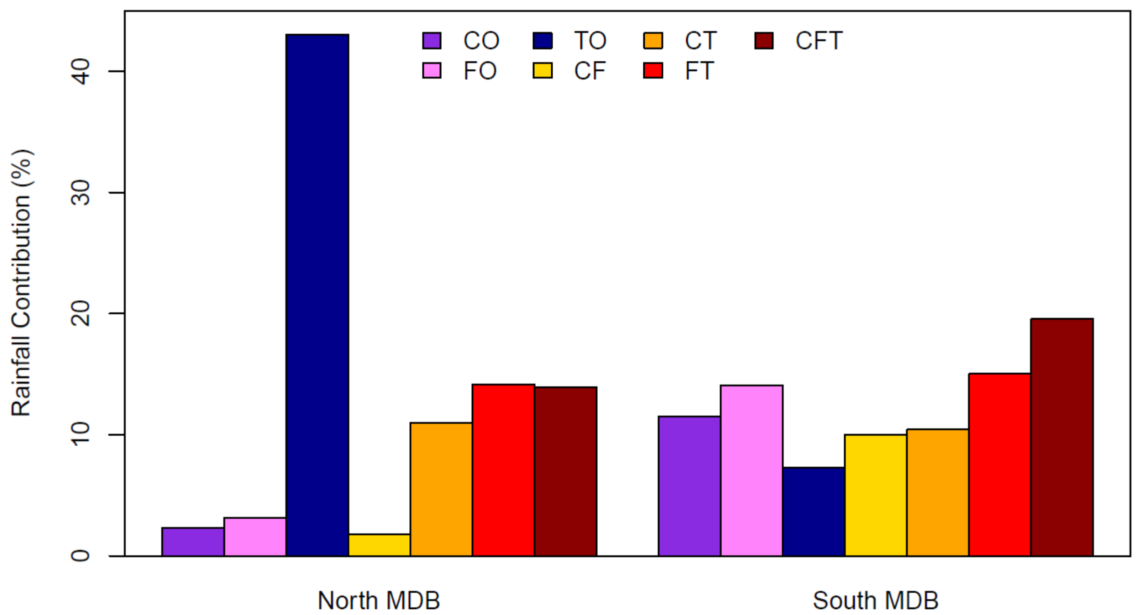

Figure 7. Comparison of rainfall contributions from different weather types in one example 5 km grid cell in the southern and northern MDB, respectively.

Changes in the rainfall attributions to different weather types through time is explored by analysing the attributions in the pre Millennium Drought dataset (1979–2000), Millennium Drought dataset (2001–2009), and post Millennium Drought dataset (2010–2015) (Fu et al., 2023). In the NMDB, the period with uninterrupted negative rainfall anomaly started in 2001 (van Dijk et al., 2013), hence the period 2001–2009 is used to separate the drought period from pre- and post-drought. Overall, the plots in Figure 8 show a wet period before the Millennium Drought, a dry period during the Millennium Drought, and a mixed pattern post Millennium Drought depending on the geographical location. The baseline for the anomaly is the entire study period from 1979 to 2015. It is interesting to note that overall, the post-drought period is much wetter than pre-drought period for the entire MDB, although some areas in the central-north and southwest of the MDB have a negative rainfall anomaly in the post-drought period. Rainfall anomaly amount (mm/year) and percentage (%) always have the same colour and sign for a specific region, but their magnitude could be significantly different due to the spatial heterogeneity in long-term mean annual rainfall.

The spatial distributions of rainfall anomalies from each weather type (Figure 9) are generally consistent with those of total rainfall anomalies (Figure 8) in the three corresponding periods, i.e., a wet period before the Millennium Drought, a dry period during the drought, and a mixed pattern for the post-drought depending on weather types. However, the percentages of rainfall anomalies show different magnitudes (Figure 10) because of the variations of rainfall contributions from different weather types. For example, TO weather type (the largest rainfall weather type for the entire MDB, Figure 3, and the dominant rainfall weather type for the NMDB, Figure 6), shows the largest negative rainfall anomalies in the northwest MDB during the Millennium Drought in terms of rainfall amount (mm/year), but small percentage rainfall anomalies in this region.

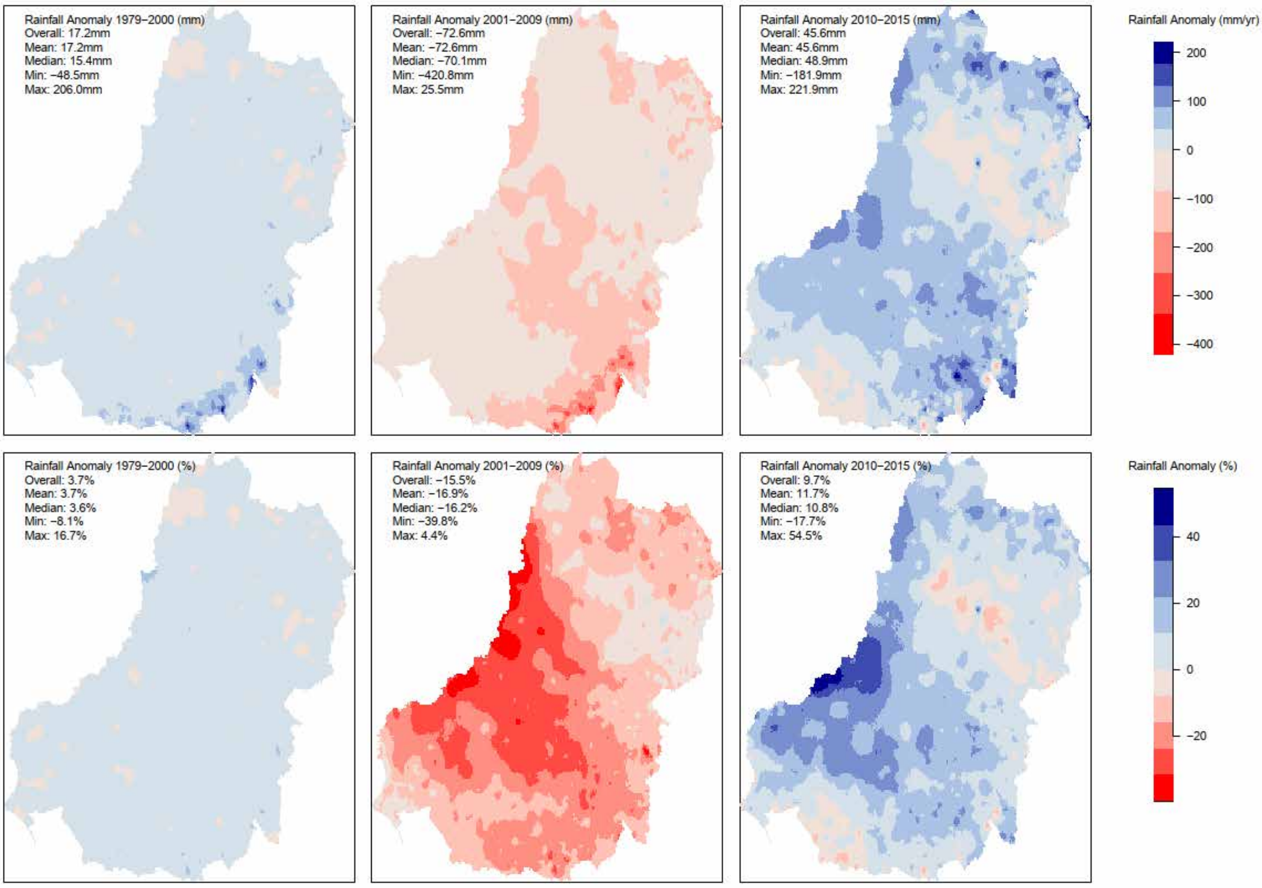

Figure 8 Spatial distributions of rainfall anomalies (mm, first row and %, second row) for pre- (first column, 1979–2000), drought (second column, 2001–2009) and post-drought (third column, 2010–2015) periods. The baseline is the entire study period 1979–2015 due to data availability of weather type datasets.

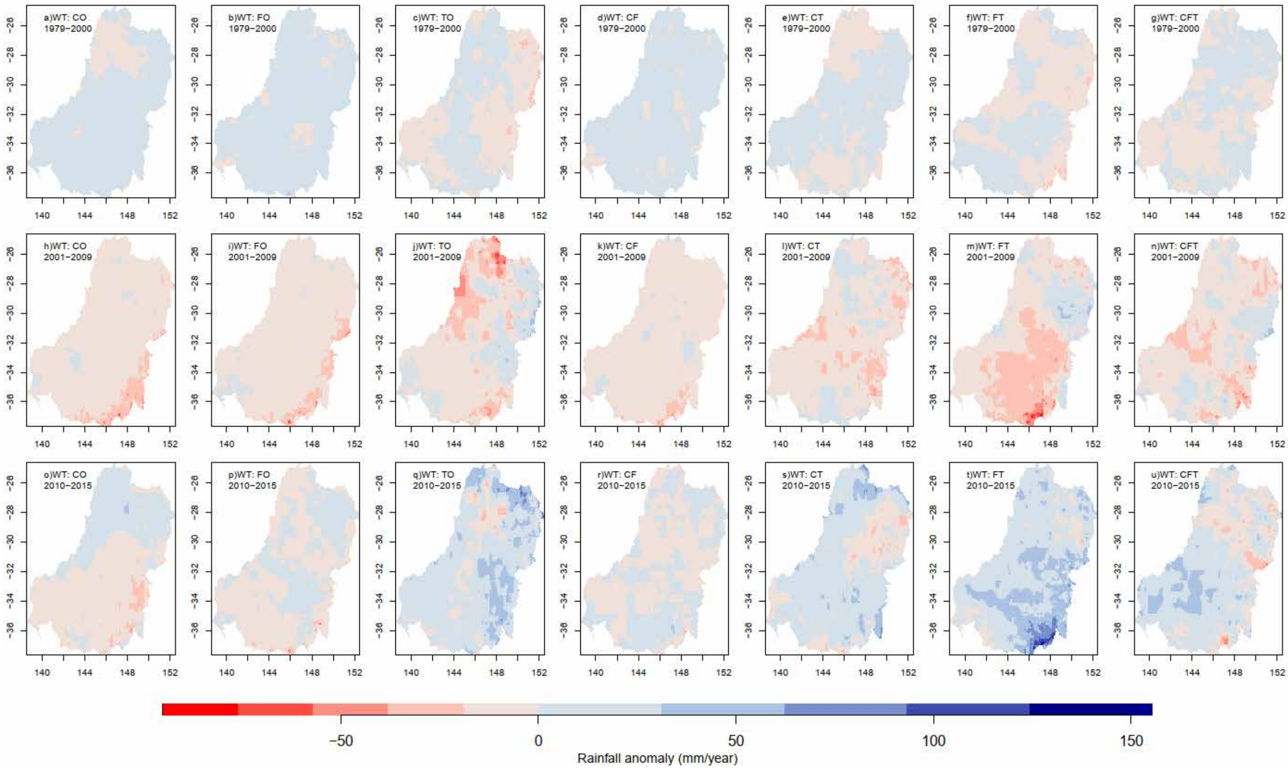

Figure 9. Spatial distributions of rainfall anomalies (mm/year) from each weather type (column) for pre-drought (first row, 1979–2000), drought (second row, 2001–2009) and post-drought (third row, 2010–2015) periods. CO= Cyclone-Only, FO= Front-Only, TO= Thunderstorm-Only, CF= Cyclone-Front, CT= Cyclone-Thunderstorm, FT= Front-Thunderstorm, CFT= Triple storm.

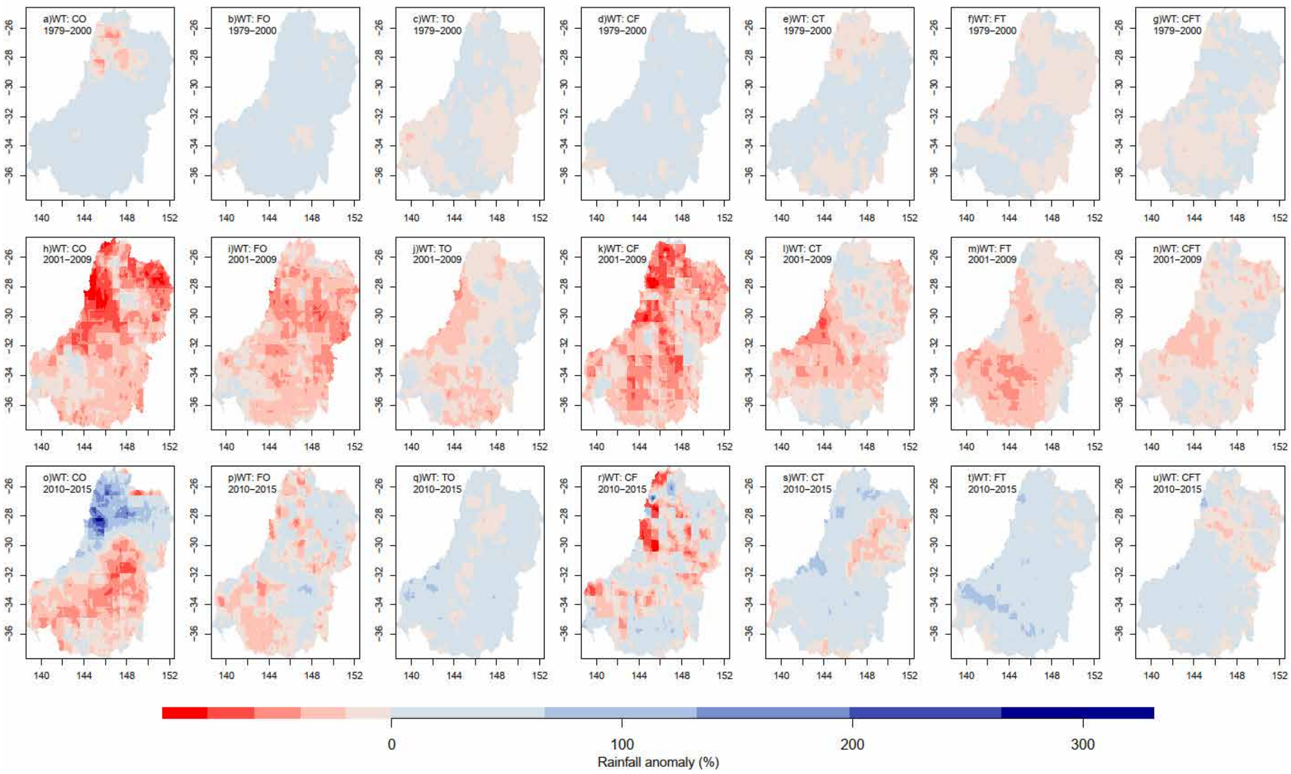

Figure 10. Spatial distributions of rainfall anomalies (%) from each weather type (column) for pre-drought (first row, 1979-2000), drought (second row, 2001-2009) and post-drought (third row, 2010-2015) periods. CO= Cyclone-Only, FO= Front-Only, TO= Thunderstorm-Only, CF=Cyclone-Front, CT=Cyclone-Thunderstorm, FT=Front-Thunderstorm, CFT=Triple storm.

3 Catchment hydrological shifts in rainfall-runoff

Many studies (Chiew, 2006; Peterson et al., 2021; Saft et al., 2016) have used streamflow in unimpaired catchments (particularly in the SMDB and Victoria) to assess the effects of long dry periods on the rainfall-runoff relationship. Some studies (Ajami et al., 2017; Deb et al., 2019) suggest that endogenous catchment characteristics (vegetation, slope, groundwater table) can be equally important as climate drivers in explaining shifts in the rainfall-runoff relationship leading to non-stationarity.

Here, a similar approach as in Saft et al. (2016) was followed to characterise shifts in the rainfall-runoff relationship for curated streamflow data from 110 catchments in the MDB, 37 in the NMDB and 73 in the SMDB (see Figure 1). The analysis was conducted for 1985–2020 and assessed shifts in the annual rainfall-runoff relationship and their change magnitude also for the post-drought period. The data used here included the SILO gridded daily rainfall (Jeffrey et al., 2001) and mean annual catchment streamflow and boundaries chiefly from the Bureau of Meteorology's Hydrologic Reference Stations (HRS, Zhang et al., 2013). Data provenance and criteria for catchment selection can be found in Appendix A , which includes criteria for data availability during the evaluation period, removal of catchments presumably regulated, and catchments where mean annual rainfall may be more uncertain according to different rainfall datasets. To account for spatiotemporal differences in monthly rainfall, the calendar year (i.e., January to December) was used to aggregate rainfall and streamflow for the SMDB catchments, and the July to next year's June was used to aggregate rainfall and streamflow for the NMDB catchments.

Firstly, pre-drought, drought and post-drought periods for each catchment were determined for 1985–2020, period chosen as it maximises data availability. These are periods generally used in southeastern Australia (Peterson et al., 2021) to characterise the time before and after Millenium Drought. The method of Killick et al. (2012) was used herein to separate these periods, which employs a parametric global approach that measures how much a metric deviates from an empirical estimate calculated at every observation. Two metrics were assessed: first the annual cumulative runoff coefficient (Q_{coeff}), which was used to detect the year in which the slope of the Q_{coeff} curve changed statistically significantly (p<0.01 or 90% confidence); second the annual runoff timeseries (Q), which was used to detect the year when the mean changed statistically significantly. The number of changes were limited to 3 as to coincide with the notion of pre-drought, drought and post-drought periods. The years with changes obtained from the two metrics were compared and manually adjusted by visual inspection, when required. Note that from 2017 to 2019, the NMDB experienced the 'Tinderbox Drought' (Devanand et al., 2024) and this is considered in the interpretation of results.

Secondly, linear regression models optimised to have the same slope were fitted to mean annual rainfall (P) and mean annual Q pairs in each of the three periods. Using the same slope is a condition to quantify the magnitude of shift across rainfall regimes (Saft et al., 2016). Prior to this, as Q data are positively skewed, they were transformed using Box-Cox (Box and Cox, 1964) to enable statistical techniques that rely on data being normally distributed. The resulting linear regression models were assessed for autocorrelation in residuals using the Durbin-Watson test

(Durbin and Watson, 1950), showing that only 9 periods of the 330 total periods had Durbin-Watson test with p<0.01 (90% confidence), hence we did not transform the data further to account for residual autocorrelation. The intercepts of the linear regressions was assessed for significant changes (at the 90% and 95% confidence levels) using an analysis of inter-model comparison covariance.

Thirdly, the magnitude of shift *M* (expressed in percentage) across rainfall regimes for different periods was computed following Saft et al. (2016):

$$\boldsymbol{M}(\%) = \frac{\boldsymbol{Q_{dry}(P')} - \boldsymbol{Q_{exp}(P')}}{\boldsymbol{Q_{exp}(P')}} \times \mathbf{100} \qquad \text{Equation 1}$$

where Q_{dry}, for example, represents annual runoff during the dry (or drought) period for a reference rainfall (*P'),* and Q_{exp} denotes the expected annual runoff for its corresponding *P'*. *P'* is defined as half of the sum of the minimum and average annual rainfall of the entire annual P record (1985 to 2020). *M* is determined individually for each catchment. It is important to highlight that *M* does not reflect the overall decline in runoff during the assessed period. Instead, it signifies the extra reduction in runoff during the assessed period in comparison to other similarly dry years in historical records, expressed as a percentage of the expected runoff. This is described in more detail in Saft et al. (2016), particularly Figure 5 in the paper.

Fourthly and finally, the linear regression models, statistical significance and *M* provided the basis for the classification of rainfall-runoff changes in the 110 catchments into: (i) catchments with non-significant decline (statistical significance of $\alpha < 0.10$ is used throughout), (ii) catchments with significant decline and recovered (non-significant decline in post-drought with respect to pre-drought and magnitude shift M in post-drought ≤20%), (iii) catchments with significant decline and partially recovered (non-significant decline in post-drought with respect to pre-drought and magnitude shift M in post-drought >20% but ≤40%) and, (iv) catchments with significant decline that have not recovered (significant decline in post-drought with respect to pre-drought).

For illustrative purposes, examples of results for MDB catchments are shown in Figure 11. The three distinct periods are determined for annual P and annual Q for catchment 418021 (first row, first column in Figure 11a, catchment located in the Gwydir river valley in the NMDB) using the cumulative Q_{coeff} curve as assessed by the Killick et al. (2012) method (first row middle column in Figure 11a). The regression models suggest (first row right column in Figure 11a) that in this catchment, rainfall-runoff has not shifted from the pre-drought period (1990–1998, blue line) to the drought period (1999–2009, red line), thereby similar rainfall led to similar runoff during the drought period. The shift in intercept from pre-drought to drought (from -2.26 to -2.41 in Box-Cox transformed data) is not statistically significant. The post-drought period (2010–2020, green line) shows again similar rainfall resulting in similar runoff. The shift in intercept from pre-drought to post-drought (from -2.26 to -2.30) is not statistically significant. The coefficient of determination (r^2) shows that the linear models explain >0.6 of the variance for the pre-drought and post-drought models, but only 0.3 in the drought model as the data dispersion deviates more from the linear model adjusted to this period. Thus, catchment 418021 is typified as a catchment with non-significant decline.

Regression models for catchment 416003 (located in the Border Rivers valley in the NMDB, Figure 11b) show that the rainfall-runoff relationship significantly shifted from the pre-drought to the drought, with a statistically significant shift (with the * symbol denoting 90% confidence) in intercept changing from -1.62 to -2.15, but recovered to the pre-drought rainfall-runoff relation, with intercept changing significantly (with ** symbol denoting 95% confidence) from -1.62 to -1.43 (i.e., more runoff from a similar amount rainfall). In this case all regression models have a r^2>0.7. This catchment is typified as a catchment with significant decline which has recovered post-drought.

Regression models for catchment 412066 (located in the Lachlan River valley in the SMDB, Figure 11c) show a significant decline so that the rainfall-runoff relationship significantly shifted from the pre-drought to the drought, with a significant shift in intercept changing from 0.71 to 0.41. It did not recover to the pre-drought rainfall-runoff relationship, with a significant shift in intercept changing from 0.71 to 0.43. An r^2>0.7 shows that the linear models explain >0.7 of the variance for the pre-drought and post-drought models, but only 0.38 in the drought model. This catchment is typified as a catchment with significant decline which has not recovered post-drought.

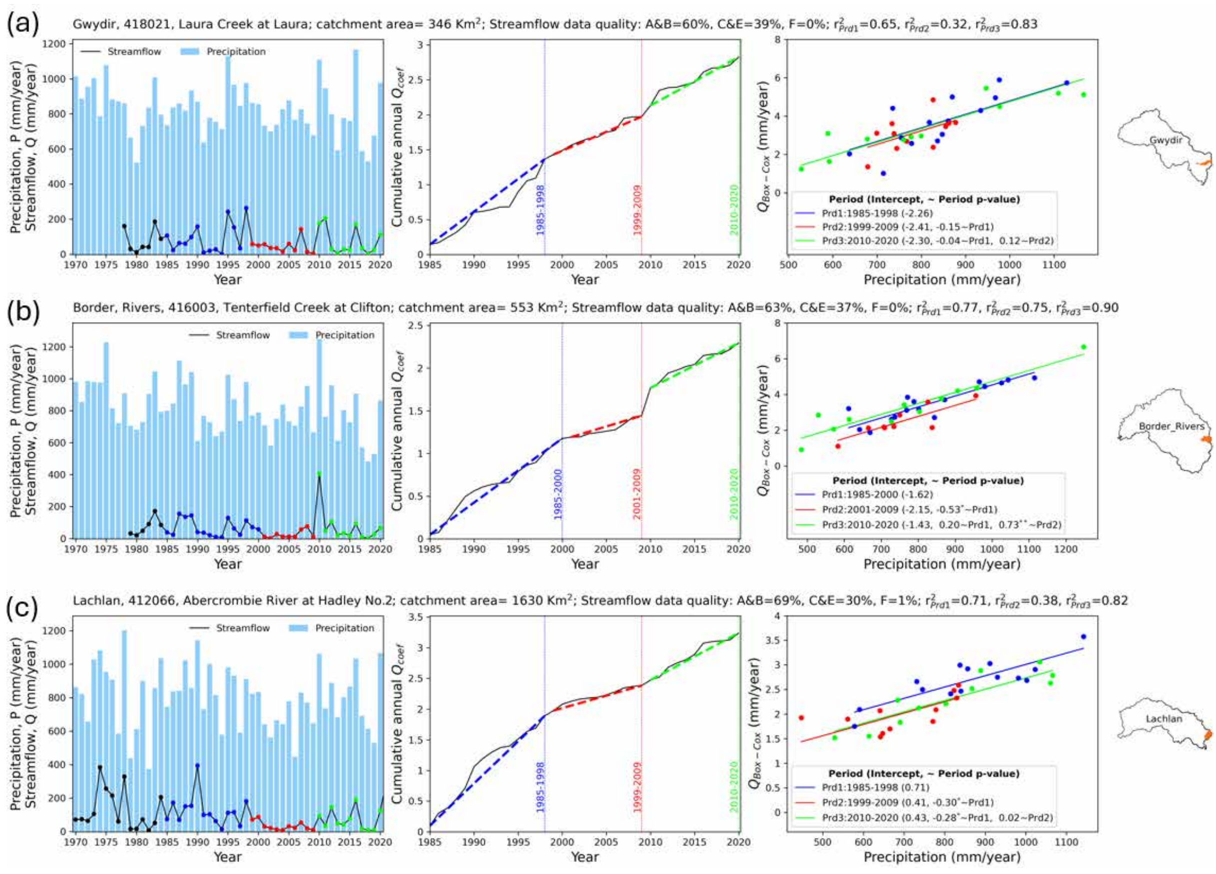

Figure 11. Left column: Annual timeseries of rainfall (P, blue bars) and streamflow Q. Middle column: cumulative annual runoff coefficient (Qcoeff). Right column P-Q (Box-Cox transformed) scatterplot including information on the intercept and p-value of the intercept difference between periods (* significant at the 90% confidence level, ** significant at the 95% confidence level). The blue lines in each of the plots denote the 'pre-drought' period, the red denote the 'drought' and green the 'post-drought'. Catchment information including name, area and streamflow quality are found above each catchment panel. The catchment geographic location within the river valley is shown in the map (see Figure 1 for location of the valley within the Murray-Darling Basin).

The summary results depicting geographic rainfall-runoff shifts in the MDB for the 110 catchments are shown in Figure 12. Significant shifts in the rainfall-runoff relationship (more runoff to less runoff for similar rainfall) occurred mainly in the SMDB (73 catchments), with 49 catchments (67%) having significant declines without recovery, 7 (10%) with significant declines and have partially recovered, 5 (7%) with significant declines and have fully recovered and 12 (16%) with non-significant declines. Conversely, in the NMDB (37 catchments), no catchments had significant declines without recovery, 2 (5%) had significant declines and partially recovered, 5 (14%) with significant declines and recovered and 30 (81%) had non-significant declines.

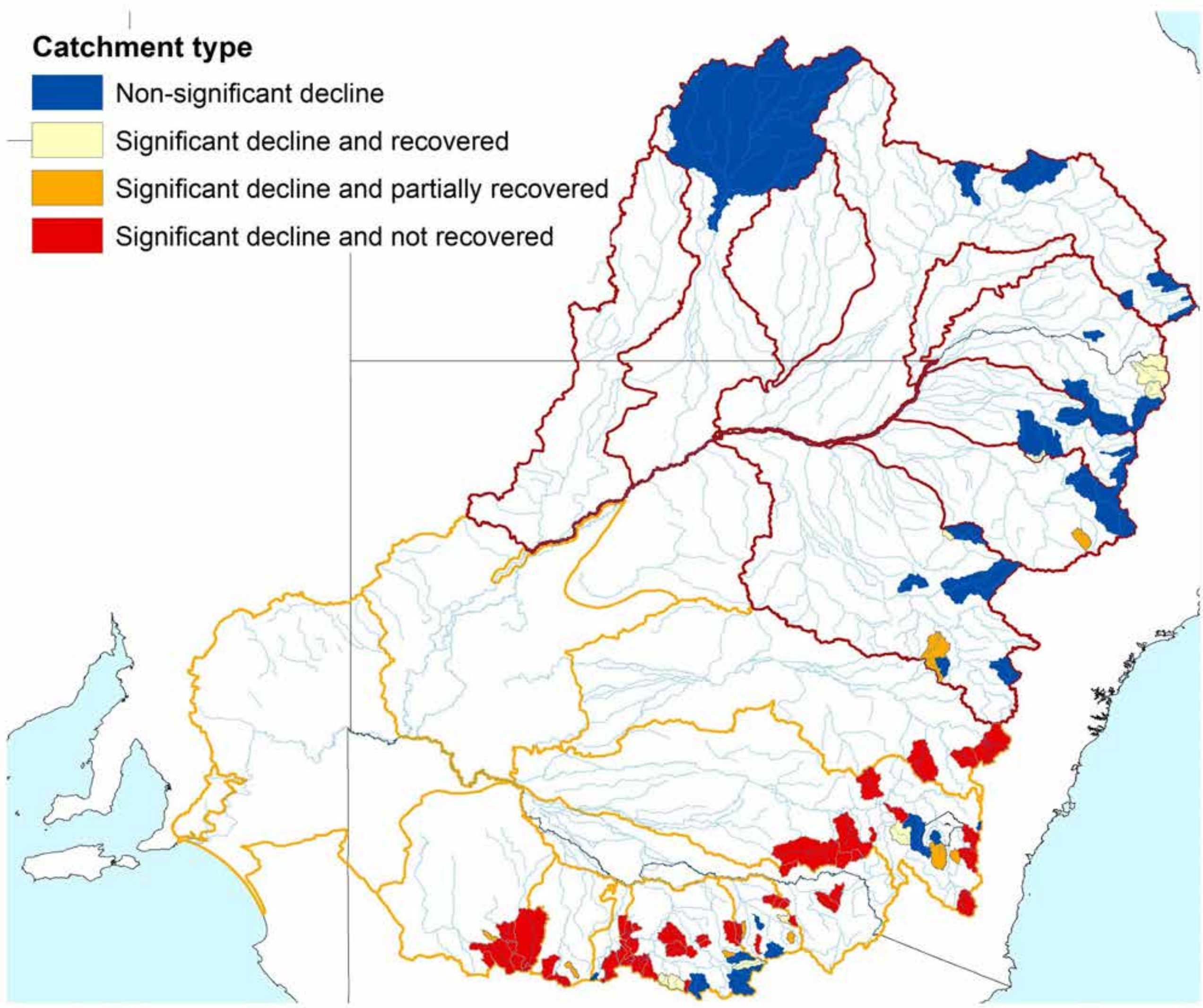

Figure 12. Summary of catchment rainfall-runoff shifts. Significance (at the 90% confidence level) is determined from the intercept of the linear regressions in each period. Shown are river valley divisions of the Murray-Darling Basin (NMDB valleys in maroon outline, SMDB valleys in orange outline) included in the analysis, 37 in the NMDB and 73 in the SMDB.

Figure 13 shows the magnitude shift (%) for the 110 catchments in the MDB across two periods, from pre-drought to drought, and from pre-drought to post-drought. An inset map shows the mean annual runoff (1990−2020). Inspecting the shift maps alongside the mean annual runoff map highlights, not surprisingly, the role of climate in modulating shifts, with smaller magnitude shifts occurring in ‘wet’ catchments (Q>150 mm/year) in the SMDB. Several of these wet catchments also did not show significant shifts in the rainfall-runoff relation (Figure 12). Conversely, larger magnitude shifts occurred in ‘dry’ catchments (Q<50 mm/year).

Across river valley divisions in the NMDB, most catchments have recovered, and in some cases the shift magnitudes post-drought were positive (i.e. more runoff than pre-drought for a similar amount of rainfall). In the SMDB, catchments in Wimmera, Loddon-Avoca, to the west in the Goulburn-Broken, and several catchments in the Murrumbidgee (with the exception of catchments in the high-rainfall area, Figure 1) and Lachlan have not recovered, and the magnitude of shifts persist post-drought.

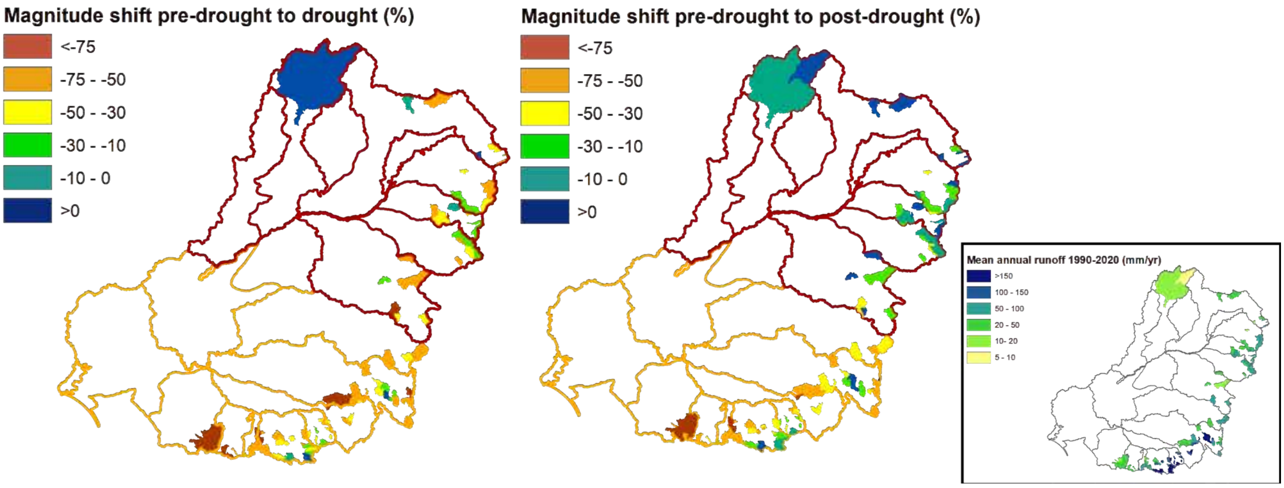

Figure 13. Magnitude shifts (%) from pre-drought to drought and pre-drought to post-drought for the 110 catchments in the MDB. Shown are river valley divisions of the Murray-Darling Basin (NMDB valleys in maroon outline, SMDB valleys in orange outline)The inset shows mean annual runoff (1990–2020) for the 110 catchments.

A summary of results per river valley, including number of catchments per type and statistics on magnitude changes, is presented in Table 2. In the NMDB, the average pre-drought to drought percentage magnitude shift (M) was -37.4%, and the pre- to post-drought was 19.8%, i.e., the shift was to comparatively more annual runoff for similar rainfall. Only two catchments in the Macquarie-Castlereagh and Namoi, respectively, significantly declined and partially recovered. Conversely, in the SMDB, the average pre-drought to drought percentage magnitude shift (M) was -54.8%, and the pre- to post-drought was -44.5%. On average, the largest M pre-drought to drought shifts were observed in catchments located in Wimmera (-85.5%), Loddon-Avoca (-77.5%) and Campaspe (-67.2%). All catchments located in the SMDB in western Victoria, and catchments located in the western Goulburn-Broken have also largely not recovered.

The results highlight that hydrological non-stationarity played a significant role in the SMDB during the Millenium Drought, particularly in catchments located in the drier western SMDB, and its effects are lingering therein. Conversely, non-stationarity has not markedly affected catchments in the NMDB, and most catchments that had a shift in the rainfall-runoff relation have largely recovered and in some cases shifted to a wetter state (i.e., comparatively more runoff from a similar amount of rain). The regression analysis included years during the Tinderbox drought (2017–2019) which largely affected NMDB catchments. When compared to the Millennium Drought (1997–2009), the duration of the Tinderbox drought did not result in a significantly changed rainfall-runoff relation, as it was preceded by relatively wet conditions, particularly during the La Niña of 2010–2011. This period brought significant rainfall and flooding to many parts of the MDB, replenishing water storages and increasing soil moisture levels, before the below-average rainfall in 2017 and heightened temperatures, which caused rapid depletion of surface water storages and soil moisture levels leading to the Tinderbox drought.

Chapters 4 and 5 explore the role of vegetation dynamics and land use in shaping the rainfall-runoff relationship. Chapter 4 focuses on changes in leaf area index (LAI) and actual evapotranspiration (ET_a) using remotely sensed data, while Chapter 5 integrates these dynamics into rainfall-runoff models, also incorporating farm dams and multitemporal satellite-derived LAI. Sensitivity analysis and scenario modelling are used to quantify the impacts of climate, vegetation, and land use changes on hydrology.

Table 2. Summary of rainfall-runoff shifts per river valley, including type (NSD=non-significant decline, SDR=significant decline and recovered, SDPR=significant decline and partially recovered, SDNR=significant decline and not recovered) and statistics about magnitude shifts (M)

	NSD	SDR	SDPR	SDNR	Pre- to drought average M (%)	Pre- to post-average M (%)	Pre- to drought max M (%)	Pre- to post-max M (%)	Pre- to drought min M (%)	Pre- to post-min M (%)
NMDB	30	5	2	0	-37.4	19.8	13.2	250.7	-84.6	-48.2
Border Rivers	5	3	0	0	-36.7	-11.6	-16.3	29.8	-56.1	-48.2
Condamine-Balonne	7	0	0	0	-29.1	90.0	8.4	196.5	-51.6	-15.6
Gwydir	7	1	0	0	-38.9	-0.7	-8.6	34.9	-84.6	-31.7
Macquarie-Castlereagh	5	1	1	0	-53.4	4.2	-29.5	71.8	-76.1	-47.6
Namoi	4	0	1	0	-44.7	-15.3	-26.1	-0.1	-56.8	-30.2
Warrego	2	0	0	0	10.9	124.1	13.2	250.7	8.6	-2.6
SMDB	12	5	7	49	-54.8	-44.5	6.0	27.9	-99.2	-91.8
Campaspe	1	0	0	5	-67.2	-62.5	-17.1	-26.7	-87.5	-76.0
Goulburn-Broken	4	3	1	13	-47.2	-43.0	6.0	4.4	-84.6	-83.6
Lachlan	0	0	0	3	-52.8	-47.4	-41.6	-43.7	-66.2	-50.9
Loddon-Avoca	0	0	1	4	-77.5	-64.5	-70.7	-33.1	-86.8	-82.2
Murray	0	0	0	8	-54.2	-47.5	-37.7	-31.3	-88.1	-91.8
Murrumbidgee	5	1	2	8	-50.8	-27.1	3.6	27.9	-87.4	-69.0
Ovens	2	1	2	3	-37.6	-30.7	-23.7	-8.3	-45.7	-53.4
Wimmera	0	0	1	5	-85.5	-74.8	-77.6	-62.4	-99.2	-84.5

4 Changes in vegetation dynamics

4.1 Leaf Area Index

Changes in vegetation 'greening' due to increases in CO_2 have been observed in shrubland ecosystems in Australia (Winkler et al., 2021) and catchments in the MDB (Ukkola et al., 2016). There are also areas within the MDB that have experienced 'browning' (Rifai et al., 2022).

Greening can increase vegetation transpiration, but increased vegetation water use efficiency under higher atmospheric CO_2 will reduce transpiration per vegetation unit. The net response depends on vegetation type, e.g., forests and grassland. To disentangle the role of forest and grasses in terms of vegetation greening or browning, we evaluated and tested a novel long-term (1982–2020) LAI dataset, LAI4G (Cao et al., 2023) which covers the pre-drought, drought and post-drought periods. LAI was separated into two components, persistent and recurrent LAI, according to Donohue et al. (2009). Broadly, persistent LAI (LAI_{per}) is ascribed to species that are active year-round and that display relatively little seasonal variation in canopy structure like evergreen trees. Conversely, recurrent LAI (LAI_{rec}) is ascribed to vegetation functional types comprised of species that operate in (often annual) cycles of activity and dormancy like grasses. The analysis was performed using monthly data from 1982–2020 and mean values and trends for the cool months (May to October) and the warm months (November to April).

Figure 14 shows the cool months mean persistent and recurrent LAI and associated trends in southeastern Australia including the MDB. The forested areas can clearly be seen as having a higher (> 3 m^2/m^2 per period) LAI_{per} than LAI_{rec}. Conversely, LAI_{rec} patterns are high (> 3 m^2/m^2 per period) in the 'arch' of the dryland cropping areas (mainly winter cereals). Significant positive trends (at the 95% confidence level) in LAI_{per} (>0.02 m^2/m^2 per period) or greening are found in the forested areas of the SMDB. On the other hand, significant positive trends in LAI_{rec} (>0.015 m^2/m^2 per period) occur in the southern grassland/cropland areas of the SMDB. Some negative (browning) trends (<-0.015 m^2/m^2 per period) are also observed in the east, straddling from the NMDB to the SMDB.

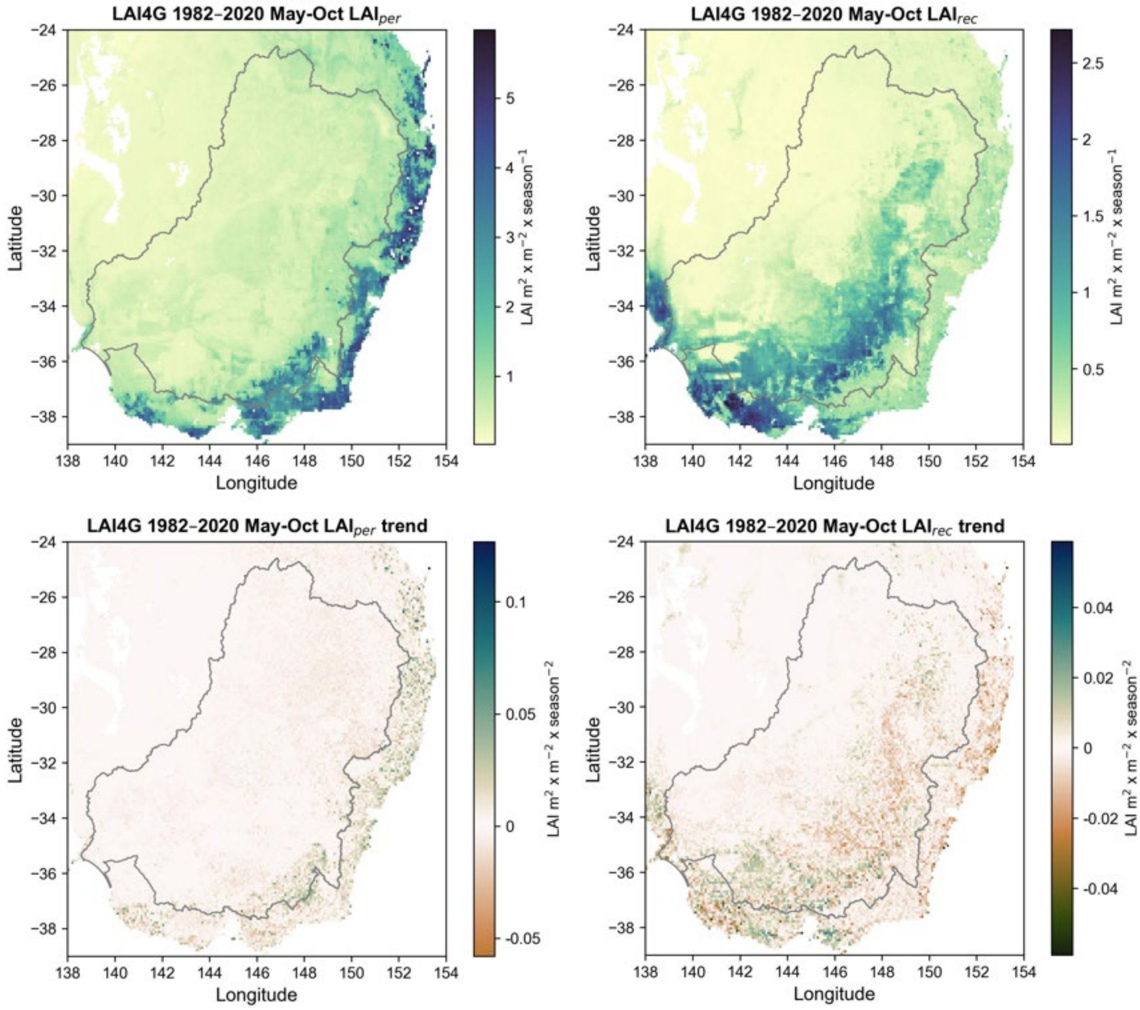

Figure 14. Mean persistent and recurrent Leaf Area Index (LAI) computed for the cool months (May to October) in southeastern Australia, with the MDB boundaries in grey.

Figure 15 shows the warm months mean LAI_{per} and LAI_{rec} and associated trends in the MDB and southeastern Australia. As for the cool months, the forested areas in southeastern Australia can clearly be seen as having a higher LAI_{per} (> 3 m^2/m^2 per period). Besides in the forested areas, the highest LAI_{rec} (> 1 m^2/m^2 per period) occurs in the northeast of the NMDB. Trends for the LAI_{rec} during the warm months are of lower magnitude than during the cool months and are mostly non-significant (at the 95% confidence level). There is a significant greening trend in LAI_{per} during the warm months (>0.015 m^2/m^2 per period), like the cool months in the forested areas in the SMDB, but a smaller trend compared to the cool months in the NMDB.

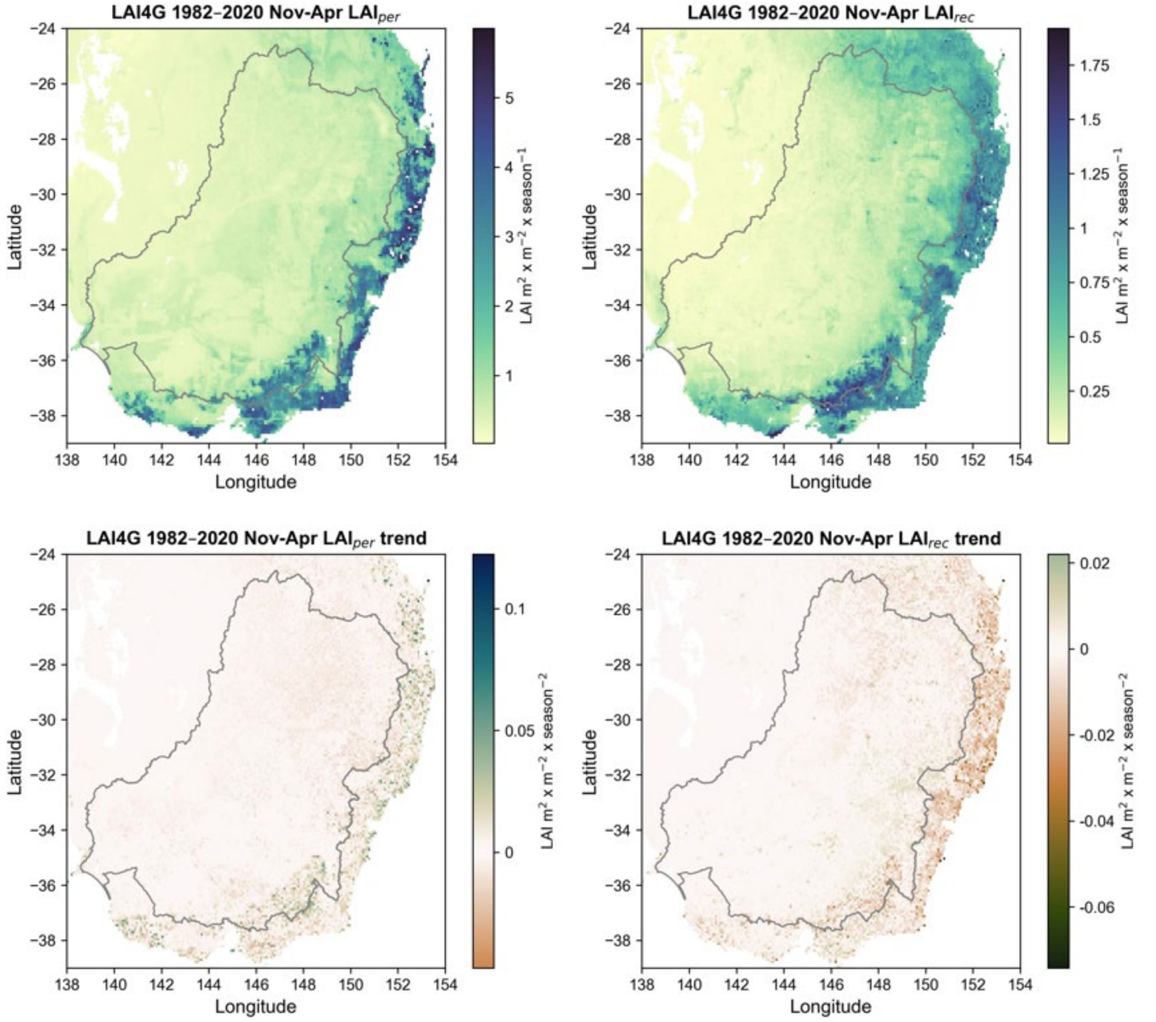

Figure 15. Mean persistent and recurrent Leaf Area Index (LAI) computed for the warm months (November to April) in southeastern Australia, with the MDB boundaries in grey.

LAI, LAI$_{per}$ and LAI$_{rec}$ were further investigated for the 110 MDB catchments in which the rainfall-runoff relationship was analysed (Chapter 3) using the shifts in rainfall-runoff relationships to segregate the catchments and the pre-drought, drought and post-drought periods. The summary results in Figure 16 shows that for the non-shifted catchments (n=42, first column plots), which are mostly located in the NMDB (Figure 12), the median LAI and LAI$_{per}$ values have slightly declined (~5%, from 1.63 to 1.55 m^2/m^2 for annual LAI), from the pre-drought to the drought period, in annual and in cool and warm months, but not so much for LAI$_{rec}$. The variance (the box height, which represents the interquartile range, IQR) has increased in both LAI and LAI$_{per}$ in the cool months towards higher LAI and LAI$_{per}$. Also, there has been an increase in the post-drought when compared to the drought period for LAI and LAI$_{per}$ but not much for LAI$_{rec}$.

For shifted and recovering/recovered catchments (n=19, second column plots, Figure 16), which are located both in the NMDB (7) and SMDB (12), LAI and its components follow similar patterns as for non-shifted catchments, with slight decreases in the median LAI (~2%, from 1.88 to 1.85 m^2/m^2 for annual LAI) and LAI$_{per}$ from the pre-drought to the drought period and then a slight increase in the post-drought period, the variance however has remained similar over the three periods.

For shifted and non-recovered catchments (n=49, third column plot), which are all located in the SMDB, the median LAI and LAI_{per} values have declined slightly more pronouncedly (~7%, from 1.99 to 1.86 m^2/m^2 for annual LAI), but LAI_{rec} has not changed much. Again, post-drought values exceeded pre-drought values, with median LAI_{per} increasing from 1.26 m^2/m^2 to 1.36 m^2/m^2 (~8%), with LAI_{rec} values not increasing much. In these catchments, variability has not changed as much as in the non-shifted catchments.

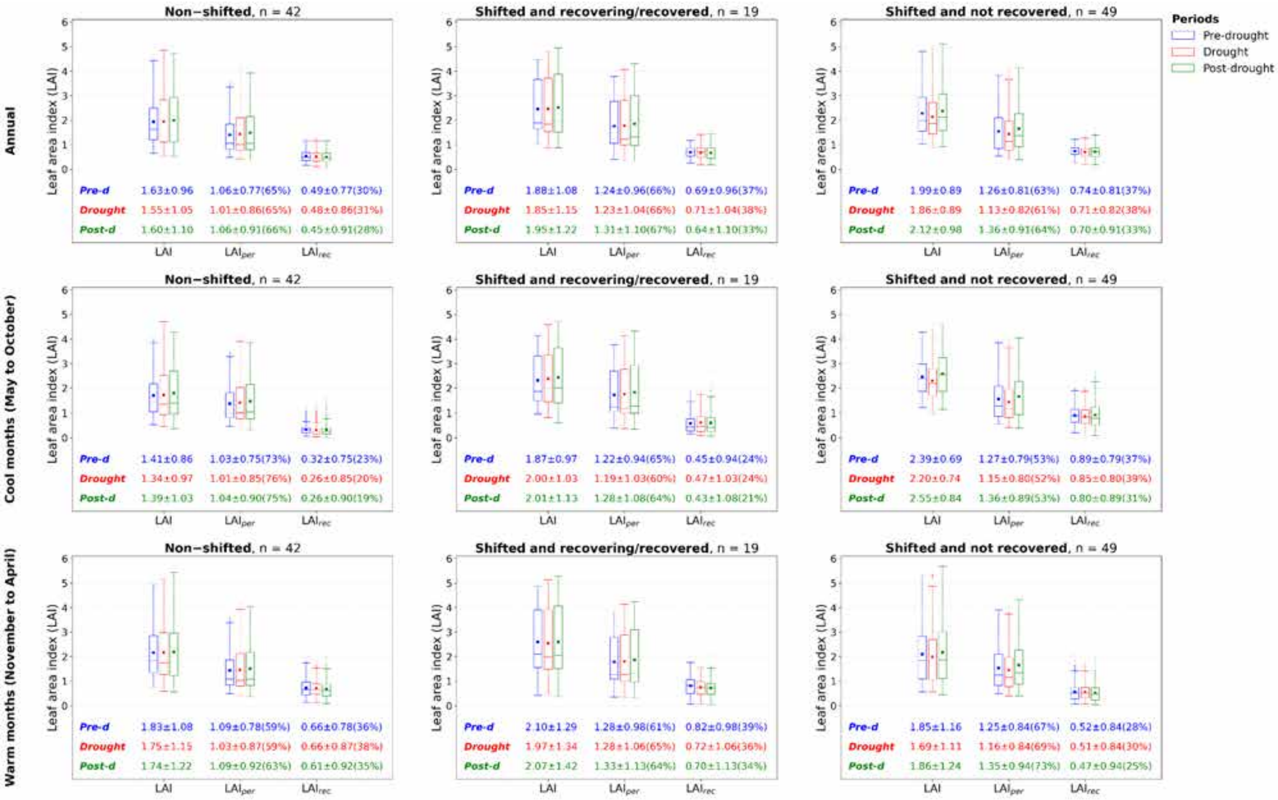

Figure 16. Boxplots of persistent (LAI_{per}) and recurrent (LAI_{rec}) LAI for the 110 catchments in the MDB, segregated by their shifts in the rainfall-runoff relation (Chapter 3). Periods are divided into pre-drought (Pre-d, blue boxplots), drought (Drought, red boxplots) and post-drought (Post-d, green boxplots). The box represents the interquartile range (IQR), lines the median value and the dot the mean value. Whiskers extend from the quartiles to the 5th and 95th percentiles. Numbers below the boxplots show the median and standard deviation for each period, while values in percentages for LAI_{per} and LAI_{rec} refer to the percentage from the mean LAI.

Leaf Area Index (LAI), along with its persistent and recurrent components, are utilised as inputs into the rainfall-runoff modelling framework in Chapter 5 to evaluate their impact on runoff dynamics, enabling a comprehensive assessment of how vegetation structure and its temporal variations influence runoff.

4.2 Actual Evapotranspiration

Changes in rainfall and vegetation dynamics affect the magnitude and partitioning of actual evapotranspiration (ET_a). ET_a often declines under dry conditions due to reduced soil moisture supply but can also increase due to evaporative demand and cause rapid depletion of water resources (Zhao et al., 2022). In the water limited MDB, an increase in ET_a can amplify runoff reductions. Satellite-based ET_a models, which capture vegetation dynamics, are generally only available since the 2000s. Of the ET_a products available before the 2000s, only the Global Land Evaporation Amsterdam Model (GLEAM, Martens et al., 2017; Miralles et al., 2011) uses observations of microwave Vegetation Optical Depth (VOD) to compute ET_a. The data are available from 1 January 1980 to 31 December 2022. The data are provided at 0.25° latitude-longitude regular grid (~25 km) and at daily temporal resolution. This spatial resolution is too coarse to be used at catchment scales <1000 km^2. To enable their use in the MDB catchments, GLEAM data were downscaled to 500 m using a downscaled 'evaporative fraction' approach. Firstly, the evaporative fraction ($k_{c,GLEAM}$) for GLEAM was calculated as:

$$\boldsymbol{k_{c,GLEAM}} = \frac{\boldsymbol{ET_{a,GLEAM}}}{\boldsymbol{ET_{p,GLEAM}}}, \qquad \text{Equation 2}$$

where $ET_{a,GLEAM}$ is GLEAM ET_a and $ET_{p,GLEAM}$ is GLEAM potential evapotranspiration (ET_p). The ET_p in GLEAM is calculated using the Priestley-Taylor formulation (Priestley and Taylor, 1972). Secondly, an evaporative fraction is obtained from $k_{c,CRMSET}$ at 500 m resolution using the "CSIRO MODIS Reflectance-based Scaling EvapoTranspiration" (CMRSET) developed by Guerschman et al. (2022). CMRSET scales Priestley-Taylor ET_p via a crop coefficient (Allen et al., 1998) obtained from two remotely sensed indices. For 1989 to 1999, the remote sensing indices are obtained from atmospherically corrected and cloud free surface reflectance, Collection 2, Level 2, Tier 1, from the TM Landsat-5 satellite (Wulder et al., 2016). For 2000 to 2022, the atmospherically corrected and cloud free surface reflectance from the Nadir Bidirectional Reflectance Distribution Function Adjusted Reflectance (NBAR) product from the Moderate Resolution Imaging Spectroradiometer (MODIS, Strahler et al., 1999) satellite (product name MCD43A4 V6.1) was used. All data were resampled to 500 m. Thirdly, a scaling factor at the 500m is computed as:

$$\boldsymbol{k_{c,scaled}} = \frac{\boldsymbol{k_{c,GLEAM}}}{\boldsymbol{k_{c,CMRSET}}}, \qquad \text{Equation 3}$$

Finally, 500 m downscaled $ET_{a,GLEAM}$ is computed as:

$$\boldsymbol{ET_{a,GLEAMscaled}} = \boldsymbol{k_{c,scaled}} \times \boldsymbol{ET_{p,GLEAM}}, \qquad \text{Equation 4}$$

An example of the results of the downscaling procedure for January 1993 is shown in Figure 17. Note how the downscaled data increases the spatial detail, highlighting areas with high ET_a (lakes, watercourses, irrigation, forested areas) and changes the data distribution. The process can result in outliers with very high ET_a in the downscaled product due to instances of very low (<0.001) $k_{c,CRMSET}$ values compared to $k_{c,GLEAM}$. These outliers occur mainly in arid areas to the west of the MDB. These are replaced by a nearest neighbour using a moving window median (in this case of five pixels).

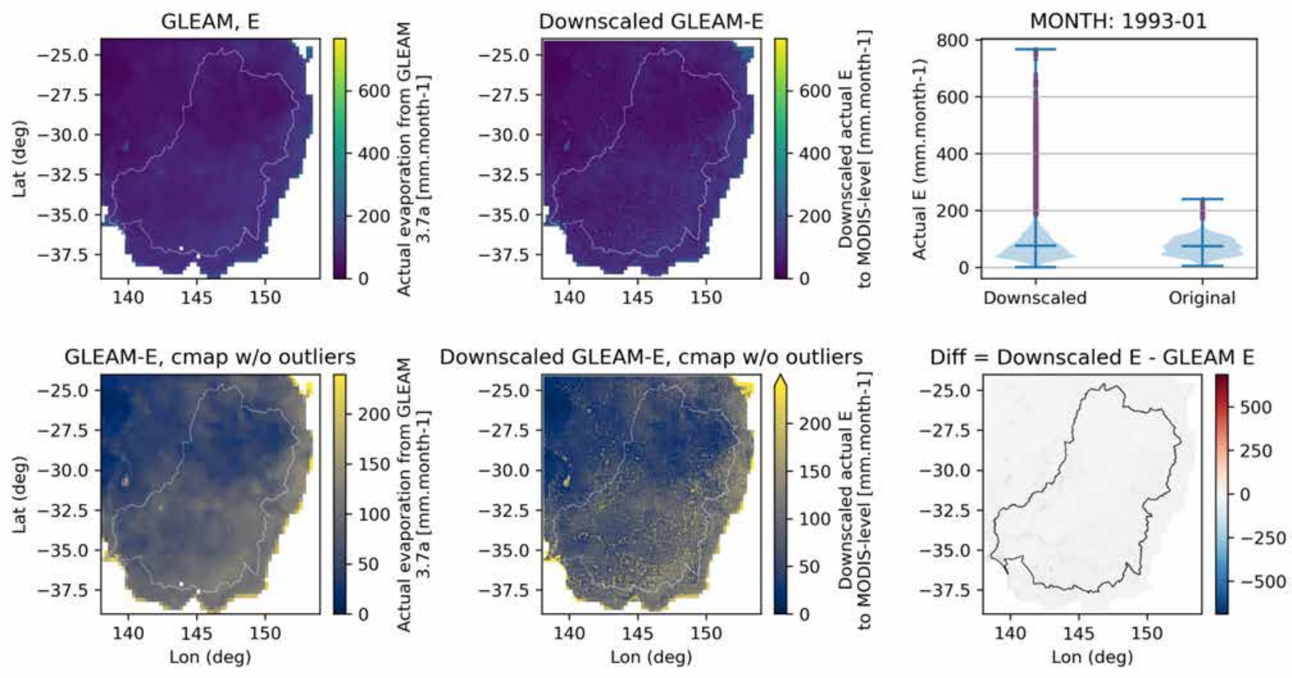

Figure 17. Example of the actual evapotranspiration (ET_a) downscaling procedure for January 1993. The first column on the left shows the original GLEAM data (with and without outliers), the second column shows the downscaled data, and the third column shows a summary of the two datasets

To verify the accuracy in the downscaled data at the catchment scale, a catchment water balance (assuming stationary conditions with no change in soil water storage over each of the periods, i.e., ET_a=P-Q) scatterplots for pre-drought, drought and post-drought periods for different downscaled ET_a data are shown in Figure 18. The overall statistics show that differences between datasets are relatively minor (noting that 91 out of the 110 catchments are smaller than 1,000 km^2). The NMDB catchments are closer to the 1:1 line in the scatterplot, whereas there is some spread in SMDB catchments, particularly for catchments with high (>900 mm/year) ET_a.

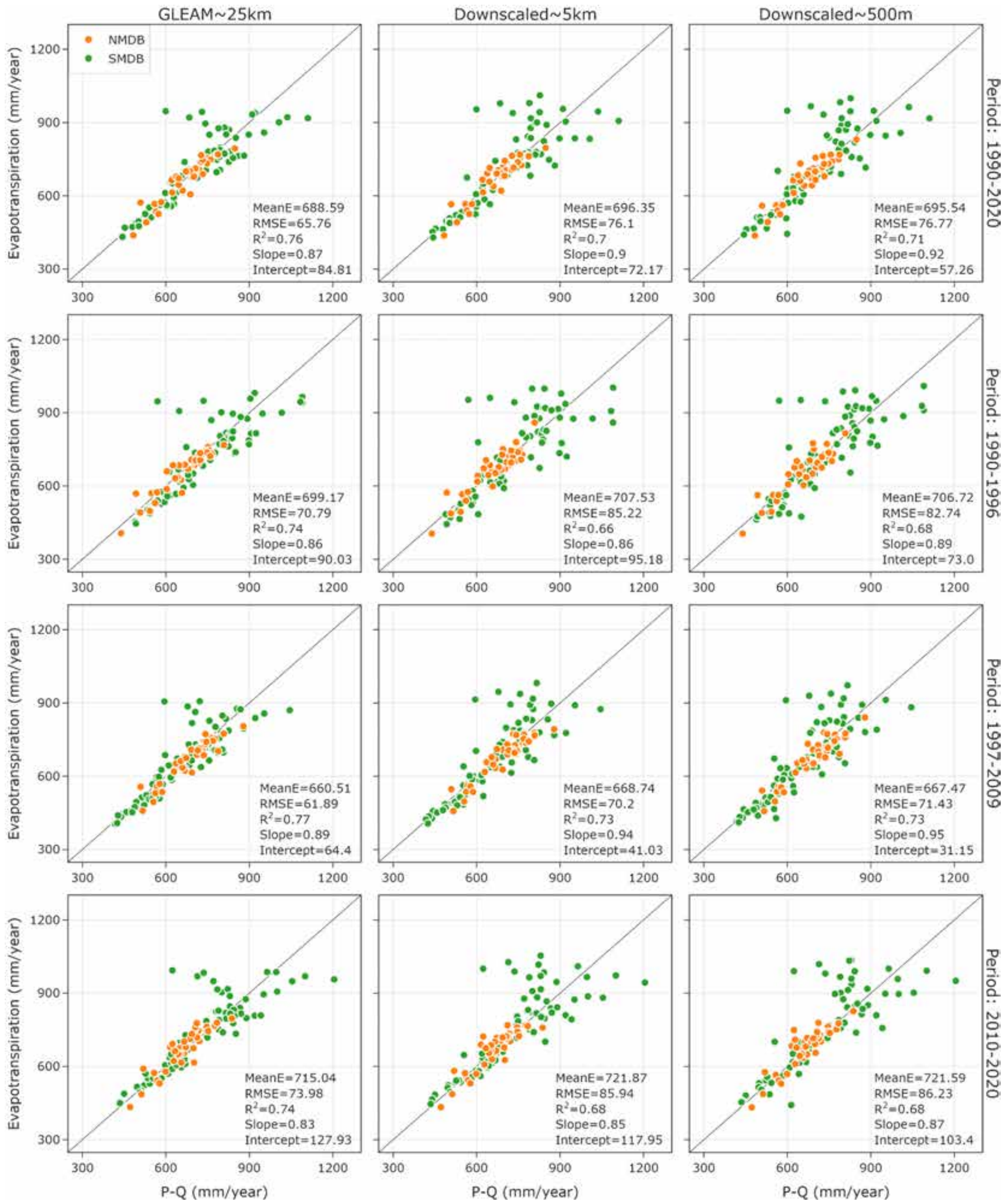

Figure 18. Scatterplot of rainfall (P) minus runoff (Q) against evapotranspiration for the 'pre-drought', 'drought' and 'post-drought' periods. The left column for the original (~25 km spatial resolution) GLEAM ET_a, the middle column for the ~5 km downscaled ET_a and the right column for the ~500 m downscaled ET_a. Goodness-of-fit statistics are reported in each panel. Green catchments are in the SMDB, while orange catchments are in the NMDB.

Overall, for the analysis period 1990–2020, the correlation for NMDB catchments is 0.86 and for SMDB catchments is 0.68, the slopes are 0.98 (NMDB) and 0.91 (SMDB), and the intercepts are 13.01 (NMDB) and 69.8 (SMDB). The results show that the downscaling data provides greater spatial detail with a marginal decrease in accuracy according to the water balance comparison.

The downscaled GLEAM ET_a data, P and Q were investigated in the 110 MDB catchments during the pre-drought, drought and post-drought periods. Figure 19 presents a summary of results as boxplots.

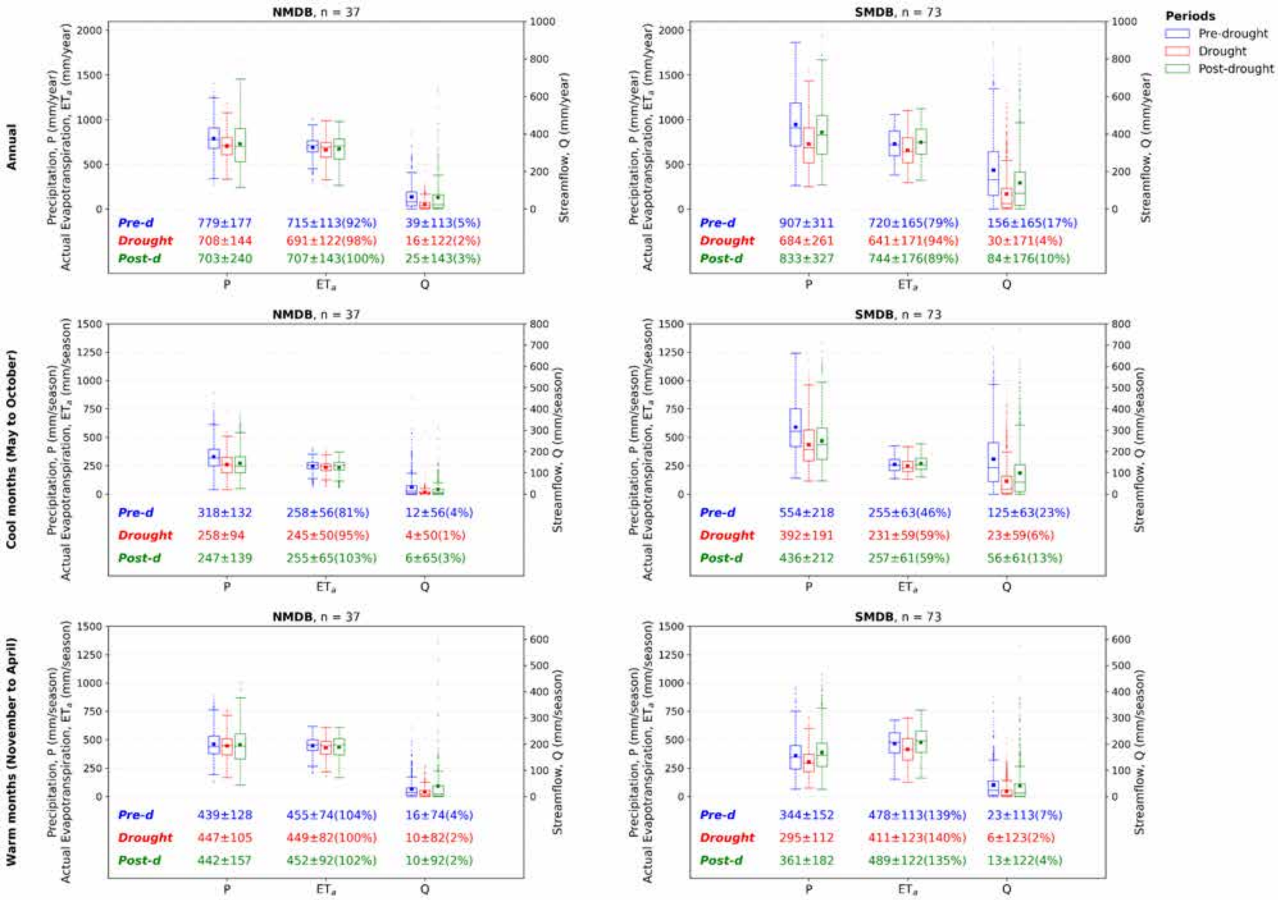

Figure 19. Boxplots of downscaled GLEAM ET_a, rainfall (P) and streamflow (Q) for the 110 catchments in the MDB, segregated by their shifts in the rainfall-runoff relation (Chapter 3). Periods are divided into pre-drought (Pre-d, blue boxplots), drought (Drought, red boxplots) and post-drought (Post-d, green boxplots). The box represents the interquartile range (IQR), lines the median value and the dot the mean value. Whiskers extend from the quartiles to the 5th and 95th percentiles. Numbers below the boxplots show the median and standard deviation for each period, while values in percentages for the different water balance components refer to the percentage from the mean P.

Annually in the NMDB, the ratio of median ET_a to P was 0.91, 0.97 and 1.0 for the pre-drought, drought and post-drought, respectively. Conversely, annually P in the SMDB had a 25% decline from pre-drought to drought, whereas ET_a declined by 11%, therefore the ratio of median ET_a to P was 0.79, 0.93 and 0.89 for the pre-drought, drought and post-drought, respectively. The difference in ratios of median ET_a to P during the cool months was consistent with the annual results, showing that in the NMDB ET_a declines followed P declines, and in the SMDB, ET_a remained more stable while P declined. In the SMDB, this situation persisted in the post-drought period. In the warm months in either NMDB and SMDB ET_a changes followed P changes, and ratios of median ET_a to P remained similar in the pre-, drought and post-drought periods.

The downscaled GLEAM ET_a data are utilised in the rainfall-runoff modelling framework in Chapter 5 to assess model ET_a from an independent source.

5 Sensitivity of runoff to factors affecting non-stationarity

The quantification and prediction of runoff is crucial for water resources management. The sensitivity of runoff to climate inputs in the MDB is high, whereby proportional changes in mean annual runoff divided by the proportional changes in mean annual rainfall is generally higher than in similar climate regions in other parts of the world (Chiew et al., 2006; Tang and Lettenmaier, 2012).

Hydrological behaviours in the MDB catchments are shifting notably owing to the compounding effects of climate change and land use and land cover change in the region. The changed rainfall-runoff relationship (i.e., hydrological non-stationarity) imposes extra challenges for hydrological projections under future climate scenarios and for developing adaptative water resources management strategies. This component of the research aimed to (1) develop a model that can reflect explicitly the impacts of primary land use and land cover change within the catchments, particularly the effects of farm dams and vegetation dynamics; (2) assess the sensitivity of streamflow to the variability of the dominant hydroclimatic drivers; and (3) quantify the relative contributions of climate, farm dams and vegetation to changes in streamflow.

This research also uses daily streamflow data from 1982 to 2020 for 123 Hydrological Reference Stations (HRS) catchments in the MDB. This set of catchments is different from the 110 catchments in Chapter 3 as the only requirements for the modelling here are data completeness and presence of farm dams. Catchments with regulation and no farm dams were excluded herein. Climate data, including rainfall and potential evapotranspiration (PET), are derived from SILO (Jeffrey et al., 2001). Daily PET is estimated using Morton's wet environment areal evapotranspiration formulation (Chiew and McMahon, 1991; Morton, 1983). This method is widely used for its robust representation of PET under varying climate conditions. For hydrological modelling, gridded rainfall and PET data are spatially aggregated to catchment averages, enabling the application of lumped hydrological models. These datasets provide comprehensive spatial and temporal coverage, crucial for understanding hydrological processes and improving water resource management in the MDB.

5.1 Model accounting for impacts of farm dam and vegetation dynamics

The GR4J model (Perrin et al., 2003) is used as a benchmark hydrological model to investigate hydrological non-stationarity in the MDB catchments. The GR4J model has demonstrated its capability to simulate daily streamflow in various catchments globally, including in Australia (Coron et al., 2012; Zheng et al., 2024). The model requires daily rainfall and PET as inputs and has four parameters that need calibration: maximum production store (x1), water exchange coefficient (x2), maximum routing store (x3), and the time base of the unit hydrograph (x4). The original GR4J model does not explicitly account for hydrological processes related to land use and land cover changes, such as farm dam development and vegetation dynamics. However, these processes are implicitly reflected in the model partially through its parameters and calibration. For example, farm dam storage in a catchment may be implicitly related to both the maximum production store and the routing store, as well as water exchange rate and flow concentration time.

The GR4J rainfall-runoff model is progressively adapted to reflect the impacts of farm dams and vegetation dynamics on runoff, including (1) incorporating a farm dam module into the GR4J model, enabling explicitly accounting for the effects of farm dams on catchment runoff (Robertson et al., 2023); (2) modifying simulation of ET_a in the original GR4J by relating ET_a to the monthly dynamics of leaf area index (LAI), enabling explicitly account for the effects of vegetation change; and (3) integrating the above modifications to jointly simulate the hydrological effects of farm dams and vegetation dynamics and the interactions between climate, farm dam and vegetation dynamics on driving hydrological response in the catchments. Figure 20 shows a schematic of the adapted model. In the modelling, time-varying farm dam properties and leaf area index for each catchment are derived from remotely sensed observations (Peña-Arancibia et al., 2023b).

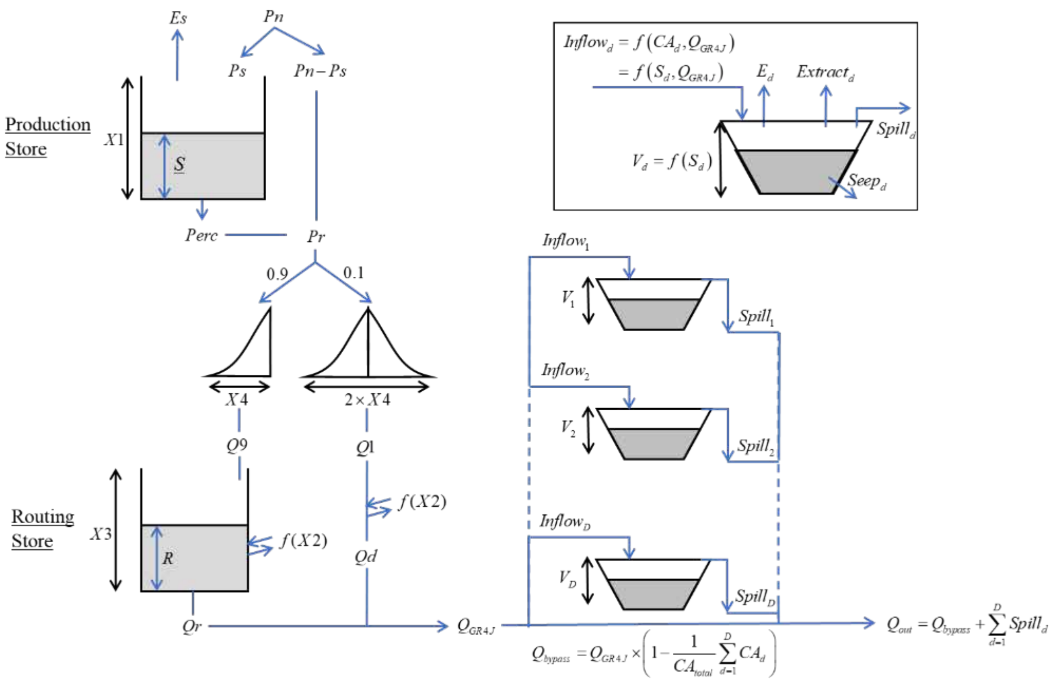

Figure 20. Diagram of hydrological model to explicitly reflect the hydrological impacts of farm dams and vegetation dynamics (based on Robertson et al., 2023).

Herein, to explicitly reflect the hydrological processes related to farm dams, we adapt the original GR4J model by introducing a farm dam module to describe water balance of the farm dam, expressed as:

$$\boldsymbol{S_t = S_{t-1} + I_t - D_t} \qquad \text{Equation 5}$$

where S_t is water stored in the farm dam at time t, I_t is inflow to farm dam and D_t is water demand/water losses from the farm dam. Water demand/losses are assumed to be a constant proportion (α) of long-term mean water availability (i.e., long-term mean daily runoff), which needs to be calibrated. Since there could be hundreds of farm dams with various sizes in a catchment, it is computationally intensive to calculate water balance of each single farm dam. For simplification, in this study, we classify farm dams within a catchment into 11 groups, each having a representative volume-surface area-catchment area relationship. More details on the modelling method can be found in Robertson et al. (2023).

Vegetation dynamics can influence catchment evapotranspiration. While vegetation transpiration may increase due to greening, it could decrease due to improved plant water use efficiency. To address hydrological processes related to vegetation dynamics, we primarily link evapotranspiration with the temporal variation in leaf area index (LAI) as observed through remote sensing. Therefore, the evapotranspiration function in the original GR4J model is replaced by the model proposed by Kondo (1998), expressed as:

$$\frac{ET_a}{ET_0} = a + b[1 - \exp(-k \cdot LAI)] \qquad \text{Equation 6}$$

where ET_a and ET_0 are actual evapotranspiration and potential evapotranspiration respectively, LAI is the leaf area index input to the model, a, b and k are parameters that need to be calibrated. Note that this formulation the model is only simulating higher ET_a with higher LAI and not the potential ET_a decrease due to improved plant water use efficiency.

Four modelling experiments are implemented in this study to investigate hydrological non-stationarity in the catchments. The modelling experiments are respectively based on the original GR4J model (M1) and the three modified models: GR4J plus farm dam module (M2); GR4J plus LAI module (M3); and GR4J plus both farm dam and LAI modules (M4). M1 serves as a benchmark modelling, M2 and M3 are used to explore the individual effects of farm dam (FD) and vegetation dynamics (VD), while M4 explores the compounding effects of FD and VD.

For all modelling experiments, parameters in the hydrologic models are calibrated by minimising the NSE-Bias objective function expressed as (Viney et al., 2009):

$$\mathrm{NSE_{bias}} = \mathrm{NSE} - 5|\log(1 + \mathrm{Bias})|^{2.5} \qquad \text{Equation 7}$$

$$NSE = 1 - \frac{\sum_{i=1}^{n}\left(Q_{mod,i} - Q_{obs,i}\right)^2}{\sum_{i=1}^{n}\left(Q_{obs,i} - \bar{Q}_{obs}\right)^2} \qquad \text{Equation 8}$$

$$Bias = \frac{\sum_{i=1}^{n} Q_{mod,i}}{\sum_{i=1}^{n} Q_{obs,i}} - 1 \qquad \text{Equation 9}$$

where, NSE is the widely used Nash-Sutcliffe model efficiency coefficient (Nash and Sutcliffe, 1970), Bias is the ratio error in the total runoff simulation, Q_{mod} is modelled daily runoff, Q_{obs} is observed daily runoff, $\overline{Q}_{obs}$ is mean observed daily runoff, and *n* is the total number of days in the modelling period. The NSE and Bias are used to evaluate overall model performance of the four models over the entire modelling period. In addition, for model performance with respect to hydrological non-stationarity, the variation of annual Bias represented by coefficient of variation (CV) of the annual Bias series is estimated. It is assumed that a model with better consideration of hydrological non-stationarity can lead to more robust model performance under different hydroclimate conditions hence with lower CV in the annual Bias timeseries.

The calibration results show that the performance of the four models is generally comparable amongst them. The models with additional consideration of the hydrological impacts from farm dams and vegetation dynamics outperform the original model in terms of overall model performance metrics such as NSE and bias (Figure 21).

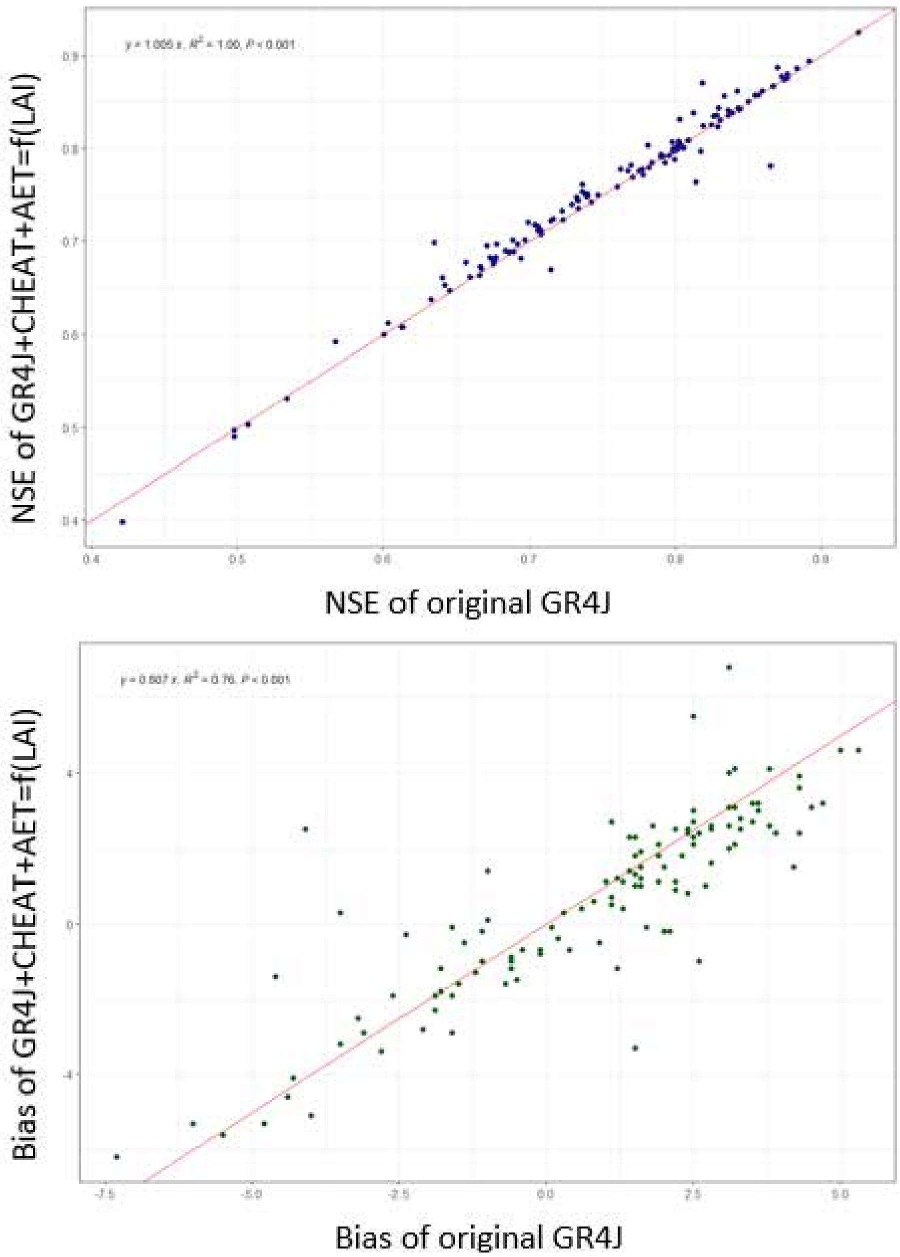

Figure 21. Performance of the adapted model (GR4J considering effects of farm dam and LAI dynamics) compared against that of the original GR4J. Top: NSE, bottom: bias.

Figure 22 further summarizes the model performances for catchments in the NMDB and SMDB separately. The results show that the models incorporating farm dams and vegetation dynamics (M2, M3, M4) outperform the original GR4J both for the northern and southern catchments. The improvements are more evident in NMDB than in SMDB in terms of higher NSE and lower bias. The inclusion of farm dam (M2) and vegetation dynamics (M3) both lead to improved model performance, with M2 performing better than M3. Modelling with both farm dams and vegetation dynamics included (M4) does not produce better results with modelling with each of the driver (M2 or M3) represented alone. This suggests complex interactions between the hydrological processes related to farm dams and vegetation dynamics.

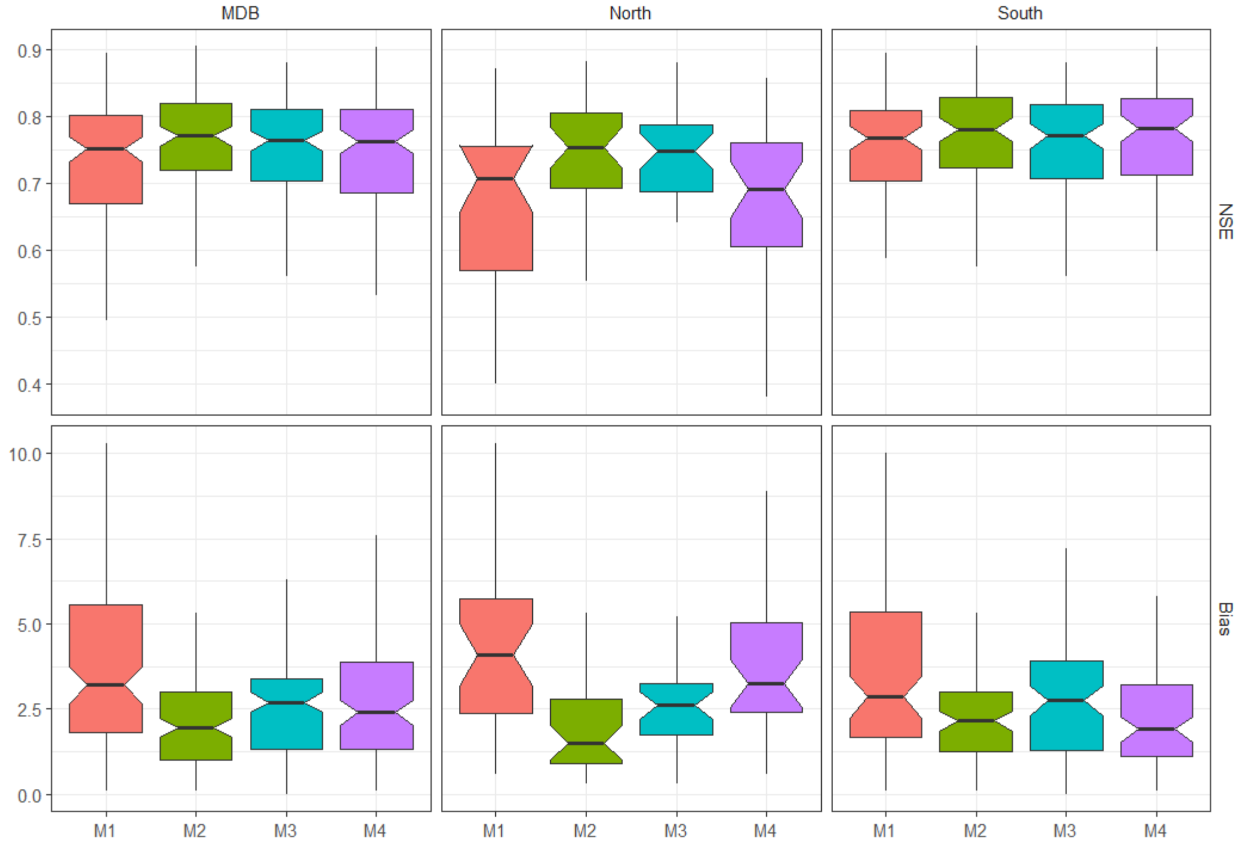

Figure 22. Performance of the adapted model (GR4J considering effects of farm dams and LAI dynamics) compared against that of the original GR4J for different regions. Bias in the plot is the absolute value taken as |Bias|. The notch displays the confidence interval around the median which is normally based on the median +/- 1.57 x IQR/sqrt of n of the sample. M1 represents original GR4J, M2 is GR4J considering farm dams impact, M3 is GR4J considering vegetation dynamics, M4 is GR4J considering both impacts of farm dams and vegetation dynamics.

The example in Figure 23, for catchment A4260533 (-35.21°S, 139.00°E, 466 km²), shows that although the original GR4J model (M1) performed reasonably over the full period (NSE=0.75 and Bias=3%), there can be considerable differences in model performance for different periods. The model significantly underestimates streamflow by almost 20% during the pre-drought period (prior to 1997), and overestimates streamflow by almost 50% during the drought period (1997–2009). In the post-drought period (2010–2020), although the overestimation is reduced to about 10%, the model performance still differs from that of the pre-drought period, indicating a change or incomplete recovery in catchment hydrological behaviour. The results indicate considerable uncertainty in hydrological modelling induced by hydrological non-stationarity. The performance of the models considering the hydrological processes related to farm dams (M2) and vegetation dynamics (M3) and both of FD and VD (M4) of the example catchment indicates that incorporating farm dams and vegetation dynamics can overcome some of the above problems, with relatively lower variation in biases during dry, wet and average years. In particular, M2 performs best for the drought period while M4 performs well in the post-drought period. The results suggest that the importance of accounting for the substantial hydrological impact of farm dams during dry periods, and vegetation dynamics generally particularly in the post-drought period.

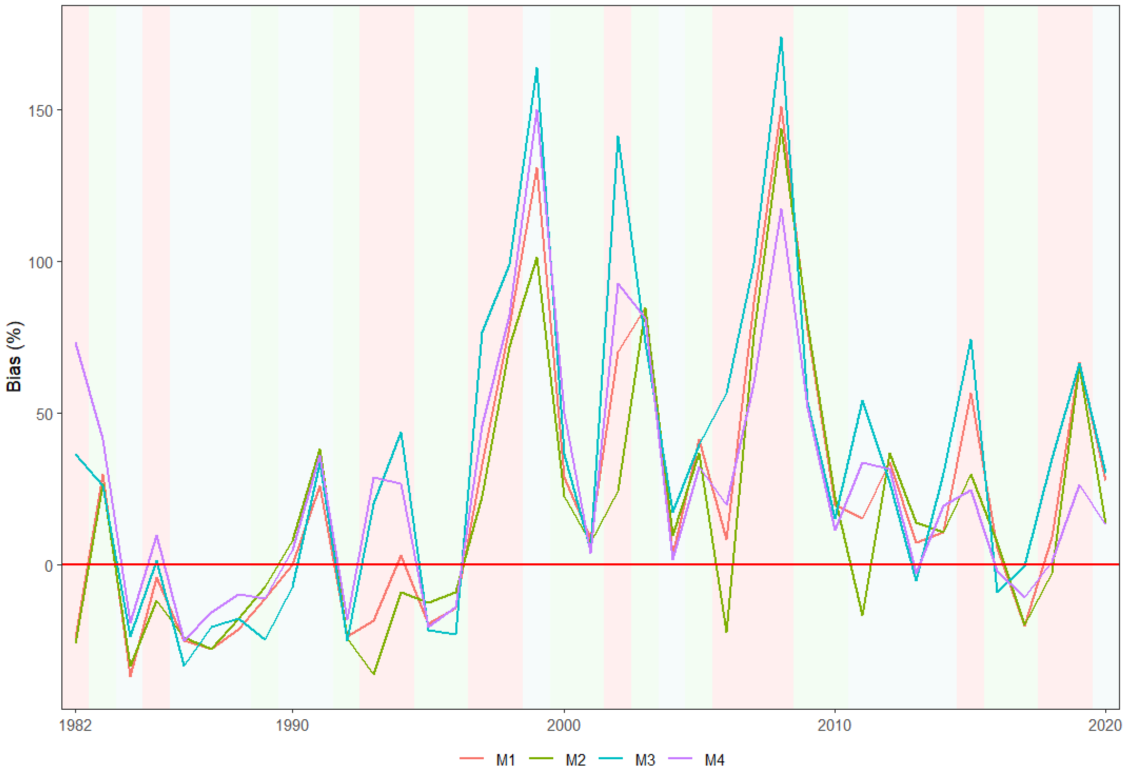

Figure 23. Varying model performance under different climate conditions for an example catchment (A4260533). The background in pink, blue and green represents dry, wet and normal years respectively according to annual rainfall. M1 represents original GR4J, M2 is GR4J considering farm dams impact, M3 is GR4J considering vegetation dynamics, M4 is GR4J considering both impacts of farm dams and vegetation dynamics.

5.2 Sensitivity of streamflow to dominant hydroclimate drivers

The sensitivity of streamflow to dominant hydroclimate drivers can be quantified using the above developed models. In general, the model-based sensitivity analysis can be done by generating various combinations of climate, farm dams and vegetation conditions as inputs to the hydrological model. The sensitivity of streamflow to the dominant climate variables, vegetation, and farm dams are then quantified by investigating the differences in the simulated streamflow from the different input combinations. The method is effective in quantifying the sensitivity of streamflow metrics of interest to the dominant drivers, but it is difficult to generate the range of realistic input combinations. Here, we use an alternative approach to quantify the sensitivity of annual runoff the dominant hydroclimate drivers by regressing the simulated annual runoff from M4 (i.e., GR4J incorporating both farm dams and vegetation dynamics modules) against annual rainfall, potential evapotranspiration, LAI and farm dams' volume. The regression approach is found efficient and effective, where R^2 for the regression model is above 0.85 for most of the catchments. Based on the model, the elasticity of streamflow with respect to the drivers is then defined as:

$$\boldsymbol{\varepsilon_y} = \frac{\partial y/y}{\partial Q/Q} \approx \frac{\Delta y/\bar{y}}{\Delta Q/\bar{Q}} \quad \text{Equation 10}$$

where, Q is annual runoff, y is the dominant hydroclimate variables considered, i.e., rainfall (P), potential evapotranspiration (PET), vegetation (LAI) and farm dams (FD). The elasticity coefficient (ε_x) is a unitless metric representing the ratio of percentage change in the dominant variable to the percentage in the response variable (i.e., annual runoff herein).

Figure 24 and Figure 25 show the probability and spatial distributions of streamflow elasticity estimated from the simulation based on M4 for the studied catchments. It is found that streamflow elasticity to rainfall is around 2.7 (median) but ranges from 1.3 to 4.4 for most of the studied catchments, indicating that a 10% change in annual rainfall leads to a 13% to 44% change in annual runoff. The median elasticity of annual runoff for catchments in MDB to PET, LAI and FD is around -0.8, -0.5, and -0.16 respectively, indicating 10% increase in PET, LAI and FD will result in 8%, 5% and 1.6% decrease respectively in annual runoff.

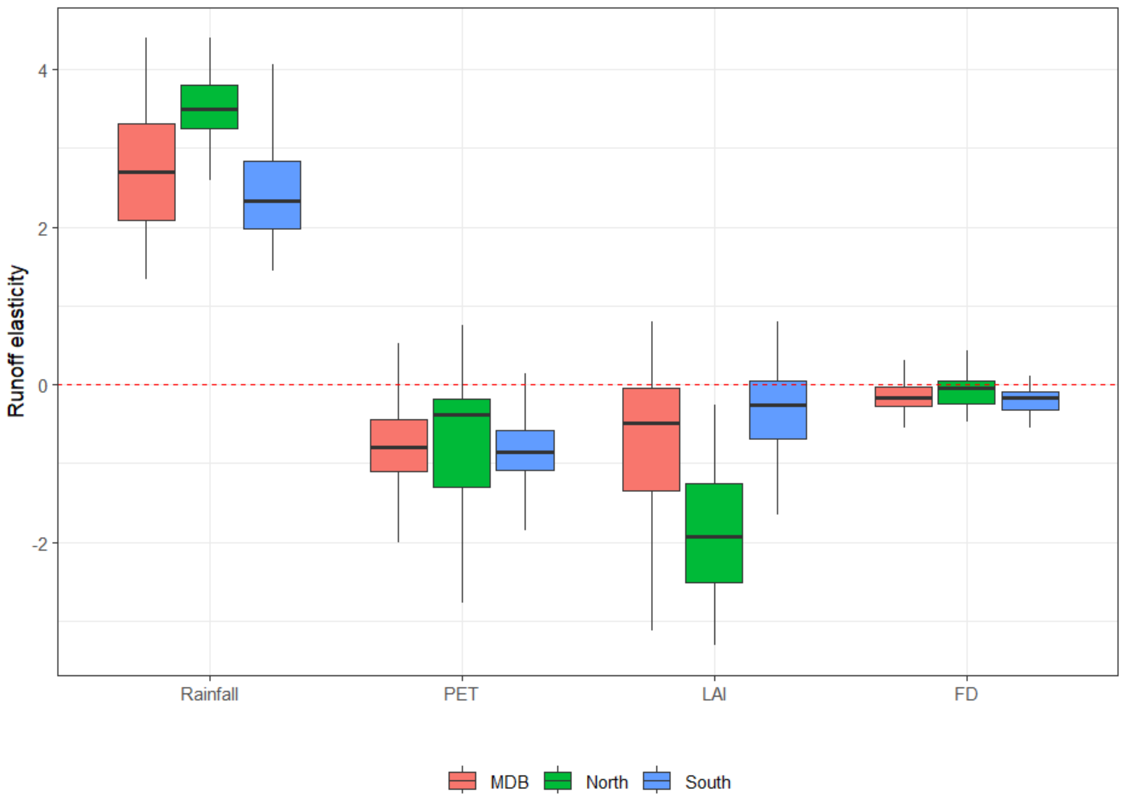

Figure 24. Streamflow elasticity to rainfall, potential evapotranspiration (PET), leaf area index (LAI) and volumes of farm dams (FD) for catchments across MDB, northern MDB and southern MDB.

The sensitivity of streamflow to the dominant hydroclimate drivers varies considerably across the MDB. The median elasticity coefficient of rainfall, PET, LAI and FD in the NMDB catchments are 3.5, -0.4, -1.5, and -0.04 respectively, while that for the SMDB catchments are 2.3, -0.9, -0.25, and -0.17 respectively. Catchments in the NMDB are found to be more sensitive to rainfall and vegetation dynamics than those in the SMDB, while the effects of PET and farm dams on streamflow are more evident in the SMDB than those in the NMDB. It is worth noting that uncertainty may exist in the estimated elasticity owing to uncertainties in the model and the farm dams and LAI datasets.

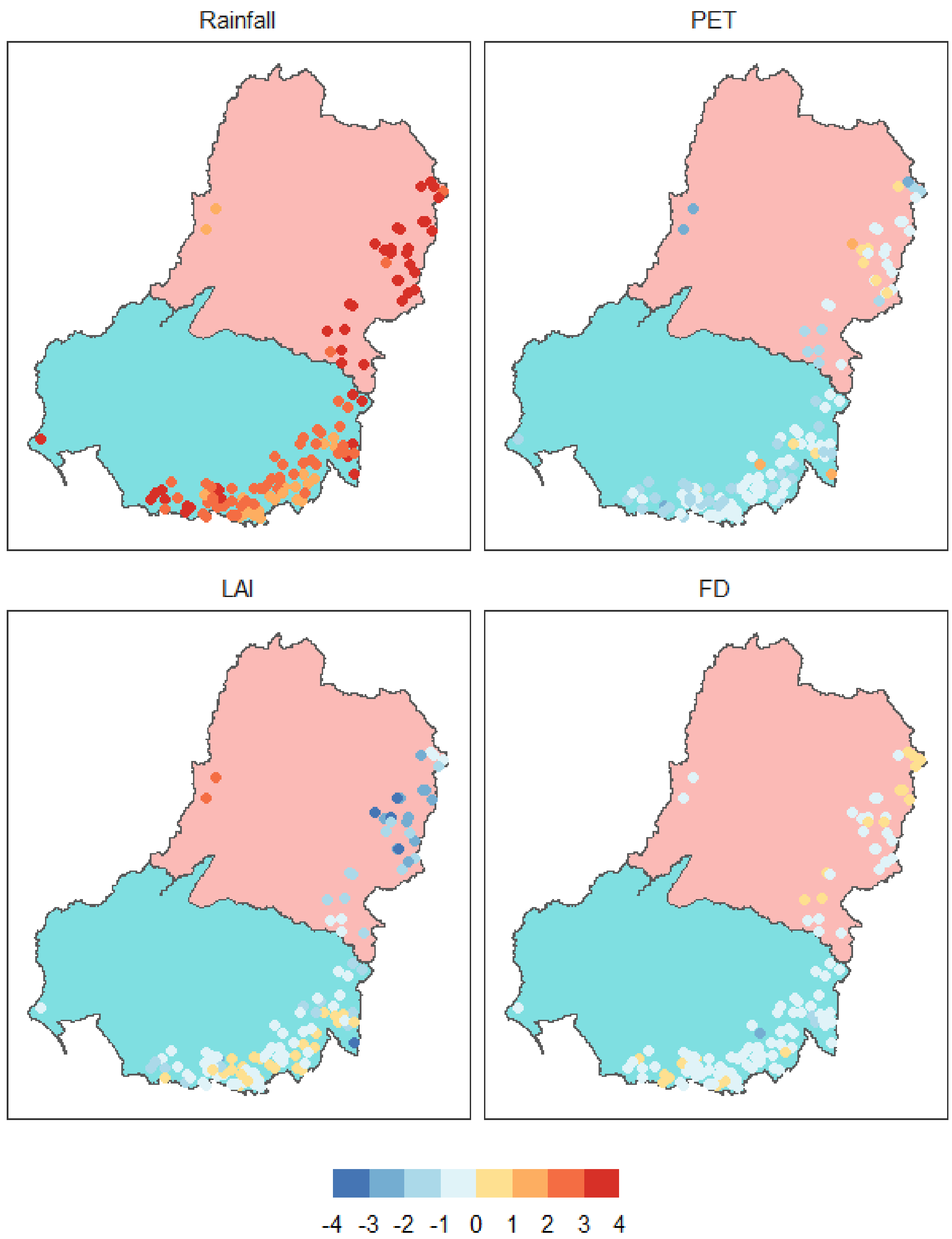

Figure 25. Spatial distribution of streamflow elasticity to rainfall, potential evapotranspiration (PET), leaf area index (LAI) and volumes of farm dams (FD) across MDB.

5.3 Attribution of streamflow changes

The elasticity coefficients derived above are used to quantify the contributions of the dominant hydroclimate variables (i.e., rainfall, PET, LAI and farm dams) to changes in annual runoff in the drought period (1997–2009) and post-drought period (2010–2020) as compared against the pre-drought period (1982–1996). It is worth noting that variables with higher elasticity do not necessarily mean a higher contribution to the changes in runoff as the contribution of the variable also depends on its change ratio. Mathematically, the contribution is the product of elasticity coefficient and the change ratio, expressed as:

$$\frac{\Delta Q}{\bar{Q}} = \varepsilon_P \frac{\Delta P}{\bar{P}} + \varepsilon_{PET} \frac{\Delta PET}{\overline{PET}} + \varepsilon_{LAI} \frac{\Delta LAI}{LAI} + \varepsilon_{FD} \frac{\Delta FD}{FD} + \delta \qquad \text{Equation 11}$$

Where $\varepsilon_P, \varepsilon_{PET}, \varepsilon_{LAI}\ and\ \varepsilon_{FD}$ are the elasticity coefficients with respect to annual rainfall, annual PET, annual mean LAI and farm dams volumes. δ is the systematic estimation error.

Figure 26 shows the estimated contributions of the four drivers to changes in runoff for all the studied catchments in the MDB. For runoff changes in the drought period (Figure 26 left) as compared to that in the pre-drought period, it is found that median contributions from rainfall, PET, LAI and farm dams are around -41%, -1.8%, 0.4% and -14.7% respectively. Reduction in rainfall and growth in farm dams during the drought period are the most important drivers leading to lower runoff in the period. For the post-drought period (Figure 26 right) as compared to the pre-drought period, corresponding median contributions of the four drivers considered are -14.8%, 0.005%, -0.6% and -23.1% respectively. Rainfall and farm dams are still the two most critical drivers for the lower runoff, but the impacts of growth in farm dams are stronger than rainfall in some catchments. During the post-drought period, the impacts of PET are negligible. The contributions of LAI can be positive or negative, depending on the increase or decrease of LAI in the catchments.

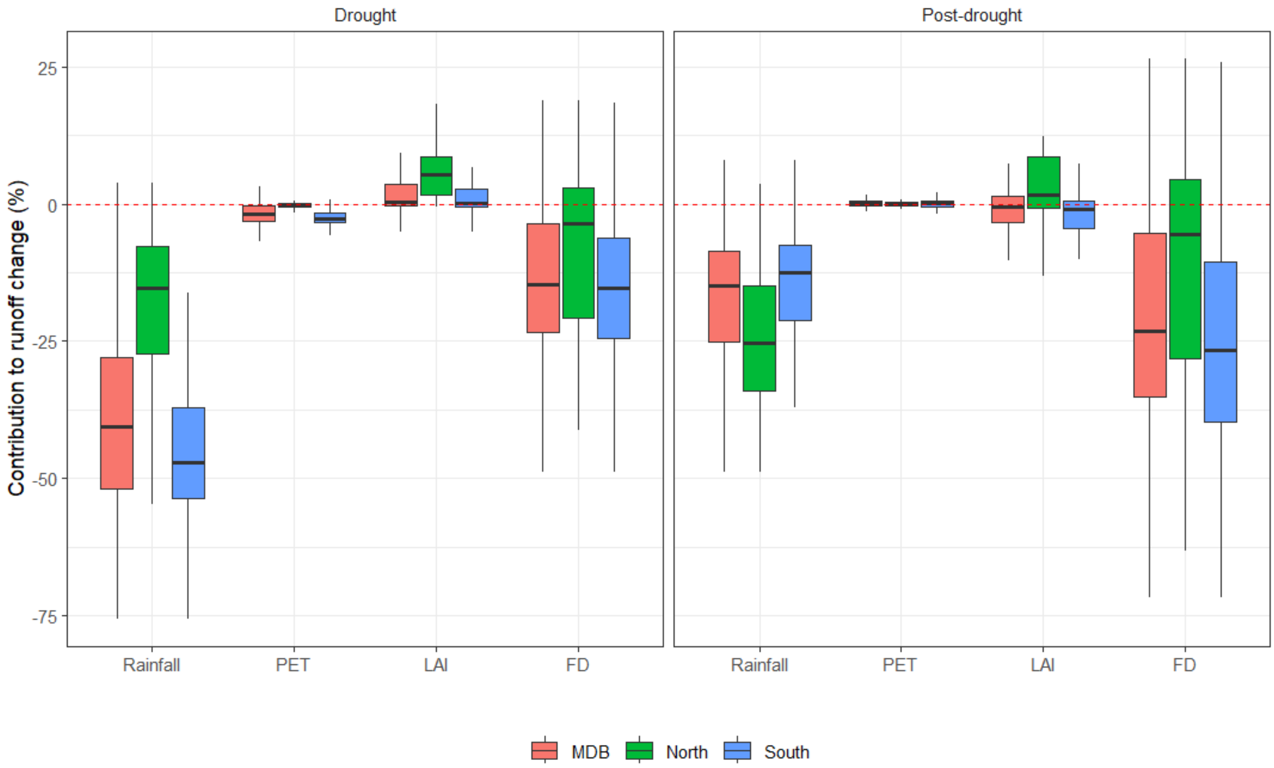

Figure 26. Contributions of changes in rainfall, potential evapotranspiration (PET), leaf area index (LAI) and volumes of farm dams (FD) to catchment runoff across MDB.

Contributions of the hydroclimate variables to changes in runoff vary substantially across the studied catchments (Figure 26 and Figure 27). Particularly, for the drought period, contributions of rainfall are much higher in the SMDB catchments (median value of -47%) than in the NDMB catchments (median value of -15%). For the drought period, median contributions from growth in farm dams to lower runoff are also higher in SMDB catchments (-15.4%) than in the NMDB catchments (-3.5%). In the post-drought period, however, median contributions from rainfall are higher in the NMDB catchments than in the southern catchments, while contributions from growth in farm dams are higher in the SMDB catchments.

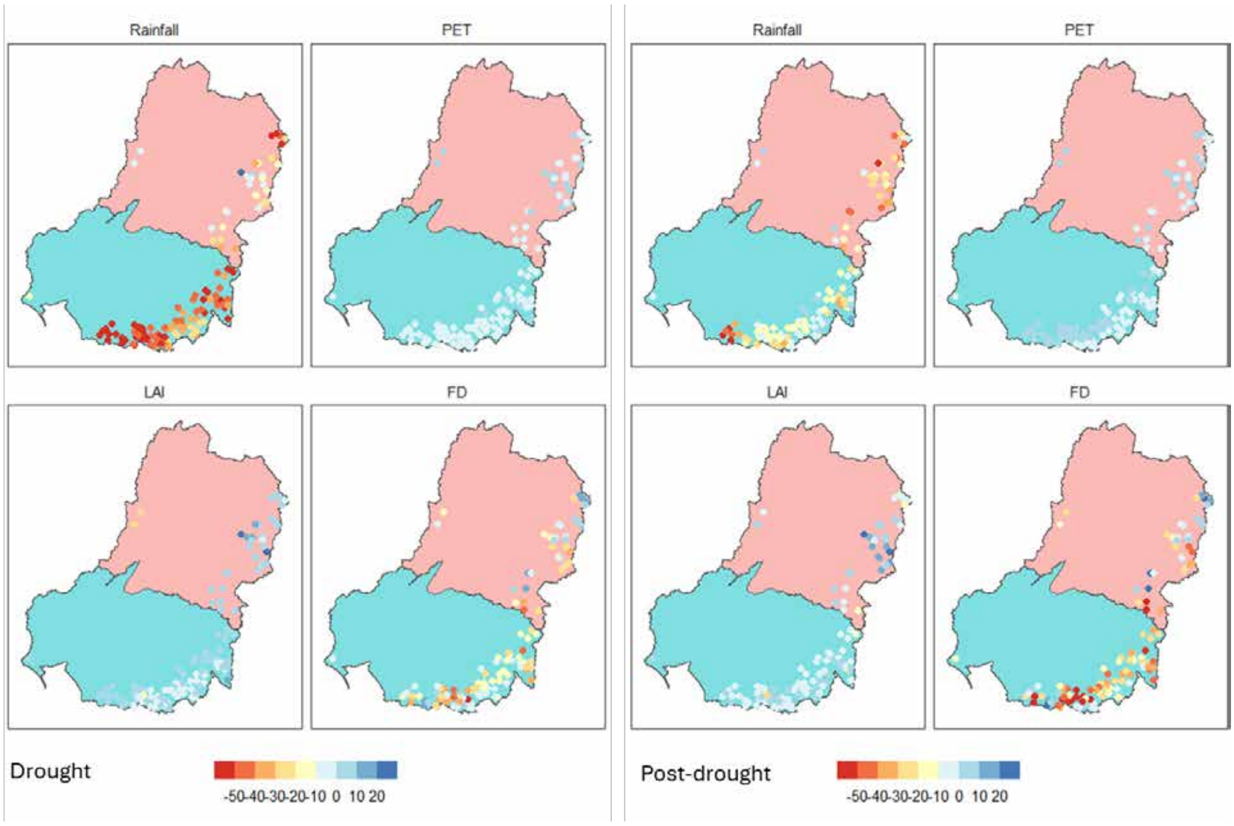

Figure 27. Spatial patterns of contributions of changes in rainfall, potential evapotranspiration (PET), leaf area index (LAI) and volumes of farm dams (FD) to catchment runoff across MDB.

6 Quantifying irrigation areas and water use

The MDB is considered the ‘food bowl’ of the nation, sustaining 40% of Australian farms and producing over a third of Australia’s gross agricultural value (AU$22,0 billion out of AU$58,9 billion, ABS, 2019). In 2020/21 (last year with published statistics), the MDB accounted for 60% of all irrigated land in Australia (1.2 million ha) and used 4,900 GL, or 62% of Australia’s freshwater use (ABS, 2023). The area equipped for irrigation (or irrigable areas, i.e., areas that have infrastructure to irrigate crops) in the northern MDB is ~10,000 km^2 (ABARES, 2021), and most irrigation is for cotton production (Figure 28). In a higher than average rainfall year like 2017/2018 (BoM, 2022), ~1,835 MCM of water were used to grow ~110,000 tonnes of cotton in the NMDB, or ~96% of Australia’s production (ABS, 2019; Goesch et al., 2020). Due to the high rainfall and streamflow variability, water availability dictates the extent of irrigated crops that can be sustained in any given year. The water use in 2017/2018 contrasts to the ~268 MCM estimated for irrigation of cotton in 2007/2008, during the Millenium Drought (Goesch et al., 2020). As mentioned before, Chiew et al. (2022a) identified that in the last 30 years water infrastructure and water extraction for irrigation and other productive activities caused roughly half of the reduction in streamflow in the Barwon-Darling River.

Understanding the potential impact of irrigated agriculture on streamflow in a largely unregulated river system with high streamflow variability such as the NMDB is key for an adequate management of water resources. This is particularly important when the available water is shared between the environment and other productive users (i.e., irrigation, town water supply). Assessing the spatiotemporal variation in irrigation water use within the MDB is conducted by computing estimates of summer crop irrigated areas and their water use using reflectance (i.e., capturing imagery in the visible and infrared spectrum) remote sensing. The focus is on summer irrigated crops because they comprise >90% of irrigation in the NMDB. This is performed at spatial resolutions (i.e., ≤100 m) and frequencies (i.e., ≤monthly) useful for analyses at the paddock scale (i.e., ≤1000 m^2). However, due to paucity of data and the effects of clouds, no remote sensing data combines these two characteristics to assess trends in long-term water use. In this research low spatial-resolution-high-frequency satellite imagery and high spatial-resolution-low-frequency imagery were ‘blended’ to produce a continuous, gap-free, 16-daily and 30 m resolution imagery across the main irrigated areas of the MDB. This imagery was then used to extract land cover patterns from remote sensing indices via AI/ML that were associated with summer irrigation. Using the extracted patterns, a neural network was trained to find these patterns and classify the landscape, focusing on summer irrigated crops. Results were then validated against secondary data such as crop survey statistics and estimated crop water use. The remainder of this chapter describes the data, methodology and results of the AI/ML mapping.

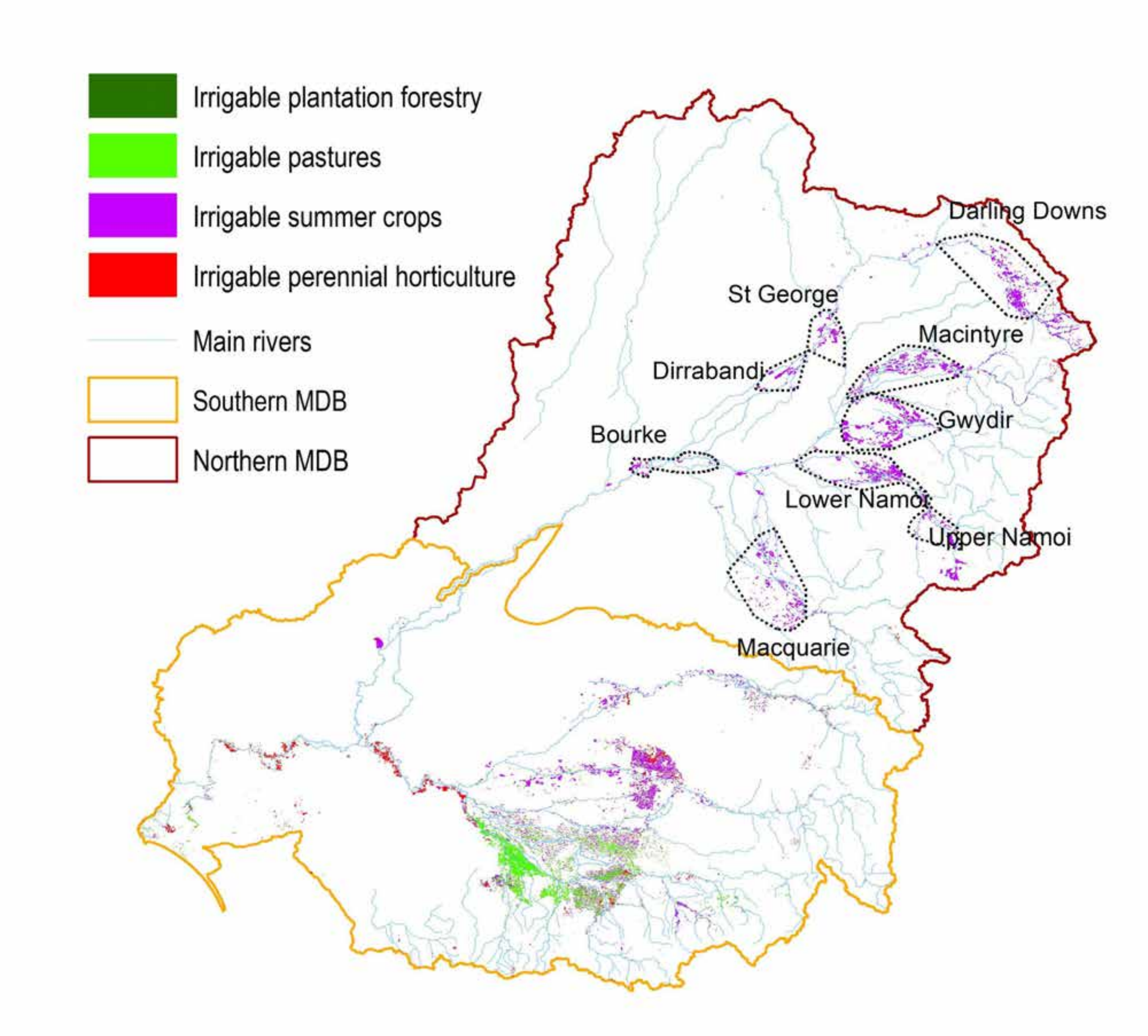

Figure 28. Irrigable land use (ABARES, 2021) in the Murray-Darling Basin (NMDB in maroon outline, SMDB in orange outline). Main cotton irrigation districts in the NMDB outlined with black-dashed lines (The Australian Cottongrower, 2020).

6.1 Pre-processing

Combining low spatial resolution-high temporal frequency images (having lower detail but taken frequently over time) with high spatial resolution-low temporal frequency images (providing higher detail but taken less frequently) has become a widely used technique to blend satellite imagery that is both detailed and frequent without any gaps. The Sub-pixel class fraction change information Flexible Spatiotemporal DAta Fusion (SFSDAF) method (Li et al., 2020) was used in this research to blend 16-day remote sensing composites from Landsat (TM, ETM+ and OLI sensors from the Landsat-5, 7 and 8 satellites) at 30 m resolution with 16-day (but taken daily) gap-free remote sensing composites from MODIS (product MCD43A4 V6.1). The SFSDAF algorithm was used due to its practicality (only requires one pair of coarse resolution (CR)-fine resolution (FR) images before prediction and one CR image at prediction to produce a FR image at prediction) and ability of detecting gradual (i.e., phenological) or abrupt (e.g., floods) land cover changes. This enabled the assessment to be conducted from 2000 (when the MCD43A4 data became available) to 2020.

The MDB was subdivided into tiles, with the focus on areas with irrigated agriculture (Figure 29). Following Peña-Arancibia et al. (2021), two remote sensing indices, the Enhanced Vegetation Index (EVI, Huete et al., 2002) which provides a proxy for vegetation health, and the Global Vegetation Moisture Index (GVMI, Ceccato et al., 2002a; Ceccato et al., 2002b) which provides a proxy of vegetation moisture, were blended using Landsat and MCD43A4 reflectance data.

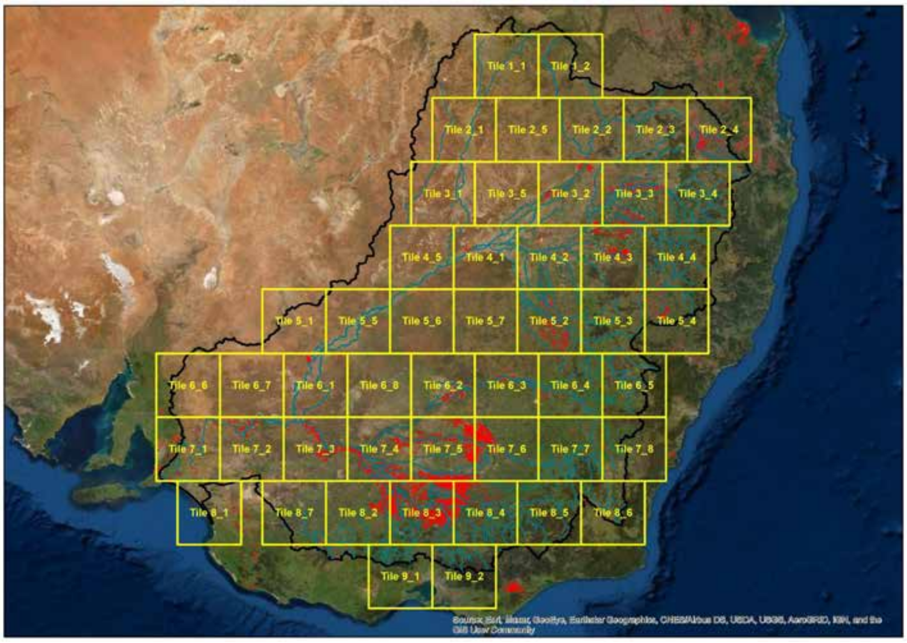

Figure 29. Tiles used to blend high-resolution-low-frequency Landsat Enhanced Vegetation Index (EVI) and Global Vegetation Moisture Index (GVMI) with low-resolution-high-frequency MODIS MCD43A4 EVI and GVMI. Irrigated areas are shown in red (ABARES, 2021).

The resulting gap-free blended data are at 16-day frequency and 30 m resolution, and from February 2000 to July 2020. The EVI and GVMI are correlated in vegetative land covers and decouple in surface water. Because EVI and GVMI are complementary, they can be used to separate land surface from water, thus, a joint timeseries of EVI followed by GVMI is chosen to analyse temporal patterns for different land covers using ML/AI methods. In addition, the Normalised Vegetation Index (NDVI), a widely used vegetation index, was also blended simultaneously. When predicting a FR, the final image retained the observed pixels and only the gaps were replaced with predicted pixels. The correlation coefficient (R^2) of the predicted FR pixels versus the observed FR pixels were used as goodness-of-fit metrics. Blending results for two tiles (tile 3_3 in an irrigated area in the NMDB and tile 8_3 in an irrigated area in the SMBD, see Figure 29) are shown in Figure 30. Monthly R^2 are generally >0.7 for NDVI and EVI and generally >0.5 for GVMI, noting that GVMI can have values closer to 0 in arid areas than NDVI or EVI, thus reducing variability in the data and hence accuracy. Results are better for tile 3_3 than for tile 8_3, arguably because of the data completeness due to prevailing cloud cover in the SMDB. All remote sensing indices show a scatter close to the 1:1 line when modelled (i.e., blended) values are compared to observed values (i.e., true observations retained in the final image but used to evaluate the blending accuracy).

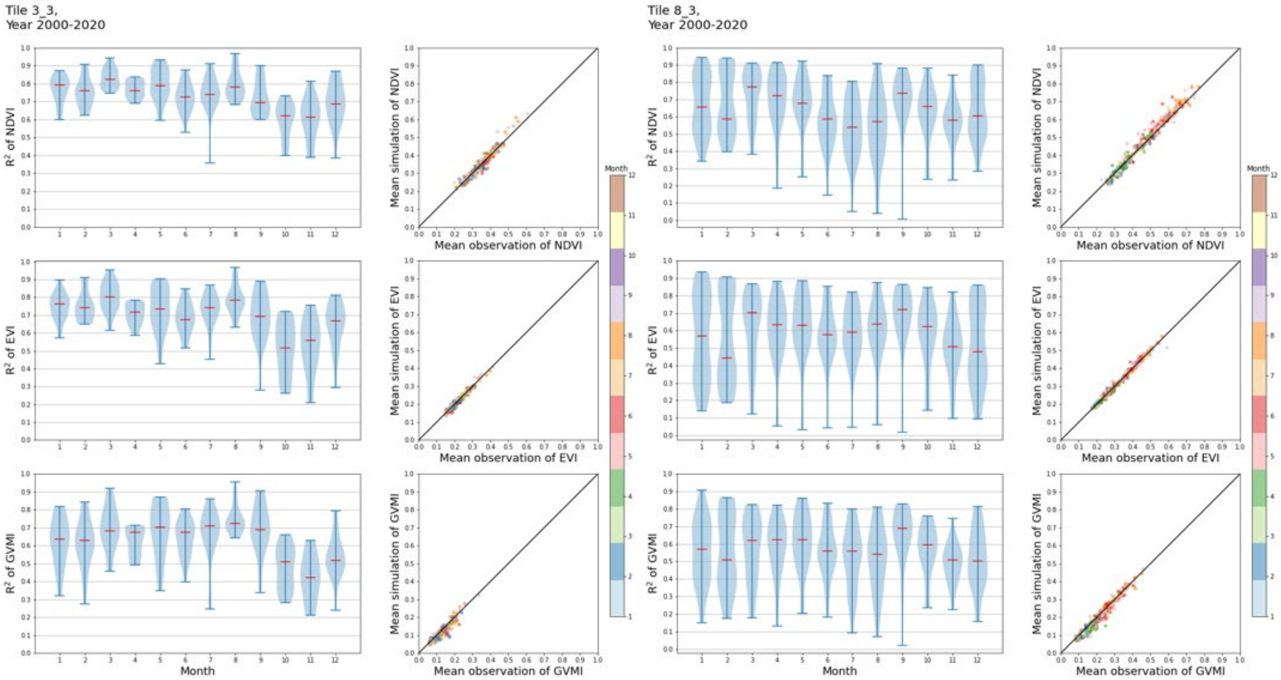

Figure 30. Blending accuracy summary for NDVI, EVI and GVMI for Tile 3_3 (irrigated area in the NMDB) and Tile 8_3 (irrigated area in the SMDB). The left panel shows correlation coefficient (R^2) violin plots for both indices in each month for all analysis years combined. The right panel shows a scatterplot between the mean and predicted EVI and GVMI values.

The performance for all tiles from 2000 to 2020 is shown in Figure 31, highlighting the overall high accuracy of the blending performance for the remote sensing indices used here.

A joint timeseries of EVI followed by GVMI is chosen to analyse temporal patterns for different land covers. In pre-processing, the joint timeseries is smoothed using a Savitzky-Golay filter (third order polynomial fitted to five neighbouring data points), a method proven to be effective in maintaining the high-frequency signal components found within vegetation indices timeseries (Cao et al., 2018; Savitzky and Golay, 1964).

Year 2000-2020

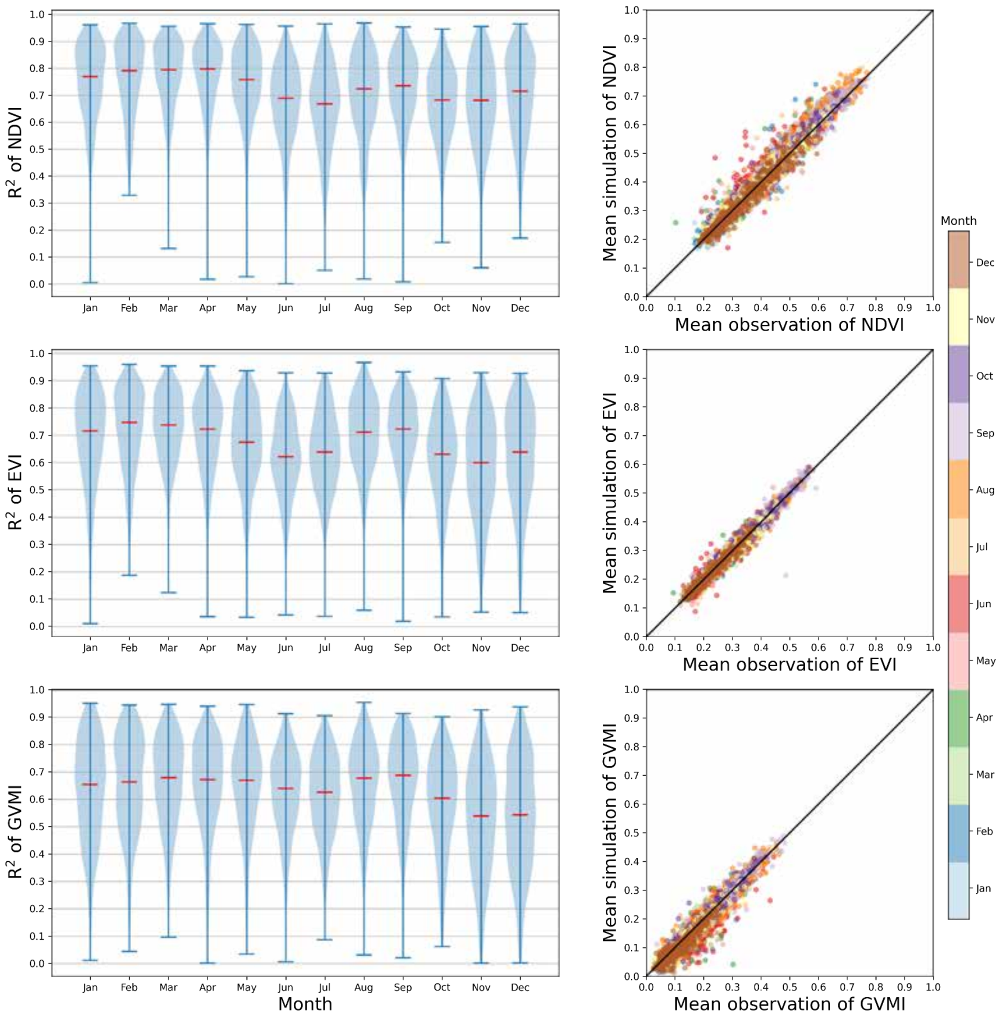

Figure 31. Blending accuracy summary for NDVI, EVI and GVMI for all tiles in the MDB. The left panel shows correlation coefficient (R^2) violin plots for both indices in each month for all analysis years combined. The right panel shows a scatterplot between the mean and predicted EVI and GVMI values.

6.2 Clustering using Self-Organising Maps

Thirdly, smoothed timeseries of EVI and GVMI are clustered simultaneously using Self-Organising Maps (SOM, Kohonen, 1998), initially into 16 clusters. The Euclidean distance is used as the objective to match the timeseries and each timestep in the timeseries. The number of clusters relies on practical heuristic rules, striking a balance between the time needed for algorithm convergence (more clusters equating to longer running times) and the anticipated variety of land cover types.

The SOM clustering was implemented for the years 2000-2001, 2005-2006, 2007-2008, 2010-2011 and 2017-2018, from October to May (coinciding with the summer cropping months, 17 timesteps for EVI and 17 timesteps for GVMI, totalling 34 timesteps) in all main irrigated areas in the MDB (Figure 32). These years were chosen based on water allocation history representing dry, average and wet conditions in both NMDB and SMDB (Goesch et al., 2020) and availability of validation data.

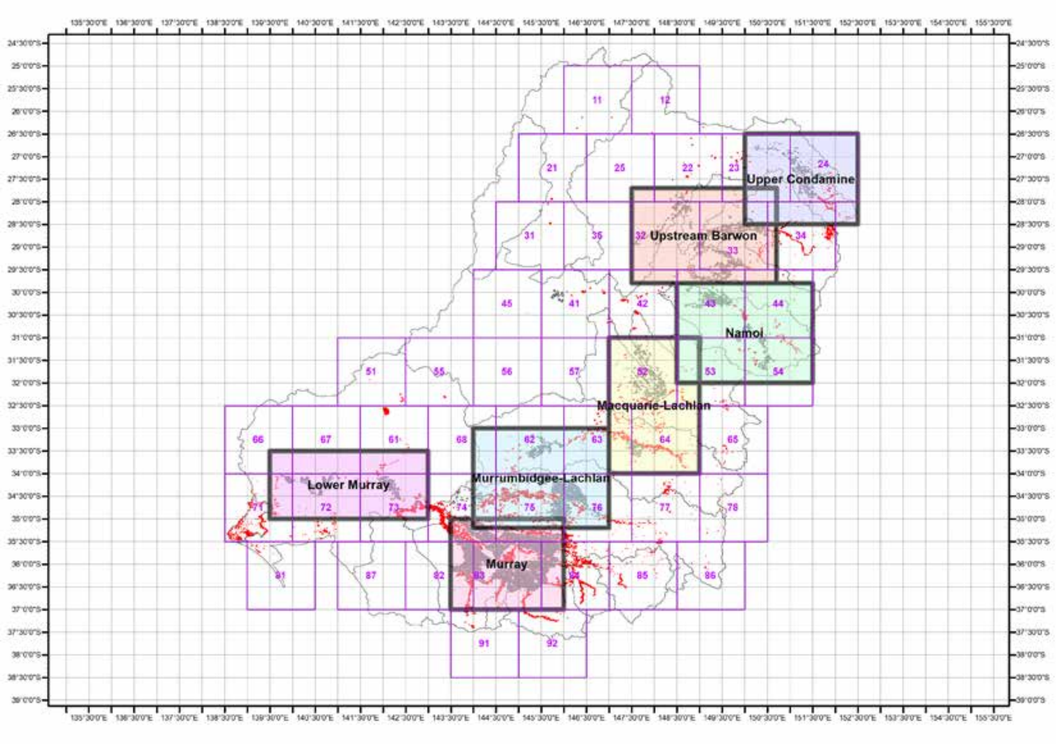

Figure 32. Irrigated areas used in the Self-Organising Map (SOM) clustering.

Figure 33 shows an example of the SOM clustered 16-day sequence of EVI values followed by the 16-day sequence of GVMI for the summer cropping months in 2017-2018. These sequences can be related to vegetation (or other land cover) phenology, i.e., the stages in crop development from sowing to harvesting as suggested by crop calendars (ABARES, 2012) in the Murrumbidgee-Lachlan irrigation area. Each clustered satellite pixel timeseries is plotted, and a ‘density’ plot is created by overlaying all timeseries, displaying low density yellow hues to high density dark blue hues. This information was used to assign different land covers according to phenology patterns. For irrigated crops, the patterns suggest a sowing period starting in October with a growth period of 3 months and harvesting starting in May. The EVI and GVMI assigned to irrigated crops showcased these characteristics, with a long growth period. Trees/orchards showed small EVI and GVMI variations with relatively high (>0.3) EVI and GVMI values, as is expected from the mostly evergreen trees/orchards in the area. Sparsely vegetated land covers exhibited both very low (<0.15) EVI and GVMI, whereas permanent water exhibited low EVI and high (>0.4) GVMI.

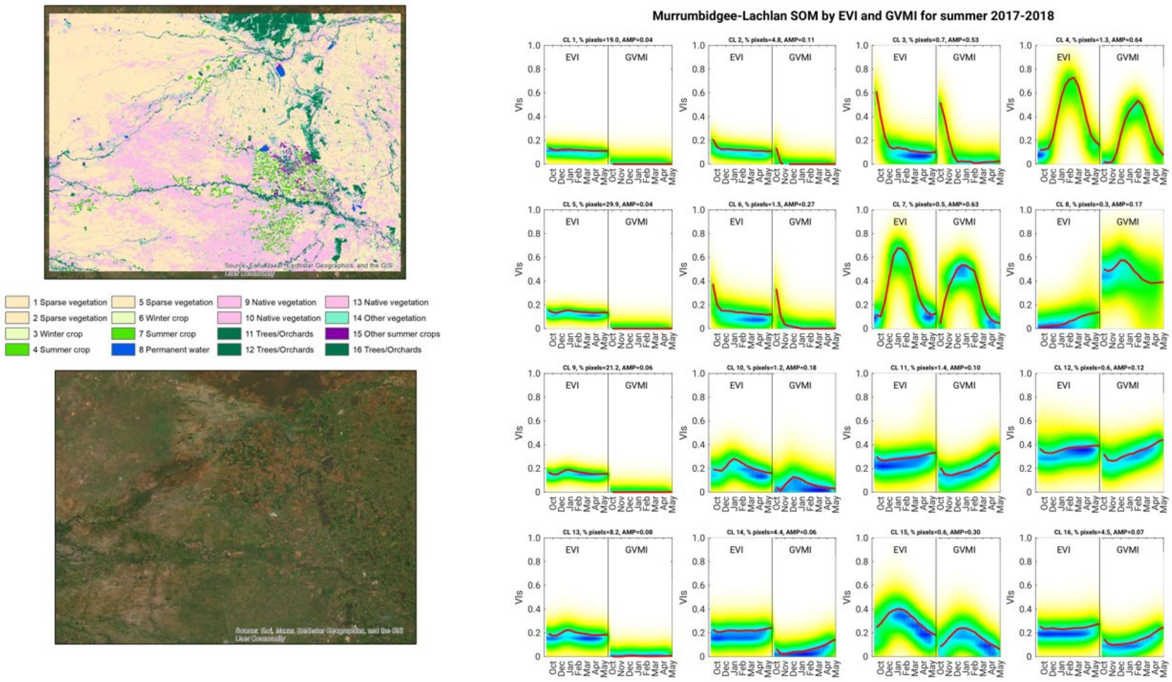

Figure 33. Example maps for the Murrumbidgee-Lachlan irrigation area of the SOM results and 16-day EVI and GVMI clustered density timeseries patterns for warm months in 2017-2018, year with higher than average rainfall over the MDB. The map shows how the land cover assignment was performed by analysing the SOM EVI and GVMI clustered timeseries patterns. The 16-day timeseries show the timeseries density (from low density expressed as yellow to high density expressed as dark blue hues) for different land cover patterns assessed in this study. The red line corresponds to the median of all timeseries.

The SOM clustering is performed for all years and all irrigated areas, which based on the EVI and GVMI phenology, renders the following manually assigned land covers: crops, trees, other vegetation, sparse vegetation/bare, water intermittent and water permanent. Subsequently, all the resulting clusters considered summer irrigated crops by their phenology, are grouped and SOM is used again to further refine their clustering. This further step is required to separate irrigated crops and vigorous native pastures, riparian vegetation or dryland crops in areas in which rainfall is in sync with the greenness signal from EVI and GVMI timeseries and irrigation may be of a supplementary nature (Peña-Arancibia et al., 2014). This is particularly the case in the NMDB. The results of the second aggregation of crops using SOM clustering are shown in Figure 34. The second SOM clustering resulted in 6 classes, 3 of them with high greenness (EVI>0.5, first row in Figure 34) at their peak phenology which are very likely associated to summer irrigated crops, and 3 of them with low greenness (EVI<0.5, second row in Figure 34) at their peak phenology, which may be associated to dryland crops or native vegetation. Visual inspection showed that patterns with low greenness can be associated to edge effects (i.e., pixels at the boundary of irrigated crops paddocks), an issue that affects accuracy mainly in the SMDB. Conversely in the NMDB, besides edge effects, riparian vegetation or vigorous native vegetation growth can have a similar signal as irrigated crops but lower greenness (i.e., second row in Figure 34). This issue was exacerbated in years with higher than average spring and summer rainfall leading to vigorous native vegetation growth, like in 2007-2008 (BoM, 2008). Other years with higher-than-average spring and summer rainfall that had this issue were 2003-2004, 2009-2010, and 2011-2012. Given this issue, patterns with low greenness but with a crop-like phenology (EVI<0.4, like in the second row and third column in Figure 34) were not labelled as irrigated crops in the NMDB, which may well lead to an underestimation of irrigated areas. In addition, because patterns with low greenness but with a crop-like phenology can occur in riparian areas, a recent map of agricultural paddocks (Waldner and Diakogiannis, 2020) was used to mask these patterns in the summer irrigation maps, both in the NMDB and SMDB.

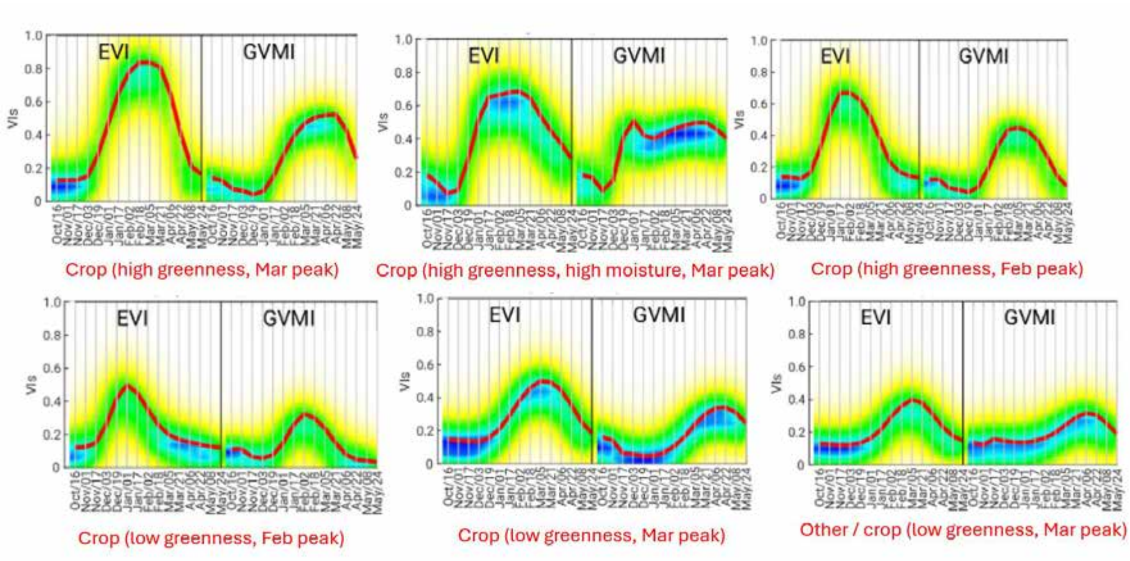

Figure 34. SOM EVI and GVMI clustered timeseries patterns for crops. The 16-day timeseries show the timeseries density (from low density expressed as yellow to high density expressed as dark blue hues) for different crop or crop-like patterns assessed in this study. The red line corresponds to the median of all timeseries.

6.3 Training data and supervised classification using neural networks

The October-April land cover maps for the years 2000-2001, 2005-2006, 2007-2008, 2010-2011 and 2017-2018 were used to build a training dataset as input to a neural network classifier. Since summer cropping covers only a small fraction (<5% in most cases) of the land cover maps, the training data is prepared using a semi-stratified sampling to reduce sampling bias. A total of ~131.1 million pixels, representing 201,760 km^2, were sampled from the above years. The characteristic of the sampling is shown in Table 3.

Table 3. Sampling characteristics for land cover according to their EVI and GVMI phenologies

Class	Land cover	Pixels	Area (km^2)	Area (%)
2	Trees	17259372	13531	13.2
3	Other vegetation	21088847	16534	16.1
4	Sparse vegetation/Bare	29879555	23426	22.8
5	Water intermittent	887953	696	0.7
6	Water permanent	728450	571	0.6
10	Crop (high greenness, Mar peak)	20984832	16452	16.0
11	Crop (high greenness, high moisture, Feb peak)	5481703	4298	4.2
12	Crop (high greenness, Feb peak)	4492191	3522	3.4
13	Crop (low greenness, Feb peak)	9614785	7538	7.3
14	Crop (low greenness, Mar peak)	9783424	7670	7.5
15	Native vegetation / crop (low greenness, Mar peak)	10870418	8522	8.3

Of the data, 70% was used for training and 15% was used for validation and 15% was used for testing. The Pattern Recognition Neural Network (PRNN) used was parameterised with 20 hidden layers and used the scaled conjugate gradient backpropagation for fast supervised learning (Moller, 1993). The performance was computed from the cross-entropy loss between the predictions and the targets. The input to the model were all the 16-day EVI and GVMI periods from September to May next year, a total of 34 periods (17 for EVI and 17 for GVMI).

Results for the validation data are shown in the confusion matrix in Figure 35. The confusion matrix presents a column summary that shows the percentages of accurately and inaccurately classified observations for each predicted class. The classes with summer cropping-like phenologies (classes 10 to 15), the main target classes for this mapping, show accuracies >80%, and >85% for the classes with high greenness (Table 3). Of the other land cover types, most have accuracies >70%, except for class 5 (water intermittent) that has a 65% accuracy, mostly getting confused with class 6 (water permanent).

Figure 35. Confusion matrix classification results of the PRNN model, with the percentage true (blue hues) and false (red hues) class and a column percentage summary. Refer to Table 3 for class labels.

Another accuracy metric, the weighted Kappa coefficient (Cohen, 1968), which considers the level of agreement that could occur by chance and thus is a robust metric, has an overall 83% accuracy.

An example of irrigated areas for the years 2000-2001, 2006-2007, 2010-2011 and 2019-2020 in the St George irrigation area is shown in Figure 36. The areal extent of irrigation in the wetter than average years 2000-2001 and 2010-2011 is contrasted with 2006-2007, at the peak of the Millenium Drought, and 2019-2020 during the Tinderbox Drought.

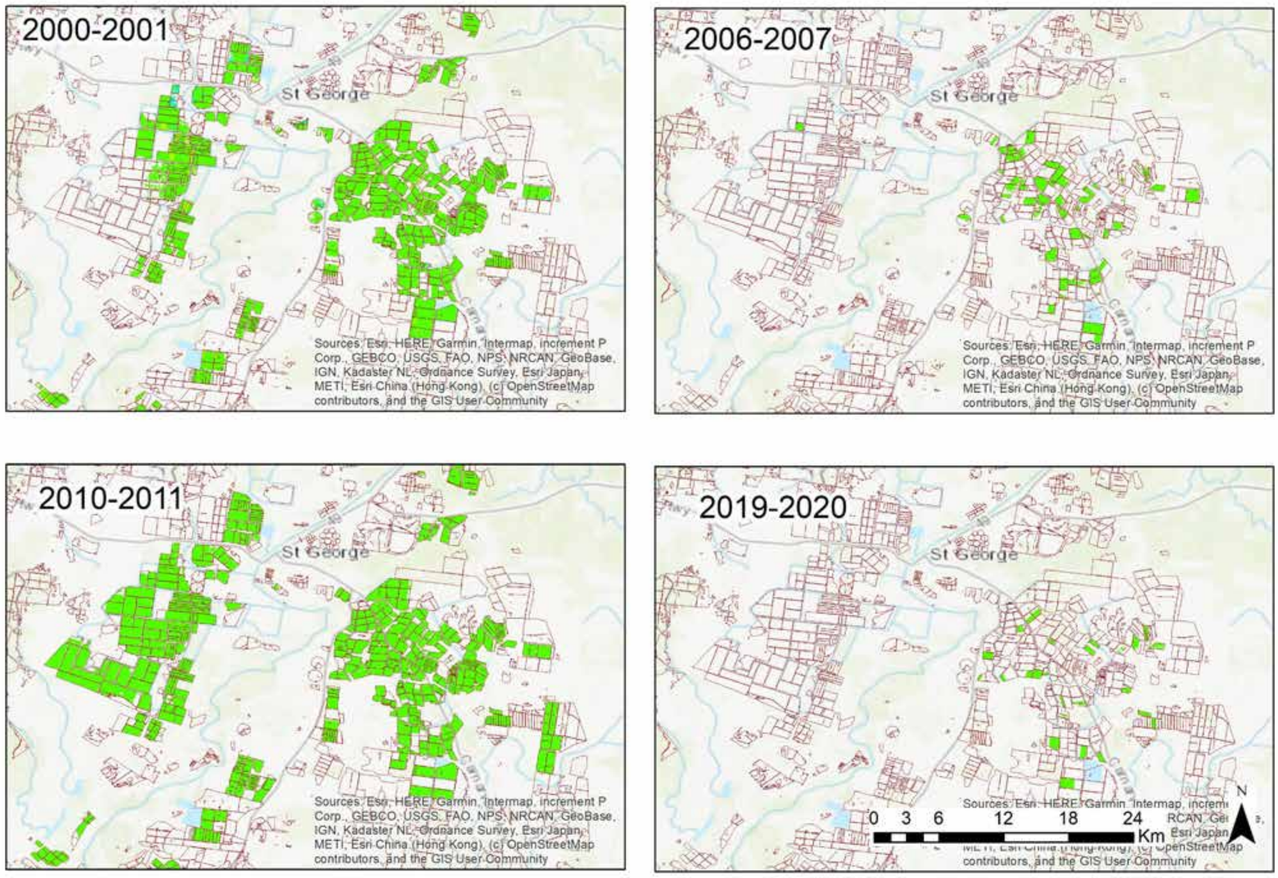

Figure 36. Summer cropping irrigation (bright green) in the St George irrigation area for 2000-2001, 2006-2007, 2010-2011 and 2019-2020. Paddock boundaries (Waldner and Diakogiannis, 2020) are in brown.

The results for all irrigated areas in the NMDB (Figure 28) compared to statistics from Cotton Yearbooks (The Australian Cottongrower, 2020) is shown in Figure 37. The goodness-of-fit statistics indicate excellent accuracy (R^2>0.9 and normalised Root mean Squared Error nRMSE<0.2) for mapped crops in most irrigated areas in the NMDB, with slopes of the regression line close to unity and very small intercepts of less than 1000 ha. The exceptions are in the Darling Downs (R^2=0.56 and nRMSE=0.25) and the Upper Namoi (R^2=0.38 and nRMSE=0.18). The Darling Downs and Upper Namoi are both located in areas with higher rainfall (>650 mm/year, Figure 1) and thus it is possible that many of the crops classified as irrigated could be dryland crops, noting that on average (2001-2002 to 2019-2020) 38% of cotton area in the Darling Downs is dryland cotton, and in the Upper Namoi is 27% (The Australian Cottongrower, 2020).

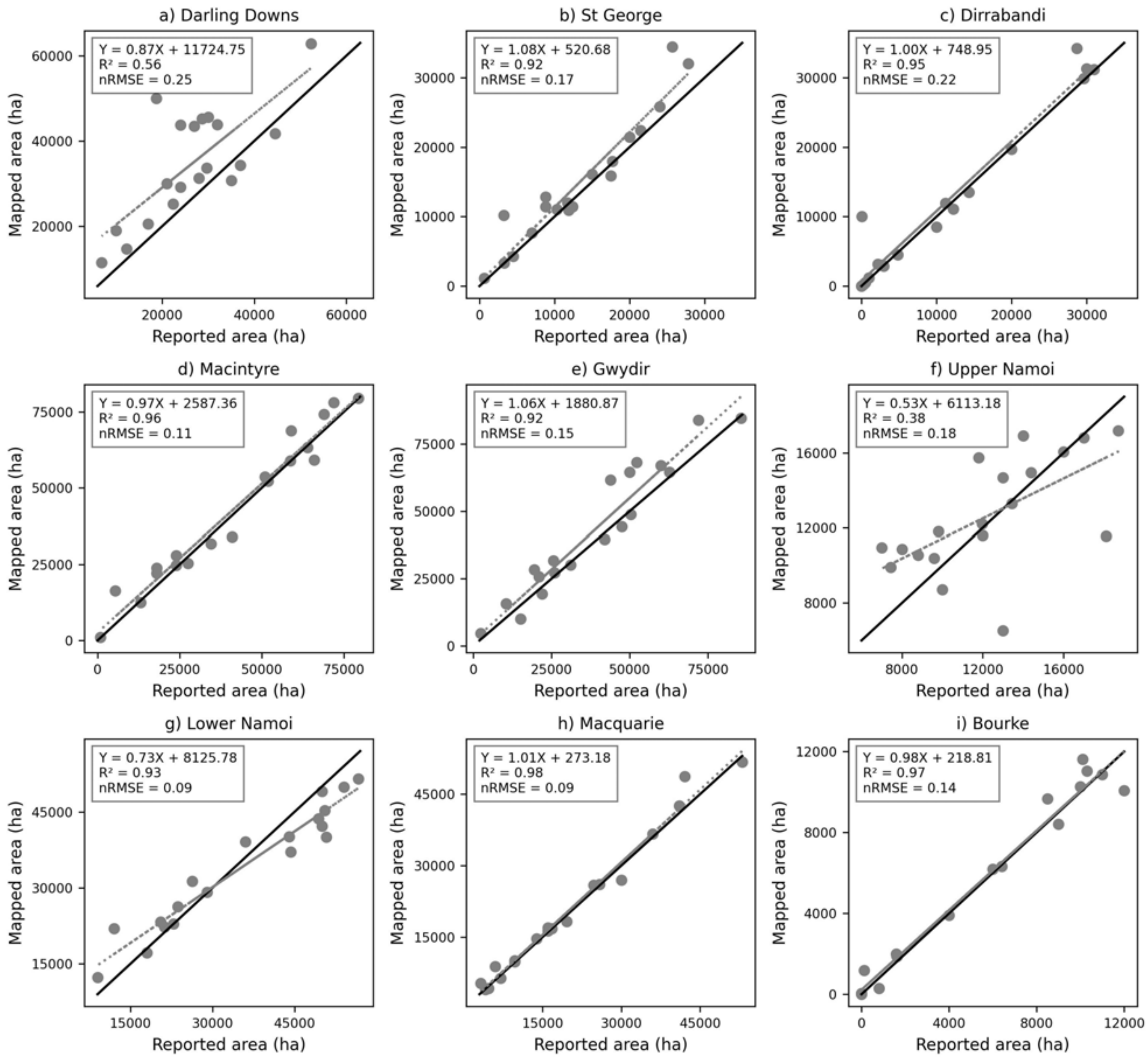

Figure 37. Scatterplot of agricultural survey statistics areas (reported areas) vs. areas mapped with the Pattern Recognition Neural Network (PRNN). Also shown are the 1:1 line (black solid line), linear regression fitted to the data (grey dashed line) and corresponding equation, the coefficient of determination (R^2), as well as the normalised (by the mean) root mean squared error (RMSE).

The comparison of the timeseries from 2000 to 2020 in Figure 38 showcases how irrigated areas vary on a year-to-year basis, and dictated by water availability, expand and contract. The natural variability of streamflow in the NMDB is buffered during dry years by the presence of large on farm floodplain storages in irrigable areas, which with a capacity of ~3,000 GL, represent ~66% of the total headwater dam reservoir capacity in the NMDB (Peña-Arancibia et al., 2024), hence irrigation was still possible during the latter years in the Millenium Drought.

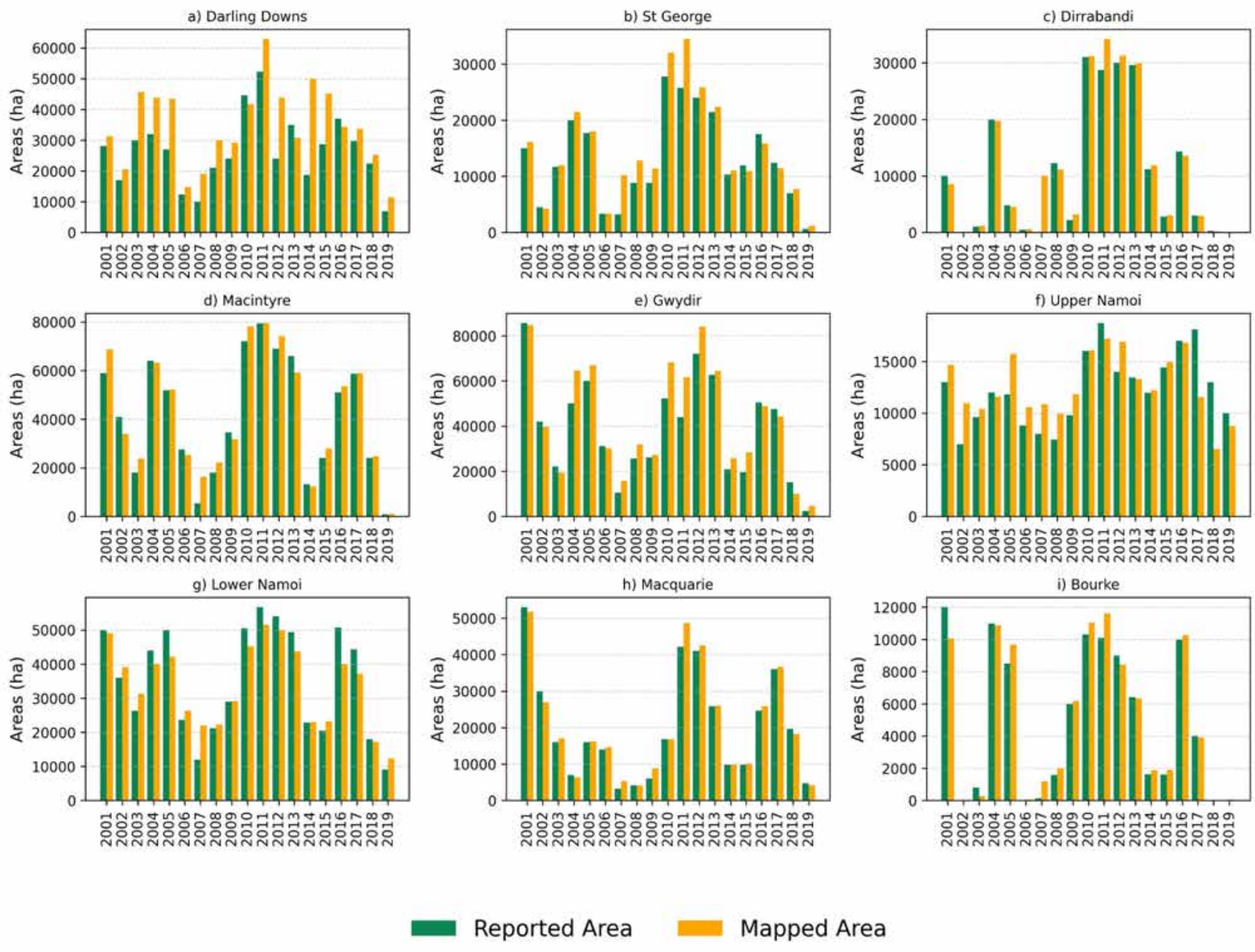

Figure 38. Timeseries for reported irrigated areas (green bars) and mapped summer irrigated areas (orange bars) in irrigated areas in the NMDB.

The associated water use for the summer irrigated areas in the NMDB irrigated regions was estimated using the CMRSET Landsat V2.2 monthly ET_a (Guerschman et al., 2022). To compute a proxy of annual summer water use, monthly rainfall was subtracted from ET_a during the crop growing window in summer cropping period (November to April) and aggregated over the six months. This proxy of water use was compared against cotton water demand from 2005 to 2017 modelled by Goesch et al. (2020). Timeseries for both estimates are shown in Figure 39. Although the temporal patterns agree, the magnitude differs, particularly during the wet period after 2010. Note that the modelling in Goesch et al. (2020) holds rainfall and water allocation prices at fixed values, whereas the proxy of water year better reflects actual crop water use. When actual water withdrawals are considered, this proxy of water use compares better with water withdrawals reported in Peña-Arancibia et al. (2023a) from MDBA (2022) estimates. In addition, the proxy of water use does not include losses in water conveyancing and storage, with on-farm storage losses estimated in Peña-Arancibia et al. (2024) accounted for 52.47 GL/year in the Barwon-Darling, which is a substantial ~27% of the estimated long-term mean regional irrigation diversion limit (189 MCM/year).

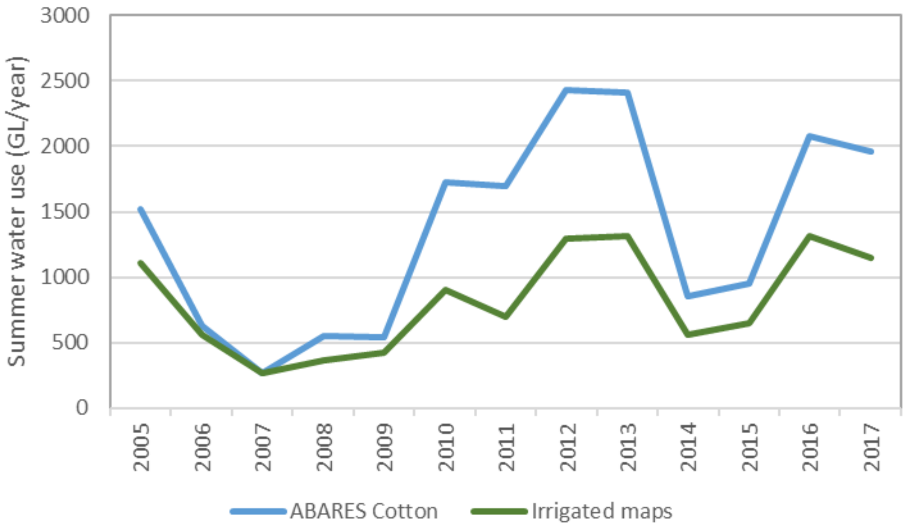

Figure 39. Timeseries comparison of a proxy of annual water use for summer irrigated areas (green line) against irrigation water demand for cotton (blue line) as estimated by Goesch et al. (2020).

7 Summary and recommendations

7.1 Weather systems and annual rainfall variability

- Changes in rainfall characteristics can result in non-stationary rainfall-runoff relationship and these can be related to changes in weather systems. The contributions of changing synoptic weather types to rainfall are essential for understanding regional water availability and water resource management.
- The contributions of 7 weather systems to rainfall and their spatiotemporal variability in the Murray-Darling Basin (MDB) were investigated with a multi-method weather type dataset and SILO gridded daily rainfall for the period of 1979–2015.
- Three weather systems, Front-Only (FO), Cyclone-Only (CO) and Thunderstorm-Only (TO) and their combinations (7 weather types) accounted for 89.3% of total rainfall with 49.3% of rainfall days for the entire MDB.
- The total number of days of FO, CO and TO and their combinations increase from northwest (40%) to southeast (55%), while their total contributions to annual rainfall show a north-south pattern.
- Thunderstorm (TO) is by far the main rainfall generating weather type in the NMDB contributing to 40% of the total rainfall, while all the weather types and their combinations contribute to the rainfall in the SMBD.
- Rainfall anomaly shows a wet period before the Millennium Drought (1975 to 2000), a dry period during the Millennium Drought (2001 to 2009), and a mixed pattern for the post-Millennium Drought (2010 to 2015) depending on geographical locations. The rainfall anomalies from each weather type are generally consistent with those of total rainfall anomalies in the three corresponding periods.
- This analysis was limited to assessing contributions of weather systems for 1975–2015 and in the pre-drought, drought and post-drought periods. Further research could explore monthly or seasonal relationships (Fu et al., 2024).
- A finer frequency analysis could also help elucidate the spatial shifts in dominant weather systems and the impacts on rainfall characteristics that are important for streamflow generation, for example number of rainfall days and for multi-day rainfall totals.
- Following from the above, this analysis can be combined with the findings in Section 3 and perform an analysis at the catchment scale. Statistical analyses or AI/ML can be used to investigate the attributions of climate variables to the nonstationary rainfall-streamflow relationships (Fu et al., 2021b).

7.2 Catchment hydrological shifts in rainfall and runoff relationship

- This research assessed hydrological non-stationarity in MDB catchments. Linear models based on annual rainfall-runoff relationship for pre-drought, drought and post-drought periods were derived for 110 unregulated and largely unimpaired catchments in the MDB, 37 in the NMDB and 73 in the SMDB, to understand the direction and magnitude of changes in the rainfall-runoff relationship and hydrological non-stationarity.
- The results provided a way to classify catchments according to the observed relationship into: (i) catchments with non-significant decline in runoff, (ii) catchments with significant runoff decline and have recovered after the drought, (iii) catchments with significant runoff decline and have partially recovered, and, (iv) catchments with significant runoff decline and have not recovered.
- Significant changes in the rainfall-runoff relationship, transitioning from higher annual runoff to lower annual runoff for the same amount of annual rainfall, were primarily observed in the SMDB. Of 73 catchments, 49 catchments (67%) experienced significant change/decline in rainfall-runoff relationship and have not recovered post drought, 7 (10%) showed significant change and have partially recovered, 5 (7%) showed significant change and have fully recovered, and 12 (16%) showed no change in the rainfall-runoff relationship.
- In the NMDB (37 catchments), no catchments had significant change/decline in the rainfall-runoff relationship without recovery, 2 (5%) had significant change and have partially recovered, 5 (14%) with significant change and have recovered, and 30 (81%) did not show change in the rainfall-runoff relationship.
- In the NMDB, only 20% of the catchments showed significant runoff decline and change in rainfall-runoff relationship during the drought, and all of them have recovered post drought. In contrast, most catchments in the SMDB showed significant runoff decline and change in rainfall-runoff relationship during the drought, and many catchments (more than half) have not fully recovered post-drought, particularly in the Wimmera, Loddon-Avoca, western Goulburn-Broken.
- The results show that hydrological non-stationarity significantly impacted the SMDB during the Millennium Drought, particularly in its drier western regions, with lingering effects. In contrast, the NMDB was less affected, with most catchments not experiencing shifts in rainfall-runoff relationship, and those that were impacted have recovered post drought.

7.3 Changes in vegetation dynamics

- Vegetation dynamics were investigated by analysing a novel long-term Leaf Area Index (LAI) dataset which covered the pre-drought, drought, and post-drought periods. LAI was separated into persistent LAI (LAI_{per}), associated with evergreen vegetation with minimal seasonal canopy variation, and recurrent LAI (LAI_{rec}), linked to vegetation with seasonal activity cycles, like grasses. Using monthly data from 1982–2020, mean values and trends during cool months (May–October) and warm months (November–April) were investigated to assess changes in LAI_{per} and LAI_{rec} contributions to vegetation dynamics.

- In the cool months, forested areas of the SMDB exhibit significant positive trends in LAI_{per}, indicating statistically significant greening. In contrast, significant positive trends in LAI_{rec} are observed only in the southern regions of the SMDB, while some eastern areas, spanning from the NMDB to the SMDB, show negative trends.
- In the warm months, forested regions of SMDB are characterized by a notably higher LAI_{per}. Outside these areas, the highest LAI_{rec} is observed in the northeast of the NMDB. During the warm months, LAI_{rec} trends are generally weaker than those in the cool months and mostly non-significant. In contrast, significant LAI_{per} trends are evident in forested areas of the SMDB, just like in the cool months.

When analysed over the 110 catchments in Section 3 the analysis found:

- Non-shifted catchments (n=42, NMDB): slight declines (~5%) in median LAI and LAI_{per} during the drought (annual LAI: 1.63 → 1.55 m^2/m^2), with minimal change in LAI_{rec}. Increased variance (IQR) in LAI and LAI_{per} during cool months toward higher values. Post-drought increases in LAI and LAI_{per} compared to drought levels, while LAI_{rec} remained largely stable.
- Shifted and recovering/recovered catchments (n=19, NMDB: 7, SMDB: 12): similar patterns to non-shifted catchments, with smaller median declines (~2%, annual LAI: 1.88 → 1.85 m^2/m^2) during the drought. Slight post-drought increases in LAI and LAI_{per}, with variance remaining consistent across periods.
- Shifted and non-recovered catchments (n=49, SMDB): More pronounced declines (~7%) in median LAI and LAI_{per} during the drought (annual LAI: 1.99 → 1.86 m^2/m^2), with little change in LAI_{rec}. Post-drought increases in median LAI_{per} (~8%, 1.26 → 1.36 m^2/m^2), while LAI_{rec} values showed minimal increases. Variability showed less change compared to non-shifted catchments.
- To assess long-term (1980 to 2022) actual evapotranspiration dynamics (ET_a) at the catchment scale, the 25km spatial resolution monthly Global Land Evaporation Amsterdam Model (GLEAM) was downscaled to 500 m using 'evaporative fraction' approach.
- The resulting ET_a estimates were evaluated against catchment water balance, assuming no change in soil storage over the data periods, and as such ET_a was compared to the difference between rainfall (P) and streamflow (Q) in the 110 catchments in the MDB.
- Overall, linear regression statistics indicate that differences between GLEAM and downscaled GLEAM are minimal.
- The downscaled GLEAM ET_a data, along with P and Q, were analysed for the 110 MDB catchments, during the pre-drought, drought, and post-drought periods.
- In the NMDB, declines in ET_a mirrored decreases in P, whereas in the SMDB, ET_a remained relatively stable despite declines in P. This pattern persisted in the SMDB during the post-drought period. During the warm months in both NMDB and SMDB, changes in ET_a closely followed changes in P, and the ratios of median ET_a to P remained consistent across the pre-drought, drought, and post-drought periods. This partly explains the significant runoff declines and shifts in rainfall-runoff relationship in the SMDB compared to the NMDB.

- Both diagnostic datasets, LAI (and its components) and ET_a can be used as inputs to hydrological models or to evaluate model outputs, as well as used in statistical analyses to assess causality of rainfall-runoff shifts.

7.4 Sensitivity of runoff to drivers of non-stationarity

- This research progressively adapted a rainfall-runoff model by considering the hydrological effects of farm dams and vegetation dynamics, as seen in the remotely sensed satellite data. The adapted models outperformed the original rainfall-runoff model in most of the studied catchments in terms of their overall model performance and robustness.
- The adapted model considering impacts of farm dams performed better than that considering the effects of vegetation dynamics. The model considering both the impacts from farm dams and vegetation dynamics does not necessarily further improve model performance, particularly in the NMDB catchments, indicating complex interplays between hydrologic processes related to farm dams and vegetation dynamics.
- The adapted model was used to quantify sensitivity of annual runoff to rainfall, PET, LAI and farm dams' volumes. Median elasticity coefficients of rainfall, PET, LAI and farm dams' volumes were around 2.7, -0.8, -0.5, and -0.2 respectively across the MDB.
- As expected, streamflow was most sensitive to the climate inputs (rainfall and PET). Farm dams, and to a lesser extent LAI, are also important secondary drivers of streamflow response.
- Catchments in the NMDB are found more sensitive to rainfall and vegetation dynamics than those in the SMDB, while the effects of PET and farm dams on streamflow are more evident in the SMDB than those in the NMDB.
- For runoff changes in the drought period, median contributions from rainfall, PET, LAI and farm dams' volumes are around -41%, -2%, 1% and -15% respectively. Reduction in rainfall and growth in farm dams' volumes during the drought period are the most important drivers leading to lower runoff in the Millennium drought.
- Uncertainties in this research can be from the remotely sensed LAI and farm dams' characteristics, structures of the adapted models and parameterization schemes. Particularly, the hydrological effect of vegetation dynamics is considered by solely relating LAI to evapotranspiration. More complex interactions between vegetation dynamics and hydrological processes may need to be further investigated in the future. In addition, the model can be further improved to better reflect hydrological non-stationarity by enhancing conceptualization of the interactions between surface water and groundwater.
- To improve the robustness and reliability of hydrological modelling, it is recommended to reassess calibrations and/or conceptualisation (i.e., adding a farm dams module, for example) of rainfall-runoff models, particularly for catchments exhibiting significant shifts in rainfall-runoff relationships during the Millenium Drought. These shifts, observed during the drought and post-drought periods compared to the pre-drought period, indicate hydrological non-stationarity.

7.5 Quantifying irrigation areas and water use

- This research maximised remote sensing data availability using a blending approach to extract features of vegetation phenology, mainly related to summer irrigation cropping across the MDB (November to April). The data, encompassing 2000 to 2020, combined low spatial resolution, high-frequency satellite imagery with high spatial resolution, low-frequency imagery to generate two continuous, gap-free vegetation indices: the Enhanced Vegetation Index (EVI) which provides a proxy for vegetation health, and the Global Vegetation Moisture Index (GVMI) which provides a proxy of vegetation moisture, with a 16-day temporal resolution and 30 m spatial resolution.
- The data were used in a semi-supervised neural network approach to extract vegetation (and other land covers) phenology patterns, focused on summer irrigated areas and then map them every season from 2000 to 2020.
- A pattern Recognition Neural Network (PRNN) was trained using data extracted from neural-network Self-Organising Maps. The training data included the following land covers: trees, other vegetation, sparse vegetation/bare, water intermittent, water permanent, crops. Crops were further subdivided in 5 classes showcasing differences in growth patterns, particularly greenness peak and vigour (i.e., higher EVI). Crop classes showed accuracies >80%, and >85% for the classes with high greenness. Of the other land cover types, most have accuracies >70%.
- The PRNN was used to predict summer land covers from 2000 to 2020 and validated using survey statistics. In the NMDB the PRNN mapping generally showed very high accuracies (R^2>0.9) against cotton area estimates. The comparison of the cotton area timeseries from 2000 to 2020 showcased how irrigated areas vary on a year-to-year basis, and dictated by water availability, expand and contract.
- The associated water use for the summer irrigated areas in the NMDB irrigated regions was estimated by subtracting rainfall from the CMRSET Landsat V2.2 monthly ET_a and compared to water demand survey statistics, showing good temporal agreement (although magnitudes differed due to different modelling assumptions).
- In this research only summer irrigated crops were considered, but phenology signals were also extracted for irrigated pastures and horticulture. Training models to predict the locations of these can help elucidate the irrigation dynamics in the MDB, including overall water use under different climate conditions. In addition, landscape transformations (e.g. from rice to cotton cropping, or from crops to orchards) in the MDB can be analysed using the above approach. Further, the methods in this research can be operationalised to enable a crop monitoring system that not only detects crops but also their water use (using CMRSET ET_a, for example).

Appendix A Catchment selection criteria

The Hydrological Reference Stations (HRS, see http://www.bom.gov.au/water/hrs/about.shtml, accessed November 2024) provide long-term high quality streamflow records. There are 133 HRS catchments across the MDB, with most of these located in the eastern and southern uplands, areas that generate most of the MDBs catchment runoff (Peña-Arancibia et al., 2023a, Figure 1). Of the 133, 37 are in the NMDB and 96 in the SMDB. In this research, which focuses on the MDB but particularly on the NMDB, a number of catchments were added or excluded for a variety of reasons. Catchments added were due to their location in the NMDB, and similar quality checks as for HRS catchments were conducted for new catchments included, namely, long-term quality records and minimal effects of water resource development and land use change. Streamflow data for the added catchments was sourced from the Bureau of Meteorology Water Data Online (http://www.bom.gov.au/waterdata/, accessed November 2024) and their catchment boundaries were obtained from the Hydrologically Enforced Digital Elevation Model (DEM-H, GA, 2015). HRS catchments that were excluded had either: (i) insufficient annual records for the rainfall-runoff analysis conducted in Chapter 3 (i.e., 1985 to 2020), (ii) a dam or other infrastructure in its headwaters regulating flow, (iii) mean annual (1985 to 2020) differences ≥10% between SILO and AGCD datasets (Fu et al., 2022), (iv) no quality information and (v) unsuitable location of gauging station.

- Five catchments were added: 416022 (Border Rivers), 416305 (Border Rivers), 422219 (Condamine), 423203 (Warrego), 423204 (Warrego).
- Eight catchments were removed due to insufficient records: 402217 (Murray), 405263 (Goulburn-Broken), 408206 (Loddon-Avoca), 410156 (Murrumbidgee), 412028 (Lachlan), 415245 (Wimmera), 421048 (Macquarie-Castlereagh), 422321B (Condamine).
- Five were removed due to regulation: 410026 (Murrumbidgee), 410033 (Murrumbidgee, downstream of Tantangara reservoir), 410761 (Murrumbidgee, downstream of Tantangara reservoir), 406214 (Campaspe), 407253 (Loddon-Avoca).
- Eleven were removed due to rainfall differences between SILO and AGCD: 401009 (Murray), 401012 (Murray), 401203 (Murray), 401210 (Murray), 401212 (Murray), 401216 (Murray), 401217 (Murray), 405241(Goulburn-Broken), 405264 (Goulburn-Broken), A4260533 (Eastern Mt Lofty Ranges). 405227 (Goulburn-Broken).
- Two were removed due to data quality flags missing: 401016 (Murray) and 419010 (Namoi).
- Two were removed due to unsuitable gauge location: 424002 (Paroo), 424201A (Paroo).

References

ABARES, 2012. Cropping calendars for natural resource management regions of Australia 2010 – August 2012–, Australian Bureau of Agricultural and Resource Economics and Sciences, Canberra, Australia, pp. 7. https://www.agriculture.gov.au/sites/default/files/abares/aclump/documents/UserGuide_CropCalendars_2010.docx, last access: December 2024.

ABARES, 2021. Catchment Scale Land Use of Australia – Update December 2020, Australian Bureau of Agricultural and Resource Economics and Sciences, Canberra, Australia. https://www.agriculture.gov.au/abares/aclump/catchment-scale-land-use-of-australia-update-december-2020, last access: December 2024.

ABS, 2019. 75030DO002_201718 Value of Agricultural Commodities Produced, Australia, 2017-18, Australian Bureau of Statistics. https://www.abs.gov.au/statistics/industry/agriculture/value-agricultural-commodities-produced-australia/2017-18/75030do002_201718.xls, last access: September 2024.

ABS, 2023. Water use on Australian Farms–2020-21, Australian Bureau of Statistics. https://www.abs.gov.au/statistics/industry/agriculture/water-use-australian-farms/latest-release#murray-darling-basin, last access: November 2024.

Ajami, H, Sharma, A, Band, LE, Evans, JP, Tuteja, NK, Amirthanathan, GE, Bari, MA, 2017. On the non-stationarity of hydrological response in anthropogenically unaffected catchments: an Australian perspective. Hydrology and Earth System Sciences, 21(1): 281-294. http://doi.org/10.5194/hess-21-281-2017

Allen, RG, Pereira, LS, Raes, D, Smith, M, 1998. Crop evapotranspiration - Guidelines for computing crop water requirements - FAO Irrigation and drainage paper 56, Food and Agricultural Organisation of the United Nations, Rome. http://www.fao.org/3/x0490e/x0490e00.htm, last access: October 2024.

Amirthanathan, GE, Bari, MA, Woldemeskel, FM, Tuteja, NK, Feikema, PM, 2023. Regional significance of historical trends and step changes in Australian streamflow. Hydrology and Earth System Sciences, 27(1): 229-254. http://doi.org/10.5194/hess-27-229-2023

Beck, HE, Zimmermann, NE, McVicar, TR, Vergopolan, N, Berg, A, Wood, EF, 2018. Present and future Koppen-Geiger climate classification maps at 1-km resolution. Scientific Data, 5. http://doi.org/10.1038/sdata.2018.214

BoM, 2008. Annual Climate Summary 2007, Bureau of Meteorology, pp. 19. http://www.bom.gov.au/climate/annual_sum/2007/AnClimSum07.pdf, last access: November 2024.

BoM, 2020. Special Climate Statement 70—drought conditions in Australia and impact on water resources in the Murray–Darling Basin, Bureau of Meteorology, Australia, pp. 18. http://www.bom.gov.au/climate/current/statements/scs70.pdf, last access: December 2024.

BoM, 2022. Recent and historical rainfall maps - 2017 rainfall anomaly, Bureau of Meteorology. http://www.bom.gov.au/climate/maps/rainfall/, last access: September 2023.

Box, GEP, Cox, DR, 1964. An analysis of transformations. Journal of the Royal Statistical Society Series B-Statistical Methodology, 26(2): 211-252. http://doi.org/10.1111/j.2517-6161.1964.tb00553.x

Callaghan, J, 2019. A comparison of weather systems in 1870 and 1956 leading to extreme floods in the Murray Darling Basin. Journal of Southern Hemisphere Earth Systems Science, 69(1): 84-115. http://doi.org/10.1071/Es19003

Cao, RY, Chen, Y, Shen, MG, Chen, J, Zhou, J, Wang, C, Yang, W, 2018. A simple method to improve the quality of NDVI time-series data by integrating spatiotemporal information with the Savitzky-Golay filter. Remote Sensing of Environment, 217: 244-257. http://doi.org/10.1016/j.rse.2018.08.022

Cao, S, Li, M, Zhu, Z, Zha, J, Zhao, W, Duanmu, Z, Chen, J, Zheng, Y, Chen, Y, 2023. Spatiotemporally consistent global dataset of the GIMMS Leaf Area Index (GIMMS LAI4g) from 1982 to 2020. Earth Syst. Sci. Data, 2023(15): 4877–4899. http://doi.org/10.5194/essd-15-4877-2023

Ceccato, P, Flasse, S, Gregoire, JM, 2002a. Designing a spectral index to estimate vegetation water content from remote sensing data-Part 2. Validation and applications. Remote Sensing of Environment, 82(2): 198-207. http://doi.org/10.1016/S0034-4257(02)00036-6

Ceccato, P, Gobron, N, Flasse, S, Pinty, B, Tarantola, S, 2002b. Designing a spectral index to estimate vegetation water content from remote sensing data: Part 1 - Theoretical approach. Remote Sensing of Environment, 82(2-3): 188-197. http://doi.org/10.1016/S0034-4257(02)00037-8

Chiew, FHS, 2006. Estimation of rainfall elasticity of streamflow in Australia. Hydrological Sciences Journal, 51(4): 613-625. http://doi.org/10.1623/hysj.51.4.613

Chiew, FHS, McMahon, TA, 1991. The applicability of Morton's and Penman's evapotranspiration estimates in rainfall-runoff modeling. Water Resources Bulletin, 27(4): 611-620. http://doi.org/10.1111/j.1752-1688.1991.tb01462.x

Chiew, FHS, Peel, MC, McMahon, TA, Siriwardena, LW (2006), Precipitation elasticity of streamflow in catchments across the world, Demuth, S., Gustard, A., Planos, E., Scatena, F., Servat, E. (Eds.), Climate Variability and Change - Hydrological Impacts - 5th FRIEND World Conference, Havana, Cuba, November 2006, 256-262, https://iahs.info/uploads/dms/13670.49-256-262-08-308-Chiew.pdf

Chiew, FHS, Potter, NJ, Vaze, J, Petheram, C, Zhang, L, Teng, J, Post, DA, 2014. Observed hydrologic non-stationarity in far south-eastern Australia: implications for modelling and prediction. Stochastic Environmental Research and Risk Assessment, 28(1): 3-15. http://doi.org/10.1007/s00477-013-0755-5

Chiew, FHS, Weber, TR, Aryal, SK, Post, DA, Vaze, J, Zheng, H, Peña Arancibia, JL, Robertson, DE, 2022a. Evaluation of causes of reduced flow in the northern Murray–Darling Basin. CSIRO Technical report for the Murray–Darling Basin Authority., pp. 62. https://www.mdba.gov.au/sites/default/files/publications/evaluation-of-causes-of-reduced-flow-northern-mdb-with-errata.pdf, last access: December 2024.

Chiew, FHS, Zheng, H, Post, DA, Robertson, DE, Rojas, R, 2022b. Hydroclimate trends and future projections in the Murray-Darling Basin, CSIRO Technical report for the Murray-Darling Basin Authority, pp. 50. https://www.mdba.gov.au/sites/default/files/publications/mdb-outlook-hydroclimate-literature-review2.pdf, last access: December 2024.

Cohen, J, 1968. Weighted Kappa - Nominal Scale Agreement with Provision for Scaled Disagreement or Partial Credit. Psychological Bulletin, 70(4): 213-220. http://doi.org/10.1037/h0026256

Coron, L, Andréassian, V, Perrin, C, Lerat, J, Vaze, J, Bourqui, M, Hendrickx, F, 2012. Crash testing hydrological models in contrasted climate conditions: An experiment on 216 Australian catchments. Water Resources Research, 48. http://doi.org/10.1029/2011wr011721

Deb, P, Kiem, AS, Willgoose, G, 2019. Mechanisms influencing non-stationarity in rainfall-runoff relationships in southeast Australia. Journal of Hydrology, 571: 749-764. http://doi.org/10.1016/j.jhydrol.2019.02.025

Devanand, A, Falster, GM, Gillett, ZE, Hobeichi, S, Holgate, CM, Jin, CH, Mu, MY, Parker, T, Rifai, SW, Rome, KS, Stojanovic, M, Vogel, E, Abram, NJ, Abramowitz, G, Coats, S, Evans, JP, Gallant, AJE, Pitman, AJ, Power, SB, Rauniyar, SP, Taschetto, AS, Ukkola, AM, 2024. Australia's Tinderbox Drought: An extreme natural event likely worsened by human-caused climate change. Science Advances, 10(10). http://doi.org/10.1126/sciadv.adj3460

Donohue, RJ, McVicar, TR, Roderick, ML, 2009. Climate-related changes in Australian vegetation cover as inferred from satellite observations for 1981-2006. Global Change Biology, 15(4): 1025-1039. http://doi.org/10.1111/j.1365-2486.2008.01746.x

Durbin, J, Watson, GS, 1950. Testing for Serial Correlation in Least Squares Regression .1. Biometrika, 37(3-4): 409-428. http://doi.org/10.1093/biomet/37.3-4.409

Fowler, K et al., 2022. Explaining changes in rainfall–runoff relationships during and after Australia's Millennium Drought: a community perspective. Hydrol. Earth Syst. Sci., 26(23): 6073-6120. http://doi.org/10.5194/hess-26-6073-2022

Fu, G, Chiew, FHS, Post, DA, Pepler, AS, Rudeva, I, 2024. Attributions of Rainfall Anomalies to Weather Systems and Their Spatial and Temporal Variabilities: A Case Study of Victoria in Southeast Australia. International Journal of Climatology. http://doi.org/10.1002/joc.8644

Fu, G, Chiew, FHS, Zheng, H, Robertson, DE, Potter, NJ, Teng, J, Post, DA, Charles, SP, Zhang, L, 2021a. Statistical analysis of attributions of climatic characteristics to nonstationary rainfall-streamflow relationship. Journal of Hydrology, 603: 127017. http://doi.org/10.1016/j.jhydrol.2021.127017

Fu, GB, Barron, O, Charles, SP, Donn, MJ, Van Niel, TG, Hodgson, G, 2022. Uncertainty of Gridded Precipitation at Local and Continent Scales: A Direct Comparison of Rainfall from SILO and AWAP in Australia. Asia-Pacific Journal of Atmospheric Sciences, 58(4): 471-488. http://doi.org/10.1007/s13143-022-00267-4

Fu, GB, Chiew, FH, Zheng, HX, Robertson, DE, Potter, NJ, Teng, J, Post, DA, Charles, SP, Zhang, L, 2021b. Statistical analysis of attributions of climatic characteristics to nonstationary rainfall-streamflow relationship. Journal of Hydrology, 603. http://doi.org/10.1016/j.jhydrol.2021.127017

Fu, GB, Chiew, FHS, Post, DA, 2023. Trends and variability of rainfall characteristics influencing annual streamflow: A case study of southeast Australia. International Journal of Climatology, 43(3): 1407-1430. http://doi.org/10.1002/joc.7923

GA, 2015. Digital Elevation Model (DEM) of Australia derived from SRTM with 1 Second Grid - Hydrologically Enforced, Geoscience Australia, Australia. https://portal.ga.gov.au/metadata/elevation-and-depth/elevation/digital-elevation-model-dem-of-australia-derived-from-srtm-with-1-second-grid-hydrologically-enforced/5f027682-4510-4756-9aae-731bf2389070, last access: September 2024.

Gallant, AJE, Kiem, AS, Verdon-Kidd, DC, Stone, RC, Karoly, DJ, 2012. Understanding hydroclimate processes in the Murray-Darling Basin for natural resources management. Hydrology and Earth System Sciences, 16(7): 2049-2068. http://doi.org/10.5194/hess-16-2049-2012

Goesch, T, Legg, P, Donoghoe, M, 2020. Murray–Darling Basin water markets: Trends and drivers 2002–03 to 2018–19, Australian Bureau of Agricultural and Resource Economics, Canberra, pp. 44. https://daff.ent.sirsidynix.net.au/client/en_AU/search/asset/1029942/0, last access: September 2024.

Guerschman, JP, McVicar, TR, Vleeshower, J, Van Niel, TG, Peña-Arancibia, JL, Chen, Y, 2022. Estimating actual evapotranspiration at field-to-continent scales by calibrating the CMRSET algorithm with MODIS, VIIRS, Landsat and Sentinel-2 data. Journal of Hydrology, 605. http://doi.org/10.1016/j.jhydrol.2021.127318

Huete, A, Didan, K, Miura, T, Rodriguez, EP, Gao, X, Ferreira, LG, 2002. Overview of the radiometric and biophysical performance of the MODIS vegetation indices. Remote Sensing of Environment, 83(1–2): 195-213. http://doi.org/10.1016/S0034-4257(02)00096-2

Hughes, JD, Vaze, J, 2015. Non-stationarity driven by long-term change in catchment storage: possibilities and implications. Hydrologic Non-Stationarity and Extrapolating Models to Predict the Future, 371: 7-12. http://doi.org/10.5194/piahs-371-7-2015

Jeffrey, SJ, Carter, JO, Moodie, KB, Beswick, AR, 2001. Using spatial interpolation to construct a comprehensive archive of Australian climate data. Environmental Modelling and Software, 16(4): 309-330. http://doi.org/10.1016/S1364-8152(01)00008-1

Jones, DA, Wang, W, Fawcett, R, 2009. High-quality spatial climate data-sets for Australia. Australian Meteorological and Oceanographic Journal, 58(4): 233-248.

Killick, R, Fearnhead, P, Eckley, IA, 2012. Optimal Detection of Changepoints With a Linear Computational Cost. Journal of the American Statistical Association, 107(500): 1590-1598. http://doi.org/10.1080/01621459.2012.737745

Kohonen, T, 1998. Self-Organization and Associative Memory. Springer Series in Information Sciences, 8ed. Springer Berlin, Heidelberg, pp. 312. http://doi.org/10.1007%2F978-3-662-00784-6

Kondo, J, 1998. Dependence of Evapotranspiration on the Precipitation Amount and Leaf area Index for Various Vegetated surfaces. Journal of Japan Society of Hydrology and Water Resources, 11(7): 679-693. http://doi.org/10.3178/jjshwr.11.679

Li, XD, Foody, GM, Boyd, DS, Ge, Y, Zhang, YH, Du, Y, Ling, F, 2020. SFSDAF: An enhanced FSDAF that incorporates sub-pixel class fraction change information for spatio-temporal image fusion. Remote Sensing of Environment, 237. http://doi.org/10.1016/j.rse.2019.111537

Martens, B, Miralles, DG, Lievens, H, van der Schalie, R, de Jeu, RAM, Fernandez-Prieto, D, Beck, HE, Dorigo, WA, Verhoest, NEC, 2017. GLEAM v3: satellite-based land evaporation and root-zone soil moisture. Geoscientific Model Development, 10(5): 1903-1925. http://doi.org/10.5194/gmd-10-1903-2017

MDBA, 2022. Annual Water Take Report 2020−2021. Report on Basin wide water availability, use and Cap compliance, Murray−Darling Basin Authority, pp. 141. https://www.mdba.gov.au/sites/default/files/pubs/annual-water-take-report-2020-21.pdf, last access: December 2024.

Miralles, DG, Holmes, TRH, Jeu, RAMd, Gash, JH, Meesters, AGCA, Dolman, AJ, 2011. Global land-surface evaporation estimated from satellite-based observations. Hydrology and Earth System Sciences, 15(2): 453-469. http://doi.org/0.5194/hess-15-453-2011

Moller, MF, 1993. A Scaled Conjugate-Gradient Algorithm for Fast Supervised Learning. Neural Networks, 6(4): 525-533. http://doi.org/10.1016/S0893-6080(05)80056-5

Morton, FI, 1983. Operational estimates of areal evapotranspiration and their significance to the science and practice of hydrology. Journal of Hydrology, 66(1-4): 1-76. http://doi.org/10.1016/0022-1694(83)90177-4

Nash, JE, Sutcliffe, JV, 1970. River flow forecasting through conceptual models part I — A discussion of principles. Journal of Hydrology, 10(3): 282–290. http://doi.org/10.1016/0022-1694(70)90255-6

Nicholls, N, Drosdowsky, W, Lavery, B, 1997. Australian rainfall variability and change. Weather, 52: 66-71. http://doi.org/10.1002/j.1477-8696.1997.tb06274.x.

Peña-Arancibia, JL, Chiew, FHS, Yu, Y, Fu, G, 2023a. Hydroclimate and catchment processes impacting runoff in the northern Murray−Darling Basin. CSIRO Technical report for the Murray–Darling Basin Authority, CSIRO, Australia, pp. 46. https://www.mdba.gov.au/sites/default/files/publications/t2.h.2-hydroclimate-and-

catchment-processes-impacting-runoff-northern-murray-darling-basin.pdf, last access: November 2024.
Peña-Arancibia, JL, Golam Mahboob, M, Islam, T, Mainuddin, M, Yu, Y, Ahmad, MD, Ibn Murad, K, Saha, K, Hossain, A, Moniruzzaman, M, Ticehurst, C, Kong, DD, 2021. The Green Revolution from space: mapping the historic dynamics of main rice types in one of the world's food bowls. Remote Sensing Applications: Society and Environment, 21. http://doi.org/10.1016/j.rsase.2020.100460
Peña-Arancibia, JL, Malerba, ME, Wright, N, Robertson, DE, 2023b. Characterising the regional expansion of on-farm storages and their implications for water resources in the light of climate change. Journal of Hydrology, 625, Part B. http://doi.org/10.1016/j.jhydrol.2023.130097
Peña-Arancibia, JL, McVicar, TR, Paydar, Z, Li, LT, Guerschman, JP, Donohue, RJ, Dutta, D, Podger, GM, van Dijk, AIJM, Chiew, FHS, 2014. Dynamic identification of summer cropping irrigated areas in a large basin experiencing extreme climatic variability. Remote Sensing of Environment, 154: 139-152. http://doi.org/10.1016/j.rse.2014.08.016
Peña-Arancibia, JL, Ticehurst, CJ, Yu, Y, McVicar, TR, Marvanek, SP, 2024. Feasibility of monitoring floodplain on-farm water storages by integrating airborne and satellite LiDAR altimetry with optical remote sensing. Remote Sensing of Environment, 302: 113992. http://doi.org/https://doi.org/10.1016/j.rse.2024.113992
Pepler, AS, Dowdy, AJ, van Rensch, P, Rudeva, I, Catto, JL, Hope, P, 2020. The contributions of fronts, lows and thunderstorms to southern Australian rainfall. Climate Dynamics, 55(5-6): 1489-1505. http://doi.org/10.1007/s00382-020-05338-8
Perrin, C, Michel, C, Andreassian, V, 2003. Improvement of a parsimonious model for streamflow simulation. Journal of Hydrology, 279(1-4): 275-289. http://doi.org/10.1016/s0022-1694(03)00225-7
Peterson, TJ, Saft, M, Peel, MC, John, A, 2021. Watersheds may not recover from drought. Science, 372(6543): 745-749. http://doi.org/doi:10.1126/science.abd5085
Priestley, CHB, Taylor, RJ, 1972. On the assessment of surface heat flux and evaporation using large-scale parameters. Monthly Weather Review, 100: 81-92. http://doi.org/10.1175/1520-0493(1972)100<0081:OTAOSH>2.3.CO;2
Rassam, DW, Pagendam, D, Gilfedder, M, Zhang, L, 2017. Non-stationarity of low flows and their relevance to river modelling during drought periods. Marine and Freshwater Research, 68(12): 2306-2314. http://doi.org/10.1071/Mf16399
Rifai, SW, De Kauwe, MG, Ukkola, AM, Cernusak, LA, Meir, P, Medlyn, BE, Pitman, AJ, 2022. Thirty-eight years of CO2 fertilization has outpaced growing aridity to drive greening of Australian woody ecosystems. Biogeosciences, 19(2): 491-515. http://doi.org/10.5194/bg-19-491-2022
Robertson, DE, Zheng, HX, Peña-Arancibia, JL, Chiew, FHS, Aryal, S, Malerba, ME, N., W, 2023. How sensitive are catchment runoff estimates to on-farm storages under current and future climates? Journal of Hydrology, 626(Part A). http://doi.org/10.1016/j.jhydrol.2023.130185
Saft, M, Peel, MC, Western, AW, Zhang, L, 2016. Predicting shifts in rainfall-runoff partitioning during multiyear drought: Roles of dry period and catchment characteristics. Water Resources Research, 52(12): 9290-9305. http://doi.org/10.1002/2016wr019525
Savitzky, A, Golay, MJE, 1964. Smoothing + Differentiation of Data by Simplified Least Squares Procedures. Analytical Chemistry, 36(8): 1627-&. http://doi.org/10.1021/ac60214a047
Strahler, AH, Lucht, W, Schaaf, C, Tsang, T, Gao, F, Li, X, Muller, JP, Lewis, P, Barnsley, M, 1999. MODIS BRDF/Albedo Product: Algorithm Theoretical Basis Document Version 5.0, pp. 53. https://lpdaac.usgs.gov/documents/97/MCD43_ATBD.pdf, last access: October 2024.

Tang, QH, Lettenmaier, DP, 2012. 21st century runoff sensitivities of major global river basins. Geophysical Research Letters, 39. http://doi.org/10.1029/2011gl050834
The Australian Cottongrower, 2020. Cotton Yearbook 2020, The Australian Cottongrower, Australia, pp. 200. https://www.cottongrower.com.au/, last access: November 2024.
Ukkola, AM, Prentice, IC, Keenan, TF, van Dijk, AIJM, Viney, NR, Myneni, RB, Bi, J, 2016. Reduced streamflow in water-stressed climates consistent with CO2 effects on vegetation. Nature Climate Change, 6(1): 75-+. http://doi.org/10.1038/Nclimate2831
van Dijk, AIJM, Beck, HE, Crosbie, RS, de Jeu, RAM, Liu, YY, Podger, GM, Timbal, B, Viney, NR, 2013. The Millennium Drought in southeast Australia (2001-2009): Natural and human causes and implications for water resources, ecosystems, economy, and society. Water Resources Research, 49(2): 1040-1057. http://doi.org/10.1002/wrcr.20123
Vaze, J, Post, DA, Chiew, FHS, Perraud, JM, Viney, NR, Teng, J, 2010. Climate non-stationarity - Validity of calibrated rainfall-runoff models for use in climate change studies. Journal of Hydrology, 394(3-4): 447-457. http://doi.org/10.1016/j.jhydrol.2010.09.018
Viney, NR, Perraud, J, Vaze, J, Chiew, FHS, Post, DA, Yang, A, 2009. The usefulness of bias constraints in model calibration for regionalisation to ungauged catchments. In: Anderssen, R.S., Braddock, R.D., Newham, L.T.H. (Eds.), 18th World Imacs Congress and Modsim09 International Congress on Modelling and Simulation: Interfacing Modelling and Simulation with Mathematical and Computational Sciences, Cairns, Australia, pp. 3421-3427. http://mssanz.org.au/modsim09/I7/viney_I7a.pdf
Waldner, F, Diakogiannis, F, 2020. Deep learning on edge: Extracting field boundaries from satellite images with a convolutional neural network. Remote Sensing of Environment, 245. http://doi.org/10.1016/j.rse.2020.111741
Winkler, AJ, Myneni, RB, Hannart, A, Sitch, S, Haverd, V, Lombardozzi, D, Arora, VK, Pongratz, J, Nabel, JEMS, Goll, DS, Kato, E, Tian, HQ, Arneth, A, Friedlingstein, P, Jain, AK, Zaehle, S, Brovkin, V, 2021. Slowdown of the greening trend in natural vegetation with further rise in atmospheric CO2. Biogeosciences, 18(17): 4985-5010. http://doi.org/10.5194/bg-18-4985-2021
Wulder, MA, White, JC, Loveland, TR, Woodcock, CE, Belward, AS, Cohen, WB, Fosnight, EA, Shaw, J, Masek, JG, Roy, DP, 2016. The global Landsat archive: Status, consolidation, and direction. Remote Sensing of Environment, 185: 271-283. http://doi.org/10.1016/j.rse.2015.11.032
Yang, YT, McVicar, TR, Donohue, RJ, Zhang, YQ, Roderick, ML, Chiew, FHS, Zhang, L, Zhang, JL, 2017. Lags in hydrologic recovery following an extreme drought: Assessing the roles of climate and catchment characteristics. Water Resources Research, 53(6): 4821-4837. http://doi.org/10.1002/2017wr020683
Zhang, Y, Viney, N, Frost, AJ, Oke, AMC, Brooks, M, Chen, Y, 2013. Collation of Australian modeller's streamflow dataset for 780 unregulated Australian catchments. CSIRO, CSIRO, Australia, pp. 115. http://doi.org/10.4225/08/58b5baad4fcc2, last access: November 2024.
Zhao, M, Geruo, A, Liu, YL, Konings, AG, 2022. Evapotranspiration frequently increases during droughts. Nature Climate Change, 12(11): 1024-1030. http://doi.org/10.1038/s41558-022-01505-3
Zheng, HX, Chiew, FHS, Post, DA, Robertson, DE, Charles, SP, Grose, MR, Potter, NJ, 2024. Projections of future streamflow for Australia informed by CMIP6 and previous generations of global climate models. Journal of Hydrology, 636. http://doi.org/10.1016/j.jhydrol.2024.131286